2023

DEVELOPMENT OF ADVANCED GERMANIUM DETECTORS FOR RARE EVENT PHYSICS

Sanjay Bhattarai

DEVELOPMENT OF ADVANCED GERMANIUM DETECTORS FOR RARE EVENT PHYSICS

By

Sanjay Bhattarai

B.S., (Tribhuvan University), (2011)
M.S., (Tribhuvan University), (2016)

A Dissertation Submitted in Partial Fulfillment of the
Requirements for the Degree of Doctor of
Philosophy

Department of Physics

Physics Program
In the Graduate School
The University of South Dakota
May 2023

The members of the Committee appointed to examine
the Dissertation of Sanjay Bhattarai find it
satisfactory and recommend that it be accepted.

DocuSigned by:
Dongming Mei
31A24A6D89824AD...

Chairperson, Dr. Dongming Mei

DocuSigned by:
D7C37880D26F476...

Dr. Jing Liu

DocuSigned by:
Dr. Henry Wong
882EAAA1D6D145F...

Dr. Henry Wong

DocuSigned by:
Chaoyang Jiang
2171313D0259446...

Dr. Chaoyang Jiang

DocuSigned by:
Dr. Juergen Reichenbacher
3F1D000494E7472...

Dr.Juergen Reichenbacher

ABSTRACT

High Purity Germanium (HPGe) detectors are widely used in rare-event physics searches for dark matter, neutrinoless double-beta decay, and solar neutrinos. This dissertation focuses on improving crystal quality by controlling the impurity concentration, dislocation density, and growth environment as well as developing advanced Ge detectors for various physics applications. The dissertation presents experimental investigations of electrical conduction mechanisms in p-type amorphous germanium (a-Ge), which is used as an electrical contact material in HPGe detectors. By measuring the surface leakage current from three high-purity planar Ge detectors, we determine the localization length and hopping parameters in a-Ge. The dissertation also explores the possibility of using advanced Ge detectors to detect solar neutrinos. We investigate the potential of achieving internal charge amplification at cryogenic temperature, which could significantly reduce the energy resolution and energy threshold of Ge detectors. Finally, this dissertation discusses the charge trapping phenomenon of an n-type HPGe detector operated at 5.2 K. We investigate the trapping cross-section and binding energy of cluster dipole states in an HPGe detector, finding that the binding energy of cluster dipole states at 5.2 K is approximately $5-8$ meV. This low energy level makes the detector ideal for detecting low-mass dark matter and solar neutrinos.

Dissertation Advisor Dongming Mei

Dr. Dongming Mei

Acknowledgements

Thank you very much to everyone who has supported and assisted me in finishing my doctoral dissertation. Without your assistance and backing, it could not have been completed. I would want to use this opportunity to convey my deepest gratitude to my supervisor, Dr. Dongming Mei, for leading me through my research in germanium crystal growth and detector fabrication. Your knowledge, patience, and assistance were crucial to the completion of this thesis.

I would also like to thank Dr. Hao Mei for his constant support and encouragement throughout my research. He guided me in learning various aspects of experimental physics researches particularly on high purity germanium crystal growth. Your insights and feedback have been invaluable in shaping my work. In addition, I would like to thank my dissertation committee members Dr.Henry Wong, Dr. Chaoyang Jiang, and Dr. Juergen Reichenbacher for their valuable comments and suggestions.

I would also like to thanks Dr. Jing Liu, Dr. Dr.Guojian Wang and Dr. Wenzhao Wei for their valuable advice, support and encouraging words.

I extend my sincere appreciation to my seniors and juniors for their assistance and advice during my time at the University of the South Dakota. Your support and guidance have been integral to my growth and development as a researcher.

I will always be appreciative of my parents (Mr.Laxmi Prasad Bhattarai and Mrs. Devi Maya Bhattarai) for continuous encouragement, support and blessings throughout my academic career. Without your support and affection, a boy from small town in Nepal would never get this far. I would also like to remember my sisters, Sangam and Sangita for their support and love.

To my wife Shrijana Basnet, I would want to express my sincere gratitude for her

unflagging support, comprehension, and tolerance throughout this journey. I've been inspired by your love and support, and I appreciate every second we've spent together.

I would also like to acknowledge all my relatives, friends and neighbours of my village Khudunabari, Jhapa, Nepal for their constant encouragement and support in my journey.

I want to dedicate this thesis with love to my two beautiful daughters Shivanshi and Shanvi who have inspired me to be a better person and understand life better as a proud father.

Contents

List of Tables

List of Figures

1 Introduction

The quest to understand the nature of dark matter is a central question in physics beyond the Standard Model of particle physics, and it remains one of the most elusive mysteries of our universe. Consequently, a key focus of underground physics is to unravel the properties of dark matter. Many research groups are engaged in this effort using various detection materials and techniques [1, 2, 3, 4, 5, 6, 7, 8, 9]. Since dark matter interacts with ordinary matter through a weakly elastic scattering process, which only leaves a minimal energy deposition from nuclear or electronic recoils [10], detectors with a very low-energy threshold are necessary. Among the current detector technologies, Germanium (Ge) detectors are the best-suited for the search for dark matter [6, 11, 12, 13], as they offer the lowest energy threshold.

HPGe crystals are widely used as detectors for rare-event physics, including the observation of neutrinoless double-beta ($0\nu\beta\beta$) decay, thanks to their excellent energy resolution and ability to minimize background from two neutrino double-beta ($2\nu\beta\beta$) decay [14]. Several research groups, such as MAJORANA[4], GERDA[1], SuperCDMS [3], CoGeNT [13], CDEX [9], and EDELWEISS [6], are utilizing HPGe detectors to detect dark matter and $0\nu\beta\beta$ decay. The LEGEND collaboration [7] is embarking on a new project to use tonne-scale ^{76}Ge detectors in an ultra-low background environment to detect $0\nu\beta\beta$ decay.

The study of solar neutrinos provides valuable insights into the fundamental properties of neutrinos and the sun. Solar neutrinos are emitted in several steps of the pp cycle, such as pp, pep, ^{7}Be, ^{8}B, and the CNO cycle, including ^{13}N, ^{15}O, and ^{17}F neutrinos [15, 16]. These neutrinos have an energy range varying from a few keV to MeV. However, detecting these neutrinos by placing a detector on the earth's surface has always been a challenge in the field of physics. It is difficult to achieve the suitable energy threshold required for detecting each of these neutrinos. A novel technology for detecting low-energy solar neutrinos is the Ge detector that utilizes internal charge amplification for the charge carriers created by the ionization of impurities. This technology has demonstrated experimental sensitivity to detect low-energy solar neutrinos with high precision.

1.1 Dark matter

Dark matter is a mysterious form of matter that is believed to make up a significant portion of the universe's total mass. It is called "dark" because it does not emit, reflect, or absorb electromagnetic radiation, making it invisible to telescopes that rely on such radiation. According to the standard model of cosmology, dark matter accounts for approximately 27% of the universe's total mass, with the remaining 68% attributed to dark energy and 5% to ordinary matter [17].

One of the most compelling pieces of evidence for the existence of dark matter comes from observations of the gravitational effects it has on visible matter. Swiss astronomer Fritz Zwicky was one of the first to propose the existence of dark matter in the 1930s while studying the Coma Cluster of galaxies. He noticed that the gravitational forces holding the cluster together were far greater than what could be accounted for by the visible matter alone [18, 19]. In the 1970s, American astronomers Vera Rubin, Kent Ford, and Norbert Thonnard made similar observations while studying the rotation speeds of stars in spiral galaxies [20, 21]. They found that the visible matter in galaxies was insufficient to explain the observed rotational velocities of stars. Specifically, they expected the velocities of stars to decrease as their distance from the center of the galaxy increased, but instead found that the velocities remained constant at any radius of the galaxy, as shown in Fig-

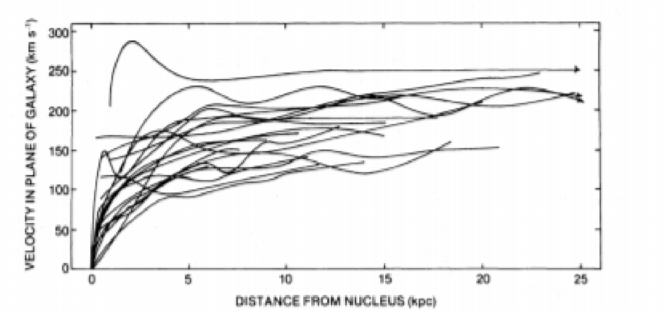

Figure 1: Measured rotation curves from a sample of 21 spiral galaxies. All galaxies show flat rotation curves. [20]

ure 1. One possible explanation for this phenomenon is the presence of uniformly distributed but invisible matter throughout the galaxy - dark matter.

There are multiple lines of evidence that support the existence of dark matter, including the bullet cluster, measurements of gravitational lensing, and observations of temperature anisotropies in the cosmic microwave background [22]. While the nature of dark matter remains a mystery, there are several candidates proposed as dark matter particles, with weakly interacting massive particles (WIMPs) being one of the most plausible.

Numerous experiments have been developed or planned to detect WIMPs, utilizing various techniques and materials [23, 24]. Direct detection involves the search for the elastic scattering of WIMP-nucleon off a target nucleus within a suitable detector. Indirect detection techniques seek out dark matter decay or annihilation products. In some cases, dark matter particles are produced from the collision of electrons or protons in the lab, which is another approach used in the field of dark matter search.

Our research focuses on the direct detection technique that employs HPGe detectors. When a dark matter particle interacts with the nuclei of Ge atoms, it generates an electron-hole pair, which can be detected by the detector through the drift charge or phonons. Detecting this energy indicates the possibility of detecting WIMPs, although this is an extremely challenging task. The interaction between WIMPs and Ge nuclei has a very small cross-section since WIMPs interact through the weak force, and there are many background events reaching the Ge detector. To increase the detection efficiency, it is essential to maintain a low background environment by reducing background contributions from cosmogenic rays, environmental gamma rays, and surface backgrounds. Placing the detector in a deep underground laboratory can significantly decrease these backgrounds. Several deep underground laboratories are used to detect dark matter, including the Soudan Mine in Minnesota (USA), the Sanford Underground Research Facility (USA), the SNOLAB underground laboratory at Sudbury, Ontario (Canada), and the Gransaso laboratory (Italy). Most experiments use Ge or silicon (Si) detectors at cryogenic temperatures (in the order of milliKelvins) to detect phonons generated when a WIMP interacts with the target crystal. Some experiments that use solid-state low-mass WIMP detectors are:

1) Super Cryogenic Dark Matter Search (SuperCDMS)

The SuperCDMS, Soudan experiment was located deep underground in the Soudan Mine in Minnesota and collected data from 2011 through 2015. It operated arrays of monocrystalline Ge and Si detectors at cryogenic temperatures (≈ 50 mK). The detectors were instrumented to measure ionization and phonon signals. It set stronger limits for low mass WIMPs of masses between 4 and 6 GeV/c^2 [25]. SuperCDMS at SNOLAB, Canada will deploy number of next generation detectors to study the backgrounds more efficiently and reduce the parameter space for differential cross-section and mass of dark matter. The target of this experiment is to reach sub-GeV dark matter [26, 27].

2) Experiment for Direct Detection of WIMP Dark Matter (EDELWEISS)

The EDELWEISS is located at the Modane Underground Laboratory in France. It uses 24 cylindrical HPGe crystals at $\approx$ 20 mK, with the surfaces fully instrumented with inter-digitated charge measurement electrodes [28]. This arrangement allows for rejection of background events near the crystal surfaces. These detectors are surrounded by layers of passive shielding and an active muon veto. They have set competitive limits for WIMP masses of 4-30 GeV/c^2 [29, 30].

3) Cryogenic Rare Event Search with Superconducting Thermometers (CRESST)

The CRESST is located at the Gran Sasso underground laboratory in Italy. It operated 13 detector modules in CRESST-III Phase 1 (2016-2018). It used $CaWO_4$ crystals as the target mass and phonon detector. Phonons were measured using W-TES (transition edge sensors) read out with SQUID (superconducting quantum interference device) based amplifiers. The CRESST devices are sensitive to lower WIMP masses than other technologies with WIMP masses down to 500 MeV/c^2. A preliminary analysis of the spectrum from a new, more sensitive set of devices produced a world-leading limit below 1.7 GeV/c^2 [31].

Although none of these experiments has yet been able to find the dark matter particle, they have set high upper bounds on the mass and nucleus interaction cross-section of these particles. Despite intense efforts to find WIMPs, none of the trials have succeeded as of yet. Many have therefore begun exploring for alternatives to it. Several more particles, such as Sterile Neutrinos, Axions, MACHO, etc., are contenders for dark matter.

1.2 Dark phonons

The Standard Model (SM) is one of the most successful physics models, defining the interactions between all known elementary particles that constitute the fundamental building blocks of the universe. However, it fails to provide a definition for dark matter particles. In some dark matter theories, dark photons could be a potential candidate for dark matter. The interactions between dark matter particles might be mediated by an unknown particle that kinetically couples with the SM photon through a weak coupling factor. Dark photons could be artificially produced in a laboratory or found in astrophysical sources, with the sun being one of the primary sources. Ge detectors have been used in recent experiments such as the China Dark Matter Experiment (CDEX) [32] to detect dark photons. Since dark photons may or may not have mass, highly sensitive detectors with an energy threshold as low as 0.01 eV are necessary to explore a wide range of assumed masses of dark photons. Low-threshold germanium detectors that utilize internal charge amplification of phonons generated by germanium are a promising strategy to enhance the sensitivity of Ge detectors for detecting dark photons.

1.3 Neutrinoless double beta decay

Neutrinoless double beta decay is a nuclear transition that has been hypothesized by Ettore Majorana in 1937 [33]. It involves the simultaneous decay of two neutrons into two protons without the emission of any neutrinos. This decay can only occur if neutrinos are Majorana particles, which means that they could be their own antiparticles.

$$(A, Z) \longrightarrow (A, Z + 2) + 2e- \tag{1}$$

This decay can be mediated by many processes, all involving physics beyond the standard model, among them the simplest model is the light neutrino exchange model. The Feynman diagrams for this model is shown in the Fig 2. This neutrinoless double beta decay model proposes that a pair of W-bosons are produced at the

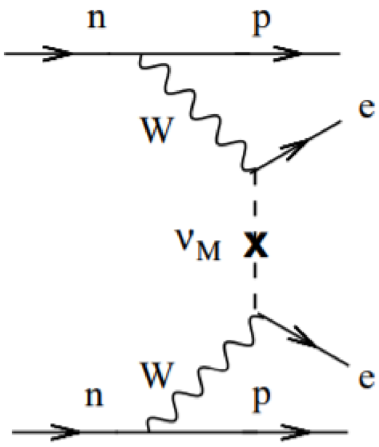

Figure 2: Feynman diagram of neutrinoless double beta decay [34]

first vertex and exchange light neutrinos at the second vertex, resulting in a pair of outgoing electrons. The detection of this decay would have significant implications for both standard model physics and neutrino physics. One of the fundamental symmetries in standard model physics, the conservation of lepton number, would be explicitly broken by two units. Additionally, this decay could explain the matter-antimatter asymmetry in the universe through the phenomenon of leptogenesis and could shed light on the absolute mass scale of neutrinos. However, due to the rarity of this decay and the need for a nearly background-free setting with high exposure, experimental observation is challenging. Many dedicated experiments are actively searching for this decay using different isotopes and techniques, such as those referenced in [4, 1, 35, 36]. For instance, the LEGEND experiment [37] is constructing a ton-scale experiment using Ge detectors with the experience gained from a variety of noble techniques used in the Majorana [38] and GERDA [7, 39] experiments. Similarly, nEXO [40] is building a ton-scale experiment using a liquid xenon time projection chamber based on their experience with the EXO experiment.

1.4 Solar neutrinos

The neutrinos generated at the sun's core by nuclear fusion processes are known as solar neutrinos. Understanding the operation of the sun is made possible by the study of solar neutrinos, which also reveals information about the fundamental characteristics of neutrinos. The sun undergoes a variety of nuclear fusion reactions that result in solar neutrinos with variable fluxes and maximum energy [41]. The solar neutrinos emitted in several steps of the proton-proton (P-P) cycle are pp, pep, ^{7}Be, ^{8}B and hep ($[^{3}He(p, e^{+}\nu_{e})^{4}He]$) neutrinos. The solar neutrinos produced through the Carbon-Nitrogen-Oxygen (CNO) cycle are mainly ^{13}N, ^{15}O and ^{17}F neutrinos [15, 16]. The energy range of these neutrinos varies from a few keV to a few MeV. Detecting these neutrinos by placing a detector in a underground laboratory has always been a challenge. A suitable energy threshold for detecting each of these neutrinos is difficult to achieve. Numerous collaborations have used different detector materials and techniques to study solar neutrinos. Homestake [42], Super-Kamaiokande [43], SNO [44], BOREXINO [45, 46], GALLEX/GNO [47], SAGE [48], LENS [49], are some of the experiments that studied solar neutrinos with the detection energy threshold greater than 233 keV. By detecting the flux of neutrinos from the ^{8}B reaction in the sun, SNO was able to completely demonstrate neutrino flavor transition using charge current (cc) and neutral (nc) current reactions [44]. The comparison of reaction rate between cc and nc reactions helps in the measurement of total electron neutrino (ν_e) flux and the total flux independent of the flavor (ν_e, ν_τ, ν_μ). A strong suppression of electron neutrinos was observed relative to that expected in the standard solar model (SSM) [50]. This indicated that the electron neutrinos from the sun are changing to other flavor of neutrinos by neutrino flavor transition. The most accurate measurement of neutrino sur-

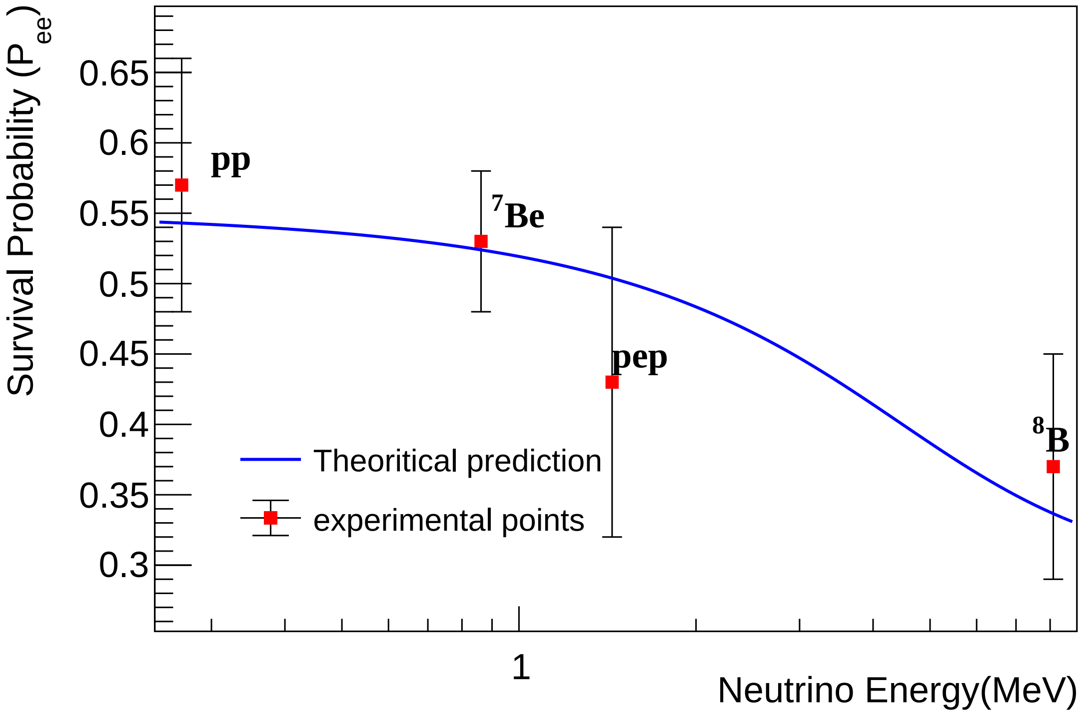

Figure 3: Survival probability of solar neutrinos from pp chain [51].

vival probability to date is observed by Borexino [51]. They used elastic neutrino-electron scattering to experimentally calculate the values of survival probability [51] for four electron neutrinos from the *pp* chain which is shown in Figure 26. There is a significant amount of difference between the theoretical [52, 53, 54, 55] and the experimental values as depicted in Figure 26.

Over 99 percent of the total solar neutrinos produced from *pp* cycles are believed to be *pp* neutrinos [41]. With an end-point energy of 423 keV and a continuous spectrum, they are challenging to detect using liquid scintillation detectors. This is due to the fact that background noise frequently contaminates the energy caused by elastic neutrino-electron scattering, and the energy deposited through elastic neutrino-nucleus scattering is below the detection threshold. Thus, as demonstrated by Borexino, the measured event rate from *pp* neutrinos might be slightly imprecise[45].

1.5 Germanium Detectors

It is necessary to utilize extremely sensitive detectors that can pick up tiny signals in order to look for rare events like dark matter interactions or neutrinoless double beta decay. Due to its great energy resolution and minimal background noise, germanium detectors have demonstrated to be quite efficient in this area.The purity of the germanium material utilized, however, has a significant impact on the sensitivity of these detectors. Impurities of any size can have a big impact on a detector's performance, lowering sensitivity and raising background noise. The impurity in the crystal is expected to be less than the level of $3 \times 10^{10}/\text{cm}^3$ and the detector grade crystal should should have the dislocation density that falls in between $3 \times 10^2/\text{cm}^2$ to $10^4/\text{cm}^2$. Hence, the high purity germanium detectors are required to attain the required sensitivity, and these detectors can only be produced through a complex crystal growth and purification procedure.

This PhD thesis aims to explore the requirement and importance of high purity germanium detectors for rare event searches, as well as the crystal growth and purification techniques required to produce them. Additionally, the fabrication process of a high purity germanium detector will be examined to ensure that it meets the necessary specifications for use in rare event searches. This will include an examination of the zone refining technique used to purify germanium crystals and the crystal growth process used to produce high-quality germanium detectors.

Germanium ingots are gradually purified during the zone refining process by repeatedly melting and solidifying them. Because the impurities in the germanium material have different melting and freezing temperatures from germanium, this procedure enables their selective removal. In the process of zone refining, a short molten zone is generated along the ingot and moved along its length, pushing impurities to one end of the ingot.

The purification process is optimized by regulating the temperature gradient and the number of passes through the zone refining device. Greater temperature gradients can result in more effective purification, but they can also cause the evaporation of germanium, which can lead to the loss of germanium. Additionally, the number of passes through the zone refining apparatus affects the level of purification achieved, with more passes resulting in higher purity.

The Czochralski (CZ) technique can then be used to grow high purity germanium crystals from the purified germanium ingots. Purified germanium is melted in a crucible as part of the CZ process, and the melt is then used to form a single crystal. A seed crystal is needed to start the crystal development process, and the crucible is often made of quartz or graphite. To create a high-quality crystal, the temperature (power) and pulling rate of the seed crystal are controlled during the CZ process. The temperature must be high enough to melt the germanium material without degrading the crystal or causing significant evaporation. The crystal's growth rate and its structural and electrical characteristics can both be impacted by the pulling rate.

The germanium detector works on the idea of gathering the charge signal generated by the excitation or ionization of electron-hole pairs. The total number of electron-hole pairs and the total amount of charge are related. Furthermore, the maximum of the valence band and the lowest of the conduction band in germanium don't share the same crystal momentum (k-vector). To transfer momentum to the crystal lattice and transit through an intermediate state in an indirect bandgap, the electrons must emit phonons.

1.6 Ge internal charge amplification (GEICA)

Most of the current searches of the rare events using Ge detectors are operated at 77 K or lower. They mostly look for the amplified luke phonons signals generated by the rare events. However, for searches of low mass dark matter and solar neutrinos, detectors with extremely low energy threshold are required. Some of the experiments like CDMS [56], SuperCDMS [25] and EDELWEISS [57] have demonstrated that the energy threshold of ∼50 eV to ∼100 eV can be achieved in Ge detectors through detecting phonons. In 2018, SuperCDMS reported a 3 eV phonon energy resolution with a 0.93-gram Si detector when biased at 100 V [3]. Nevertheless, nuclear recoils induced by these low mass rare event particles require detectors of threshold lower than 1 eV to have meaningful statistics. Therefore, because the current state-of-the-art Ge detectors cannot detect these particles through elastic neutrino-nucleus scattering, a new type of detector is required. A Ge internal charge amplification (GeICA) detector, that amplifies the charge carriers created by the ionization of impurities, is a novel technology with experimental sensitivity for detecting the low-energy solar neutrinos, geo-neutrinos, WIMPS, dark phonons and axions [58, 59].

For a solid state detector, such as a Ge detector, both coherent elastic neutrino-nucleus scattering (CEvNS) and elastic neutrino-electron scattering can be detected. However, since the detectors are much smaller in size compared to liquid scintillation detectors, the energy deposited through elastic neutrino-electron scattering is often immersed in backgrounds. Nevertheless, the event rate grows exponentially as a function of nuclear recoil energy through elastic scattering off the nucleus. It is expected that the event rate will significantly surpass the background in the low energy range of nuclear recoils. This is because the expected nuclear recoil events (signal) grows exponentially while electric recoil events (background) remains flat in the region of interest. Thus, elastic neutrino-nucleus scattering represents a viable tool to measure *pp* neutrinos in a Ge detector. The maximum nuclear recoil energy produced by *pp* neutrinos via elastic neutrino-nucleus scattering in a Ge detector is ∼5.2 eV. Hence, to detect the *pp* solar neutrinos, an unprecedented low-energy threshold detector is needed. With an unprecedented low-energy threshold (∼0.01 eV), GeICA detectors can measure the *pp* neutrinos flux through CEvNS with good statistics and hence the current uncertainty in neutrino survival probability (Figure 26) can be decreased. In this work, I describe the GeICA detector technology for achieving a sensitivity in detecting low-energy *pp* neutrinos. GeICA will amplify the charge carriers induced by *pp* neutrinos interacting with Ge atoms through the emission of phonons[58]. It is those phonons that will create charge carriers through the ionization of impurities to achieve an unprecedented low energy threshold of ∼ 0.01 eV.

The interaction between dark matter (DM) and ordinary matter is limited to weak elastic scattering processes, resulting in only a small energy deposition from nuclear or electron recoil [60, 61, 62]. This highlights the need for a detector with a very low energy threshold to detect DM [58]. The LZ experiment has pushed the sensitivity for weakly interacting massive particles (WIMPs) with a mass greater than 10 GeV/c^2 to the point where the neutrino-induced background limits its sensitivity [63]. However, the recent emergence of low-mass DM in the MeV range has generated excitement as a DM candidate, although current experiments cannot detect it due to its small mass. The detection of MeV-scale DM requires new detectors with thresholds as low as sub-eV, since both electronic and nuclear recoils from

MeV-scale DM range from sub-eV to 100 eV [64]. Conventional detector techniques cannot detect this low-mass DM. Germanium (Ge) detectors have the lowest energy threshold among any current detector technology, making them ideal for low-mass DM searches [25, 11, 61, 6]. The band gap of Ge at 77 K is 0.7 eV and the average energy required to generate an electron-hole pair in Ge is about 3 eV [65]. Thus, a Ge detector can provide a very low energy threshold. Furthermore, proper doping of the Ge detector with impurities can expand the parameter space for low-mass DM searches even further. Shallow-level impurities in Ge detectors have binding energies of about 0.01 eV, and can form dipole states and cluster dipole states when operated at temperatures below 10 K [58, 66, 67]. These dipole states and cluster dipole states have even lower binding energies than the impurities themselves, providing a potential avenue for detecting low-mass DM. Although the binding energies of impurities in Ge is well understood [68, 69], little is known about the binding energy of the dipole states and cluster dipole states near helium temperature. I have studied the binding energy and trapping cross-section of different charged states in a p-type HPGe detector at 5.2 K [70].

Apart from this, I have also, for the first time, experimentally studied electrical conduction mechanisms in the disordered material system (p-type amorphous germanium (a-Ge)) used for high-purity Ge detector contacts. The localization length and the hopping parameters in a-Ge are determined using the surface leakage current measured from three high-purity planar Ge detectors. The temperature dependent hopping distance and hopping energy are obtained for a-Ge fabricated as the electrical contact materials for high-purity Ge planar detectors. As a result, it was found that the hopping energy in a-Ge increases as temperature increases while the hopping distance in a-Ge decreases as temperature increases. The localization length of a-Ge is on the order of $2.13^{-0.05}_{+0.07}$ A° to $5.07^{-0.83}_{+2.58}$ A°, depending on the density of states near the Fermi energy level within band gap. Using these parameters, it was predict that the surface leakage current from a Ge detector with a-Ge contacts can be much smaller than one yocto amp (yA) at helium temperature, suitable for rare-event physics searches.

1.7 Summary

In summary, this dissertation work focus mainly on:

1. Purification of germanium by zone refining process, converting them into high purity crystals by crystal growth method and fabrication of a high purity germanium detectors which is discussed in the Chapter 2.

2. In the Chapter 3, this thesis discusses the investigation of p-type amorphous contacts used for reducing the surface leakage current and hence increase the performance of a HPGe detector. This project also contributes to the study of these contacts at liquid helium temperature which significantly helps the research and development of advanced germanium detectors that utilizes germanium internal charge amplification of phonons created by ionization of impurities [71].

3. Chapter 4 discusses the scientific potential of detecting low energy solar neutrinos and low energy dark photons utilizing unprecedented low threshold GEICA detectors [72].

4. Chapter 5 investigates the behaviour of HPGe detectors at cryogenic temperatures and find the binding energy and trapping cross section of different charge states and understand the possibility of achieving internal charge amplification in such low temperatures [70, 67] which will be extremely useful in detecting low energy rare events particles.

2 Research and Development activities at USD

Rare event searches detection favors large HPGe detectors. But the impurity limits the size of the detector as the detector needs to be fully depleted for the operation. The depletion depth of the detector is given by

$$d = \sqrt{2\epsilon V_0 / eN} \tag{2}$$

where t is the thickness detector, ϵ is the relative permittivity of Ge and V_0 is the applied reversed bias voltage, e is the charge of the electron and N is the net impurity concentration. A reverse bias of 1000 volts can produce a depletion width 1cm for the net impurity concentration of $10^{10}/\text{cm}^3$. Hence, the impurity in the crystal is expected to be less than the level of $3 \times 10^{10}/\text{cm}^3$.

Another important factor that determines the performance of HPGe detector is the dislocation density in the crystal. Detector grade crystal should should have the dislocation density that falls in between $3 \times 10^2/\text{cm}^2$ to $10^4/\text{cm}^2$. Dislocations act as nucleation centres for vacancies and as trap for the impurity ions. If there are few or no dislocations, they act as gettering centre, thereby isolating the defects which trap the charge carriers. However, if there are excessive dislocation densities they serve as generation/recombination centers or the trap centres for the charge carriers. This result in increase in leakage current in the detector and hence the sensitivity of the detector is reduced.

Commercial suppliers supply the Ge ingots usually of the impurity level of $10^{13}/cm^3$ to $10^{14}/\text{cm}^3$. It is extremely difficult to obtain the desired net impurities in the crystal by crystal growth process alone. Hence, we purify the Ge in two steps

a) Zone refining the ingots and obtain the impurity level of the order of $10^{11}/\text{cm}^3$.

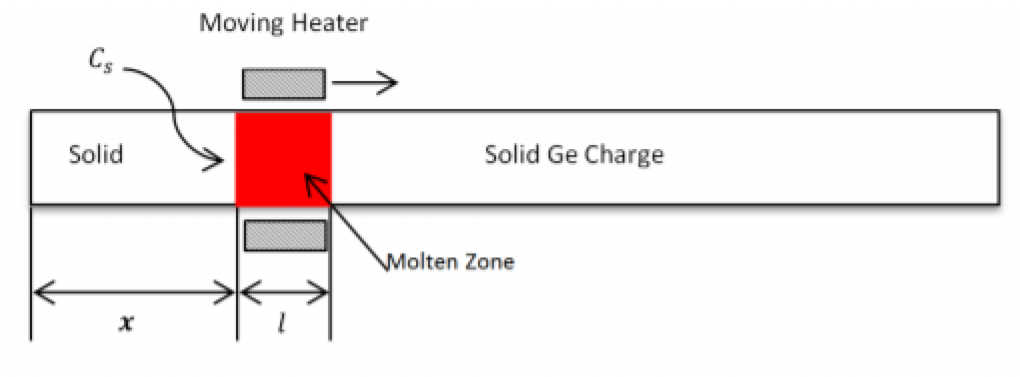

Figure 4: Theoritical model of zone refining.

b) Grow a crystal to obtain the impurity in the order of $10^{10}/\mathrm{cm}^3$.

2.1 Zone Refining

2.1.1 Zone refining principle

Zone refining is one of the most effective and popular method for purification of metals and semiconductors. It was developed by Willian Gardner Pfann in Bells lab in the 1950s [73]. It is based on the principle that the different impurities segregate differently in solid and liquid part of the material.

In this process, raw Ge ingots brought from the commercial companies are placed in a boat made up of non reactive materials (quartz, graphite). Both the Ge ingots and the quartz boats are etched and dried before putting inside the zone refining system that consists of a glass tube. An inducting heating coil moves along the cylinder which creates a molten zone in the Ge. This narrow zone moves slowly as the coil moves. The impurities moves along the molten zone from one end to another thereby purifying the Ge ingots as shown in Figure 4. This process is repeated multiple times to enhance the efficiency of the zone refining.

The main impurities existing in the starting of the Ge were identified by Photo thermal ionization spectroscopy (PTIS) to be boron (B), phosphorous (P) and alumunium (Al). The temperature and the coil speed can be controlled very precisely. This lead to narrow zone width (about 2 cm) moving away from left to right. Impurities will be deposited on left and right side of the tubes depending upon the segregation of the impurities. Impurities having segregation coefficient greater than 1 are deposited on the left hand side of the ingot and those with segregation coefficient less than 1 on the right hand side. After n number of passes during the zone refining, the final impurity level $|N_A - N_d|$ is given by

$$|N_A - N_d| = \sum C_i x[1 - (1 - k_i)exp(-k_i x/L)]^n \tag{3}$$

where n is the total number of passes, i is the impurity, x is the distance from the standing end of the ingot, k_i is the effective segregation coefficient and C_i is the initial concentration of impurities in the ingots.

2.1.2 Zone refining at USD

As we have discussed previously, commercially procured Ge ingots are not suitable for detector fabrication due to the presence of high level of impurities. These ingots are purified by zone refining process in our lab here at USD.

These commercial ingots are cut and cleaned using de-ionized (DI) water and acetone. After that, these ingots are etched using 1HF:3HNO_3 etching solution. Etching removes the surface contamination. Etched materials are then dried using compressed nitrogen gas. The quartz boat and the glass tubes are washed with 30% H_2O_2 and cleaned with DI water.

The segregation coefficient coefficient of aluminium oxide (AlO) is about 1 which makes it difficult to purify as it distributes uniformly in the ingots. To prevent

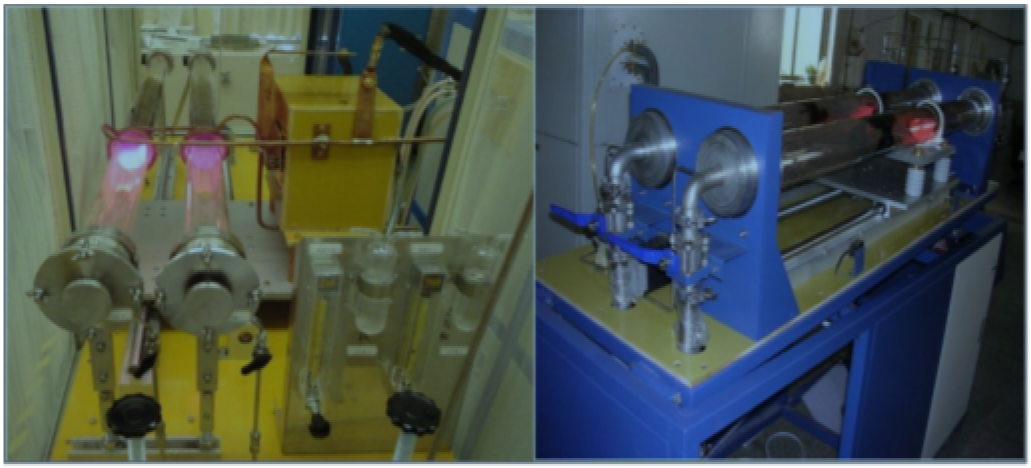

Figure 5: Zone refining set up in USD lab.

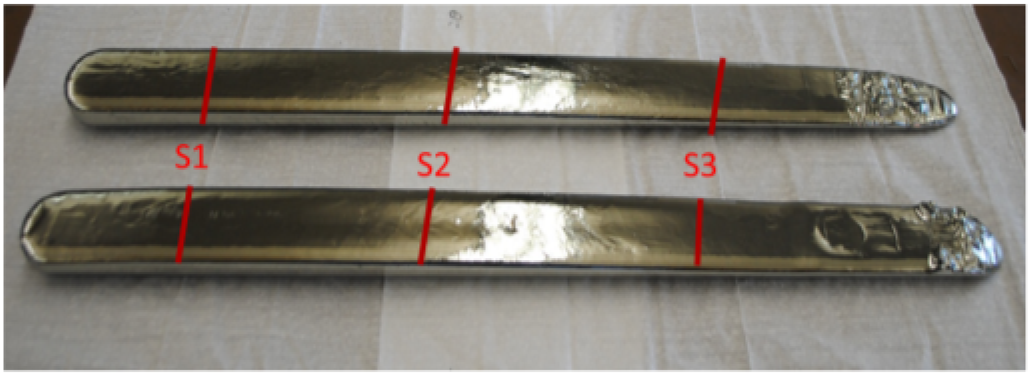

Figure 6: Zone refining ingots ready for characterization.

Al inside the ingots to form AlO by reacting with oxygen in the quartz boat, it is coated with carbon using high purity ethylene gas. Carbon also help to reduce the probability of breaking of the quartz boat when Ge freezes.

Zone refining facility at USD consists of two zone refiners A and B with capability of about 4 Kg Ge ingots as shown in Figure 5. Red portion shown in the same figure is the melted portion of the Ge. A high frequency (200 Hz) coil is used for applying induction heating to the tube to melt the Ge inside it.

Figure 6 shows the Ge ingots taken out from the tube after all the passes are finished. S-5 cm, S-25 cm, and S-40 cm are the three positions of the ingot, we cut with the help of diamond wire saw to get samples for impurity measurements. Since, the ingots from the zone refining are poly crystalline in nature, we lap the samples to find the grain boundaries and cut smaller samples to get crystalline portion of the ingots. These samples are washed with DI water and etched HNO_3:HF, 3:1 solution for about 3 minutes. We used gallium indium eutectic contacts on four corners of the samples and heat them for about 20 minutes at 360°C. This help contacts diffuse into the samples so that we get reliable results for impurity level. We use Hall effect measurement system to measure the net impurity level, mobility and the resistivity of the samples. More about hall effect is described later. Table 1 shows the result of recent zone refining done at USD on 10/13/2022. We can see from the Table 1 that the p-type impurities in the ingots increase as we go from head to tail. This is due to the difference in the segregation coefficients in the impurities. Also, we can only purify the Ge ingots to the order of $10^{11}/\text{cm}^3$ which is below the the requirement for detector fabrication. Also, the ingots we get from zone refining are poly crystals, as we do not use seed crystal in zone refining process. Hence, the zone refining purifies the Ge significantly and these ingots can be further purified and crystallized by the crystal growth process.

position	Net Impurity ($/\text{cm}^3$)	Resistivity (Ω cm)	Mobility (cm^2/Vs)
S-1	1.4×10^{11}	3.8×10^3	1.7×10^4
S-2	3.2×10^{11}	3.6×10^2	2.3×10^4
S-3	5.8×10^{11}	2.9×10^2	3.3×10^4

Table 1: Net impurity concentration, Resistivity and Mobility of the Ge ingots after 7 passes of Zone refinement done in zone refiner B1.

2.2 Crystal growth

The zone refining process do not produce the desired impurity level and single crystal structure required for detection fabrication.Hence, the next step for the process is the HPGe crystal growth using the ingot from the zone refining.

2.2.1 Introduction

A crystal is a solid material whose constituent atoms are arranged in periodic pattern in all three dimensions. Crystal growth is the process of adding new atoms, ions or polymer strings into the characteristic arrangement of the crystalline lattice. A material can be transformed into single crystals from melt, solution or vapor phase. There are various techniques of crystal growth but the development of device quality crystal is always challenging.

One of the widely used method of crystal growth is the czochralski method(CZ) developed by Polish scientist Jan Czochralski [74]. Growth conditions like temperature gradient, gas flow rate, growth orientation can be modified suitably as per the requirement of the material in this process. Seeding and growth process can be seen in real time so that the corrective measures can be taken. These merits make the CZ as one of the most preferred technique of the crystal growth.

In our laboratory, HPGe crystals are grown using CZ method. The set up of the crystal growth system in our lab is shown in Figure 7. As shown in the Figure 7, crystal growth system comprises of furnace, a control panel, a high frequency inducting heating power supply, a weighting scale, a computer, a water cooling system and a hydrogen generator. A HPGe detector has very good energy resolution so that it is an ideal choice for solar neutrino detection experiment. As mentioned earlier, HPGe crystal should have some qualities for fabricating them into good de-

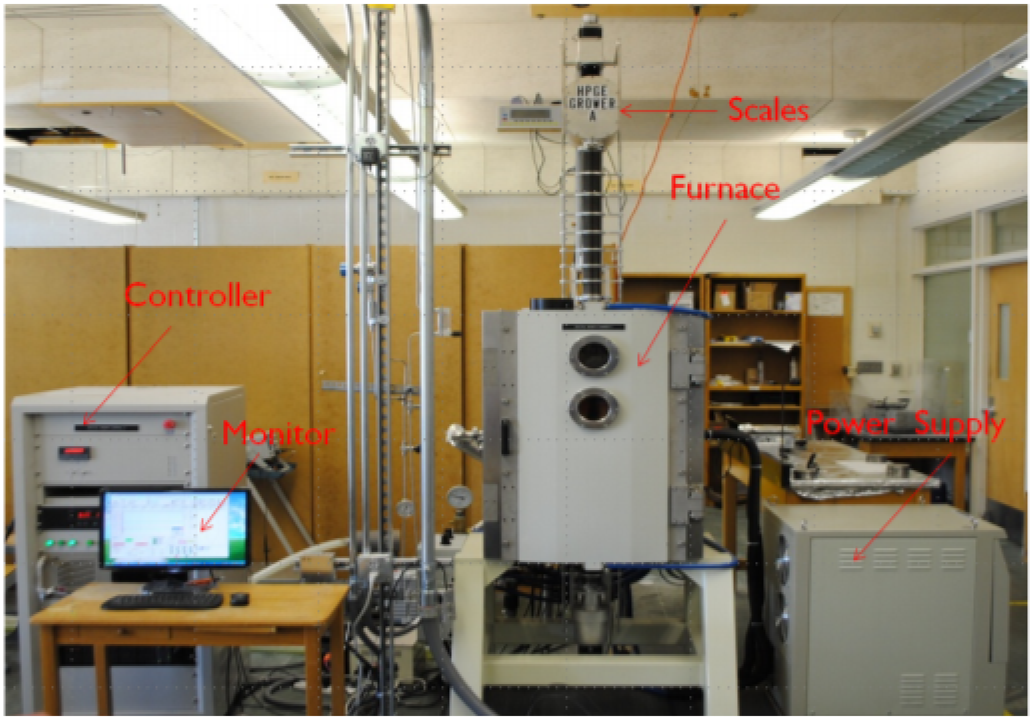

Figure 7: Crystal growth components in USD lab

tectors. They should have net impurity of only $10^9 - 3 \times 10^{10}/\mathrm{cm}^3$ and the dislocation density in the range of $100 - 10000/\mathrm{cm}^2$. Large diameter HPGe crystals result in large detector which increases the probability of rare events detection. However it is extremely difficult to control the thermal field and dislocation density in large diameter crystal. Our goal is to advance crystal growth process so that the large diameter HPGe can be grown with desired criterion for HPGe detectors.

2.2.2 Experimental procedure

The ingots we receive from the zone refining process are cleaned with DI water and the use acetone to clean organic contaminants. We was them again with DI water and etch them with HNO_3:HF (3:1) acid solution to remove the surface contamination. Quartz crucible and radiation glass shield that are used for crystal growth

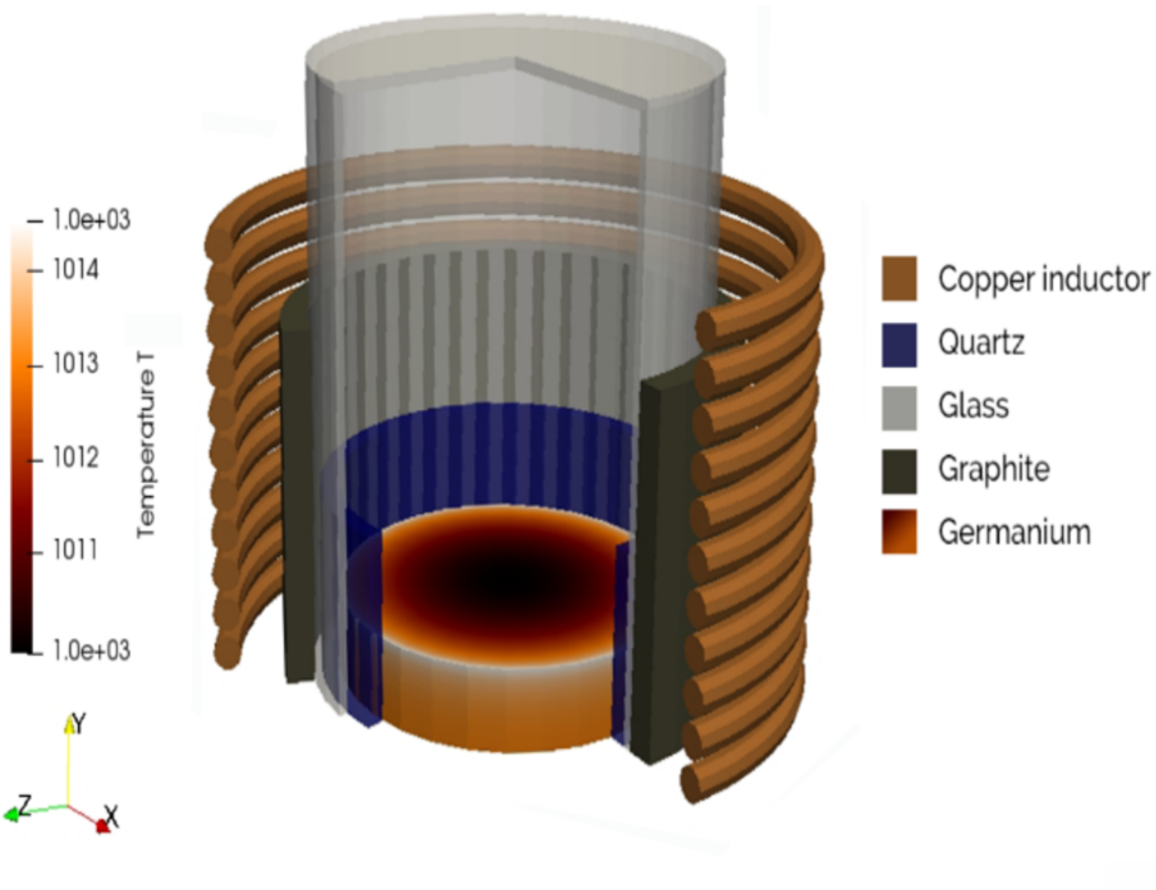

Figure 8: Simulation of melting process of Ge for crystal growth in USD lab.

process are applied with hydrogen per oxide (H_2O_2) and are washed after 15 minutes of application of the solution. Quartz crucible, radiation glass shield and the raw materials are then dried with compress nitrogen gas and loaded in the furnace. Furnace is closed and a mechanical pump is used to reach the vacuum level of 6.9 Pa is about 15 minutes. Then the diffusion pump is used to get the vacuum level of about 2×10^{-4} pa. When the desired vacuum level is obtained, hydrogen gas will flow at the constant flow rate of $8l/min$. Melting of the material is done by high frequency induction heating. Power of the heater is gradually increased and the entire process of melting take about 2 hours. Figure 8 shows a simulation of crystal growth components inside a crystal growth chamber at USD [75].

Once all the material is melted inside the chamber, the supplied input power is decreases that the under-cooling of the melt occurs so that the nucleation is initiated in the crystal growth process. A rotating seed is slowly introduced in the melt and after the equilibrium is achieved, crystal growth process is started by pulling the rod slowly. For controlling the dislocation density in the crystal, diameter of the crystal is gradually increasing in conical shape at the beginning. This process is called dash necking process [76]. Once the neck and the shoulder of the crystal is formed, power is adjusted to control the diameter of the crystal. The diameter is kept constant throughout the body of the crystal.At the lower part of the crystal, diameter of the crystal start to increase slightly and then start to decrease rapidly at the end of process of the crystal growth as shown in Figure 9.

All the melt inside the quartz crucible should be pull out to avoid the breaking of the quartz crucible. The thermal expansion coefficient of Ge and quartz(SiO_2) are different so, they don't cool at the same rate thereby creating a force which can break the crucible. Once the growth process is done, crystal is allowed to cool overnight. The crystal is then taken out of the chamber next day and will be ready for characterization.

2.2.3 Diameter control

The thermal field generated by induction heating is the main factor for controlling the diameter of the crystal. Crystal grower at USD comprises of a glass window through which growing crystal can be observed. Also, there is a camera at the top of the furnace and the image produced by it is projected on the computer screen. Diameter is controlled by observing the growing crystal or its image of it on the computer adjusting the applied power suitably. Diameter (D) of the crystal is given

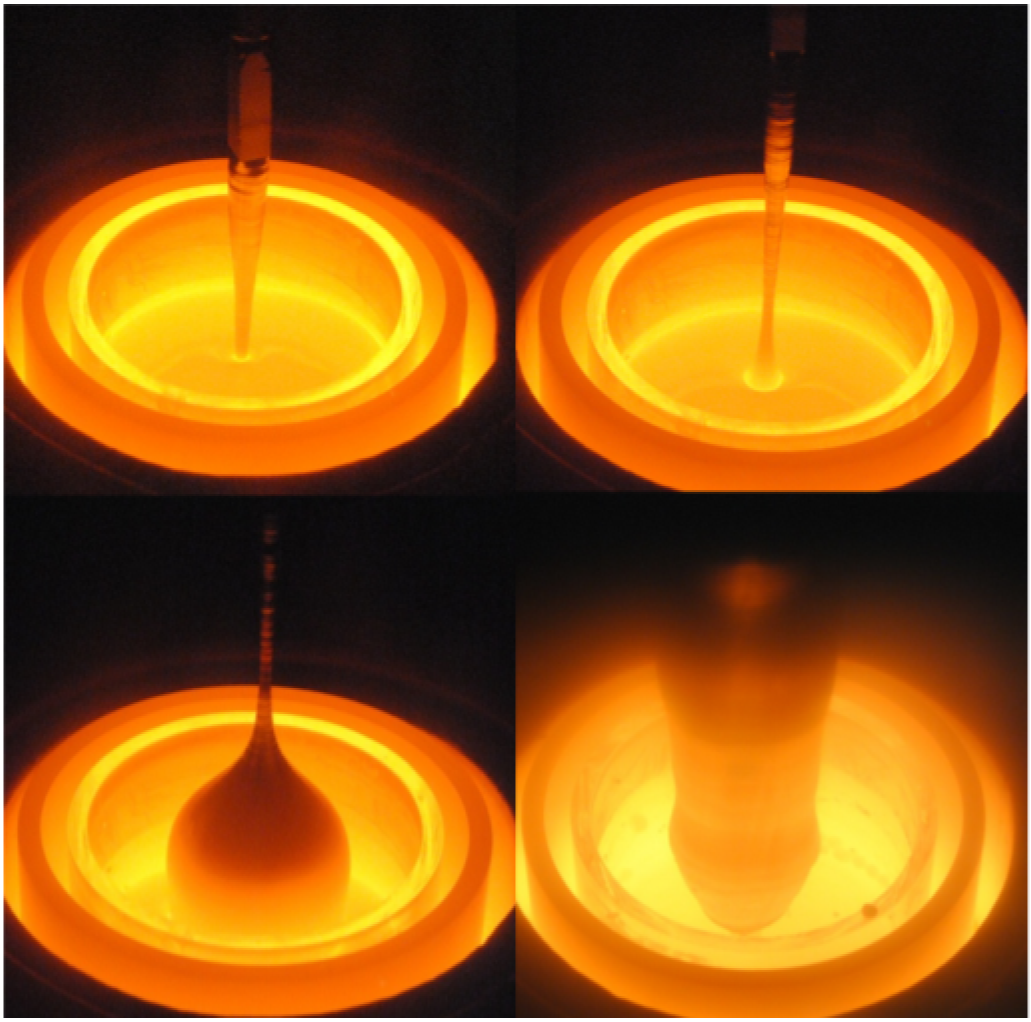

Figure 9: Various step in crystal growth process. Top left: Dipping the seed in the melt. Top Right : Formation of the neck. Bottom left: Growth of the body part. Bottom right: Finishing the crystal growth process.

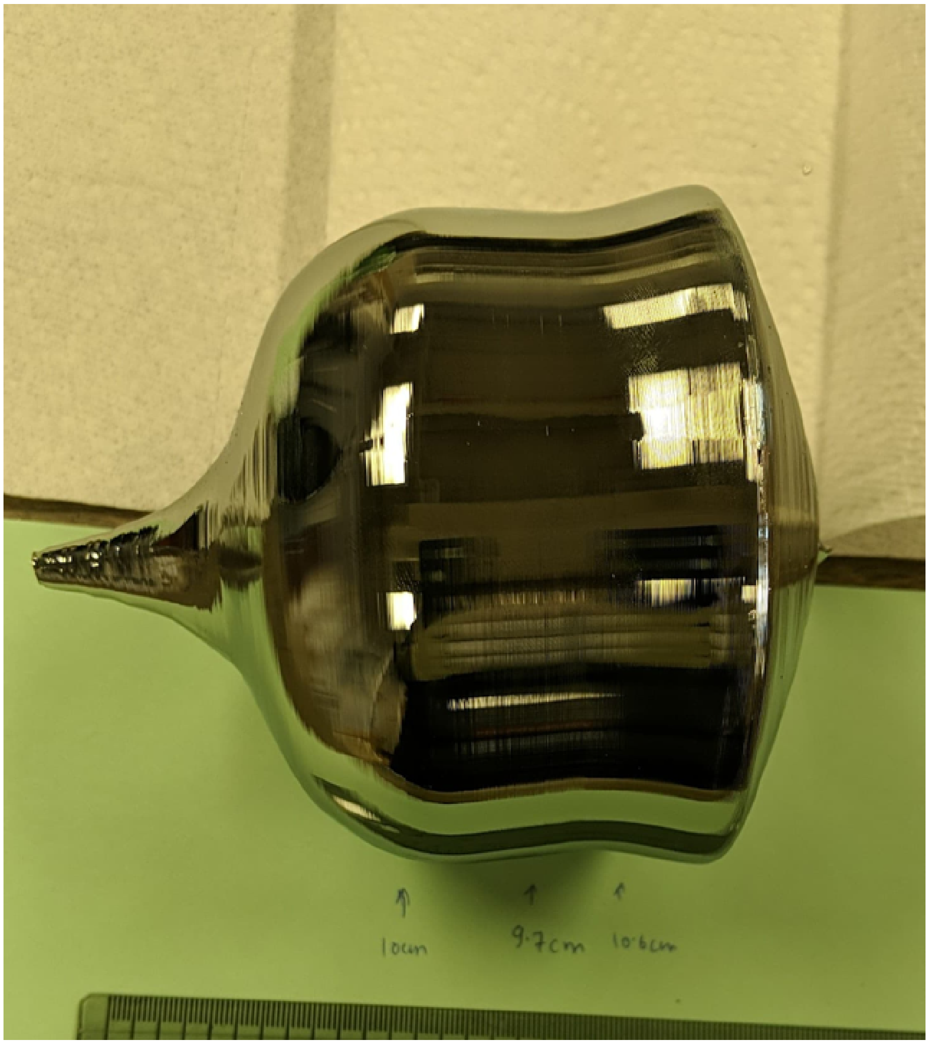

Figure 10: High purity Ge crystal grown in USD lab.

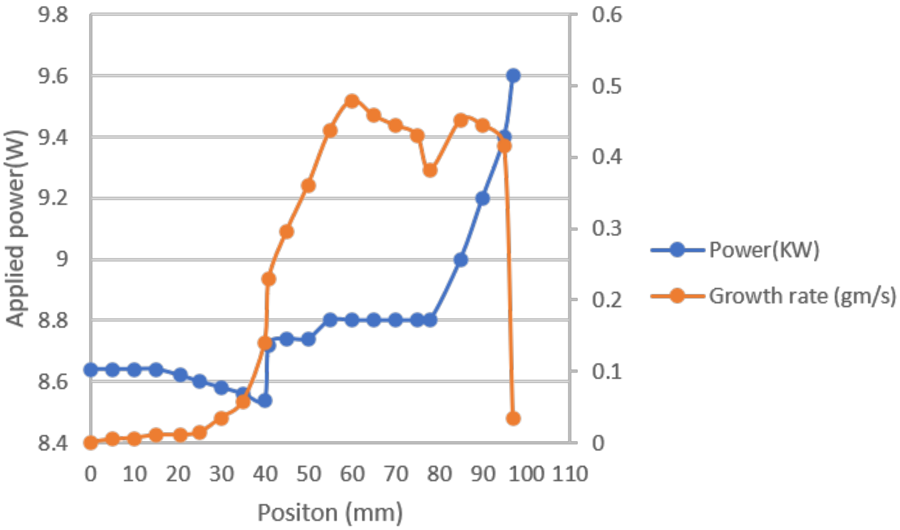

Figure 11: Variation of input power and the growth rate with position for a HPGe crystal grown on 10-08-2020.

by

$$D = \sqrt{\frac{4dw/dt}{p\pi\rho_s + (dw/dt.\rho_s)/R^2\rho_L}} \tag{4}$$

where dw/dt is the rate of change of weight with time, p is the pull rate, ρ_S and ρ_L are the densities of the solid and liquid Ge and R is the crucible radius. Figure 11 power variation with position and the growth rate during the crystal growth process for controlling the diameter along with diameter of the crystal for subsequent power supplied. Figure 11 shows the measured diameter and theoretical prediction. The diameter of the body part is well controlled as shown in figure 12.

2.2.4 Contamination Control

As there are numerous sources of contamination, it is very challenging to control it during the crystal growth process. Diffusion pump which uses a high speed jet of oil vapor to capture gas molecule [77] could flow back the oil vapor into the fur-

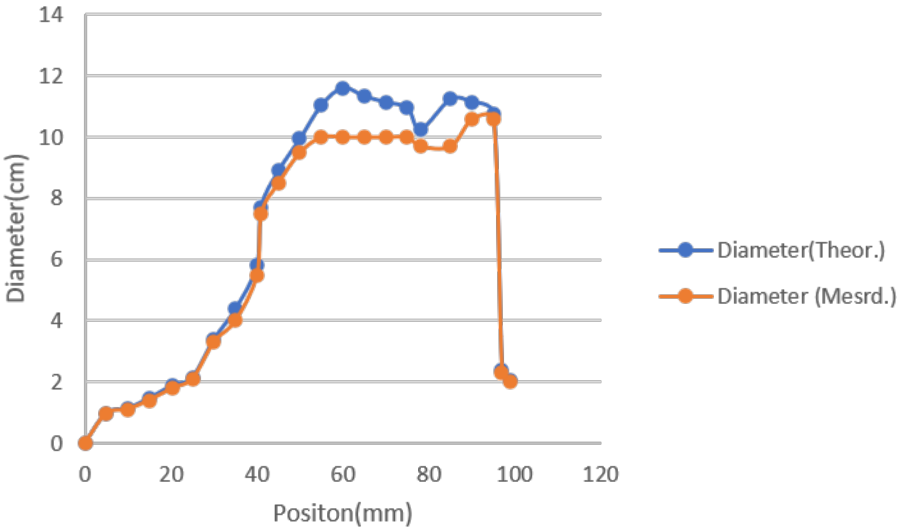

Figure 12: Experimental diameter and theoretical diameter of the crystal grown on 10-08-2020 along its length.

nace. A cold trap is applied at the junction of the pump to reduce the risk and prevent the oil vapors to get back into the furnace.

Another source of contamination is the quartz crucible used for HPGe growth. The impurity level of the quartz crucible should be less than $10^{11}/\text{cm}^3$ to avoid the impurities getting inside Ge melt in high temperature scenario. Also the oxygen contamination in HPGe crystal from the quartz crucible at high temperature is another factor. Hydrogen gas used will react with oxygen and help it evaporate before oxygen from the side surface of crucible reaches the the crystal part in the middle part of the melt. The contamination from the hydrogen gas is also the source of external contamination. Hydrogen environment is created in the crystal growth process by using a glass envelop and cover with the two small holes for letting the hydrogen gas in and out.All the contaminants cannot be removed from the furnace completely. A baking process is applied before the crystal growth to remove the impurity atoms as much as possible. At high temperature, impurities inside the chamber will get activated and flushed by the hydrogen gas during the baking process. Past experiences shows that using the crucible or the furnace without baking cannot achieve the impurity level less than $10^{12}/\text{cm}^3$.

Controlling the impurities in the Ge ingots from the zone refining during the crystal growth is another challenge for HPGe crystal growth. When Ge is pulled out from the melt, effective segregation coefficient coefficient will determine the distribution of impurities. According to the BPS model [78], effective distribution is given by the equation

$$k_{eff} = \frac{C_s}{C_L} = \frac{k}{K + (1-k)exp(-R\delta/D)} \tag{5}$$

where k is the equilibrium distribution coefficient, C_s is the solute concentration in the solid, C_L is the concentration in the melt away from melt the solid liquid interface.

Here, δ is the thickness of the growth interface given by the

$$\delta = 1.6 D_L^{1/3} v^{1/6} w^{-1/2} \tag{6}$$

where D_L is the diffusivity of impurity in the melt, v is the kinematic viscosity and w is the rotation speed used for crystal growth.

Boron has the segregation coefficient greater than 1 so they prefer to concentrate at the head of the crystal. Phosphorous, gallium and aluminium where the equilibrium distribution coefficient is less than 1, will segregate towards the body and the tail part of the crystal. Figure 13 shows the segregation behaviour of main impurities of HPGe crystal [79].

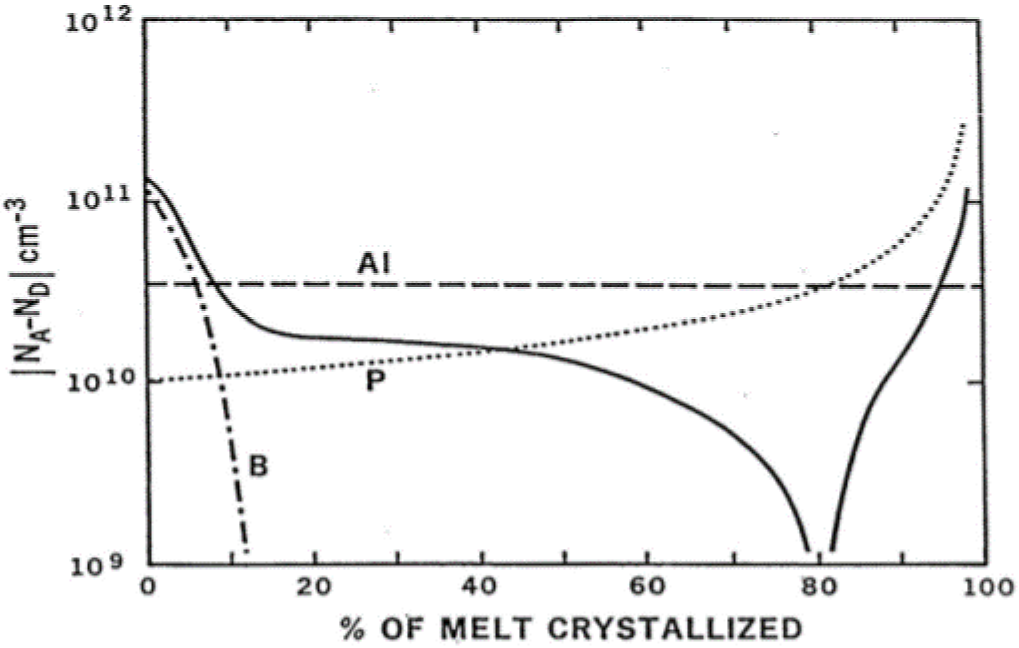

Figure 13: Segregation of various impurities in a Ge crystal.

2.3 Crystal Characterization

After the crystal growth is done, the crystal is taken out of the chamber and is characterized to see if it meets the requirement for detector grade crystal. Dislocation density measurement and the net impurity measurement are the two characteristics we measure usually. Other than that, crystal plane orientation is also measured once in a while to check weather crystal are in (100) plane or not.

2.3.1 Measurement of impurities

Hall effect measurement system is used to measure the net impurity concentration in the crystal. Hall effect is based on the theory that when the magnetic filed is applied perpendicular to the flowing current, it will have a sideways deflection of charge carrier and a resulting voltage across the conductor is developed [80]. Hall

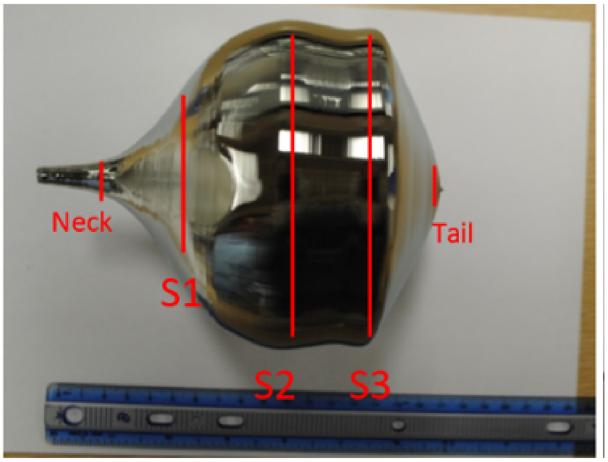

Figure 14: Positions of a HPGe crystal for the characterization.

voltage is given by

$$V_H = -IB/ned \tag{7}$$

where I is the applied current, B is the applied magnetic field, d is the thickness of the sample and n is the concentration of charge carriers.

Hall coefficient is given by

$$R_H = V_H d/IB = -1/ne \tag{8}$$

If we know the hall coefficient then the net charge carrier concentration can be calculated.

For performing the hall effect measurement, the crystal is cut into three slices using diamond wire saw from three position in the crystal S1, S2, and S3 as shown in Figure 14.

Then the wafers are further cut into samples of 1.5 × 1.5 × 0.1 cm^3. They are polished and etched ($HNO_3 : HF; 3 : 1$. Four contacts are made at the four corners of the samples by scratching Indium Gallium eutectic Ohmic contacts. Using the

Figure 15: Hall effect measurement system in USD lab.

position	Net Impurity (/cm^3)	Resistivity (Ω cm)	Mobility (cm^2/Vs)
S1	4.9×10^{10}	3.7×10^3	3.6×10^4
S2	4.2×10^{10}	2.9×10^3	3.4×10^4
S3	-5.06×10^{11}	3.8×10^2	2.1×10^4

Table 2: Net impurity concentration, Resistivity and Mobility of the recently grown (05-14-2022) HPGe crystal in USD lab.

Vander Pauw Hall effect measurement system (Ecopia HMS-300 with 0.5 Tesla permanent magnet) as shown in Figure 15 [81].

Impurities are measured at 77K since our detector are also operated at same temperature by using liquid nitrogen. Apart from the impurities level, hole or electron mobility, resistivity and the Hall coefficient can also be measured by this system. Table 2 shows the net impurity level of the most recent detector grade crystal grown in USD lab.

The table shows that the region between S1 and S2 which is about 2 cm thick,

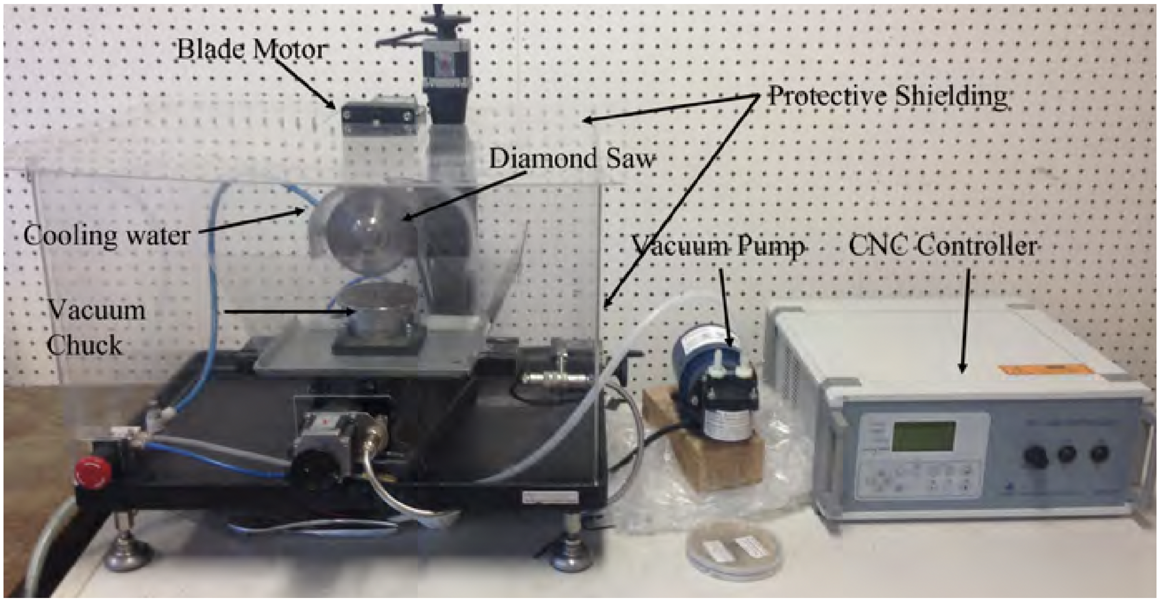

Figure 16: The configuration for cutting and grinding the crystal to give it the desired geometry is shown.

about 10 cm in diameter and mass of 1 Kg is suitable for detector fabrication.

2.4 High purity germanium detector

After the commercially brought Ge ingots are converted into high purity germanium crystals, they are fabricated into HPGe detectors. It is a sensitive process where handling of the crystal in different steps of the fabrication is very important. The recipe for the fabrication is described in brief in this section.

Ge is prone to breaking. The crystal boule is cut using a diamond saw to get the desired geometry. To prevent cracks or chips, grinding the Ge crystal is preferable to cutting. Usually, less than 2 mm per minute is the grinding speed. For the manufacturing of the detector, it is vital to handle the crystal sample well. Even a little scratch that occurs during the manufacture and loading of the detector could cause the a-Ge contacts to fail the electrical test. The Ge crystal needs to be properly

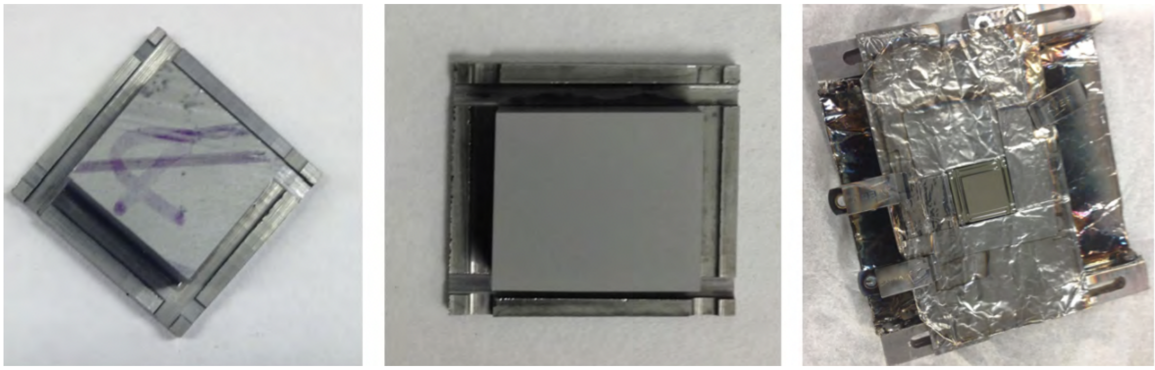

Figure 17: The germanium crystal that has undergone several processes is displayed. Right: crystal put on the jigs with an Al mask after short-term chemical etching. Left: crystal after mechanical lapping. Middle: crystal after long-term chemical etching.

treated in order to create a suitable detector crystal.

The detector's grade crystal is cut with the use of diamond wire saws and grinding bells. The crystal that was formed from Czochralski pullers in the H2 atmosphere was cut into around $2 \times 2 \times 1$ cm^3 cuboid shapes. As seen in Figure 16, each cuboid is further cut into the form of a top hat. The crystals are handled with the help of the wings to protect their delicate surfaces during creation and use. The crystal sample's geometry can be either square or rectangular. During detector manufacture, handling is made simpler by developing square-shaped geometry.

Blade markings are left on the crystal after cutting and grinding. Along the crystal's edge, there could also be minor chips or cracks. Crystals are mechanically lapped to help remove these flaws. Lapping can be delicate and rough. Chips and scratches on the top and bottom surfaces of the crystal can be easily removed with coarse lapping. If both surfaces are flawless and free of obvious chips and scratches, simply fine lapping may be used instead of coarse lapping.

To get a smooth and spotless surface, the already lapped crystal is etched. If there are any faults or micro scratches that were not visible to the naked eye during lapping, they become apparent following the chemical etching procedure. It is preferable to do fine lapping once more if minor scratches are still present after the chemical etching. Lapped crystal pieces are immersed in a 1:4 solution of HF and HNO_3 acids to remove minute surface flaws and rinsed in DI water and dried by using nitrogen gas. The crystal is removed using a Teflon tweezer after the etching is complete, cleaned with DI water, and dried with dry nitrogen gas. If the crystal develops chips or cracks, it should be lapped once more and the etching procedure repeated. Short-term etching can be carried out immediately before the crystal is inserted into the jigs and the sputtering chamber if there are no flaws. If there are visible scratches, then the whole etching process should be repeated. Once the crystal is scratchless, it is loaded in a jig and is ready for contact formation [82, 83].

A crucial process in the construction of the detector is the development of contacts on the Ge crystal. The crystal surface is passivated using an a-Ge contact, which also serves as the charge injection barrier height. Making electrodes for the detector's bias voltage and signal readout from the detector requires the use of aluminum contacts. Al contacts have low resistance, but a-Ge contacts have high resistance. The short-term etched crystal is immediately put on the jigs after etching. When the crystal is placed on the jigs, indium foil is applied to the top of the jigs to prevent scratches. The indium-layered jigs are only touched on the wings of the crystal, which leaves them undamaged and has no impact on the performance of the detector. To reduce the back-sputtering of a-Ge atoms onto the down side of the crystal, an Al foil mask is placed over the etched crystal before putting it into the sputtering chamber. Prior to applying the H2 and Ar gas mixture at a pressure of 14 mTorr, the sputtering chamber is first evacuated to a pressure of less than 4×10^6 Bar. (7:93). Perkin Elmer's model 2400 RF sputtering equipment was utilized for the deposition of a-Ge. Normally, a forward power of 100 watts and a reflected power of 0 watts are maintained and transmitted to the gas mixture. The gas molecules are then ionized to generate plasma, which is then focused towards the area holding the HPGe crystal. Ions are then bombarded toward the a-Ge target. From the target, neutral atoms are expelled, and they land in the Ge crystal. The target was cleaned with pre-sputtering while the shutter was in the closed position for five minutes before to the deposition on the crystal's surface.

Additionally, Al deposition was performed in the sputtering chamber using a DC power source. The procedure is comparable to a-Ge deposition. The key distinction is the use of Ar gas instead of H2 and the placement of Ar gas mixture at 3 mTorr chamber pressure. After deposition, a thickness of 150 nm can be reached in 5 minutes. [82]

Making contacts on the detector is the final stage in the fabrication process. To separate the contacts, a portion of the Al-layer must be scraped from the detector surface. The surfaces where the Al must be maintained undamaged are taped with acid-resistant material using a gentle touch. This tape has a weak bond and leaves no trace when it is removed. To remove air bubbles from the tape on the detector surface, a Q-tip is used to gently push and smooth it out. Then, using Tefon tweezers, the tape-protected detector is handled before being immersed in HF dip solution (1% for 3–4 minutes). The gas bubbles that adhere to the exposed surfaces can be eliminated through agitation. The detector should be removed from the acid immediately. After that, dry nitrogen gas is used to completely dry the detector [84]. It is preferable to quench in methanol rather than DI water if the detector is large since it dries the detector more quickly after the designated amount of time, the solution should be quenched in DI water for a few seconds. The detector could malfunction if Al isn't completely removed from the area outside of the contacts.

A detector's performance can be evaluated using electrical characterization (current-voltage (I-V) and current-voltage (C-V) characteristics) and energy spectroscopy measurements. For big detectors, contact stability is especially desired. Typically, handling a detector entails a number of steps, including as transportation, prolonged storage, and many heat cycles while the operation is being performed. A-Ge contact characteristics vary as a result of prolonged room temperature storage. The Ge detectors fabricated using home-grown crystals at USD were tested in a vacuum cryostat. Figure 19 shows a schematic illustration of the detector characterization setup at USD. The bottom electrode is wired to the indium foil, while the top electrode is wired to the gold-plated pogo pin. The existing configuration at USD enables us to readout signal and leakage current from the top contact and bias the detector through its bottom contact. The connection between the high voltage supply and signal wire was checked using a multimeter after the detector had been loaded inside the cryostat. The cryostat must then be vacuumed to a pressure of around 10^6 Bar before liquid nitrogen can be added to the dewar in the chicken feeder style. The heater and temperature sensor for the vacuum cryostat are mounted at the base of the Al stage. In the vacuum cryostat, a minimum temperature of 78 K was reached. The temperature of the detector was tracked and managed using a LakeShore temperature controller. An hour later, electrical measurements were made in order to give the detector enough time to reach temperature equilibrium with the Al stage. The single top contact is used to record the leakage current and transient signals. Since the leakage current is a direct current (d.c.) signal, it could not pass through the 0.01 F capacitor before the charge-sensitive pre-amplifer but rather the 1 G resistor before the ammeter. However, transient signals, which are a.c. signals, might flow through the capacitor but not the resistor. The charge-sensitive pre-amplifer amplified transient signals [82].

A planar HPGe detector's performance metrics, such as energy resolution, peak-

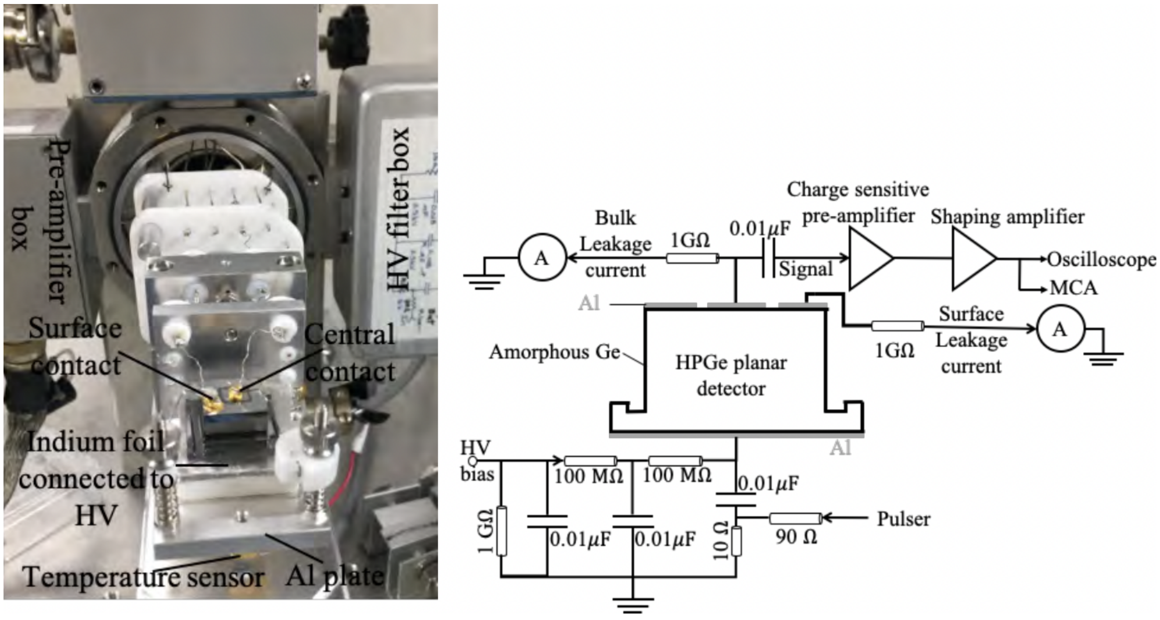

Figure 18: The configuration for cutting and grinding the crystal to give it the desired geometry is shown.

to-background ratio, and efficiency, are often tested using common radiation sources as part of the characterisation process. Cesium (^{137}Cs) and Americium-241(^{241}Am) are few of the popular source for this use. To make sure that the gamma rays or X-rays emitted by the radioactive source are uniformly incident on the detector, the source is positioned a predetermined distance from the detector, usually 5 to 10 cm. In order to eliminate thermal noise and enhance its energy resolution, the detector is chilled to liquid nitrogen temperature (77K). The gamma rays emitted by the radioactive source interact with the detector and produce electrical signals that are amplified and digitized. The resulting energy spectrum can be analyzed using software to determine the detector's energy resolution, peak-to-background ratio, and efficiency. The radioactive source's gamma rays interact with the detector to create amplified and digitized electrical signals. Software can be used to analyze the generated energy spectrum and evaluate the detector's peak-to-background ratio, efficiency, and energy resolution. The detector's capacity to distinguish between gamma rays of various energies is known as its energy resolution. It is usually represented as the photopeak's full width at half maximum (FWHM). The energy resolution is improved when the FWHM is smaller. The energy spectrum's peak intensity to background intensity is measured as the peak-to-background ratio. It evaluates how well a detector can distinguish between signal and noise. A better signal-to-noise ratio is shown by a larger peak-to-background ratio. The percentage of gamma rays released by a radioactive source that are picked up by the detector is its efficiency. It is computed by dividing the number of counts in the photopeak by the rate of radioactive decay, and is commonly reported as a percentage.

The energy spectra collected while the three USD fabricated detectors (USD-RL, USD-8-4-15, USD-R02) [85] were biased at 1200 V in the LBNL vacuum cryostat is shown in Figure 19. They were captured with a ^{137}Cs radioactive source elevated above the detector outside the cryostat. The pulser peak at 662 keV was produced using rectangular pulses with a set amplitude. The commercial companies like ORTEC [86], Mirion [87] also produce high purity germanium detectors whose energy resolution for 1332 keV gamma rays are 1.8 to 2.2 keV which are in the similar range of the detectors we fabricate in the USD. This shows that the high purity germanium detectors are successfully fabricated and characterized in USD lab.

2.5 Conclusion

We have successfully established a production chain for purification of germanium to its fabrication to a high purity germanium detectors here in USD. Zone refining helps to reduce the impurity level to $\sim 10^{11}/\mathrm{cm}^3$ and crystal growth converts it into highly pure single crystals of impurity $\sim 10^{10}/\mathrm{cm}^3$. We have studied the various in-

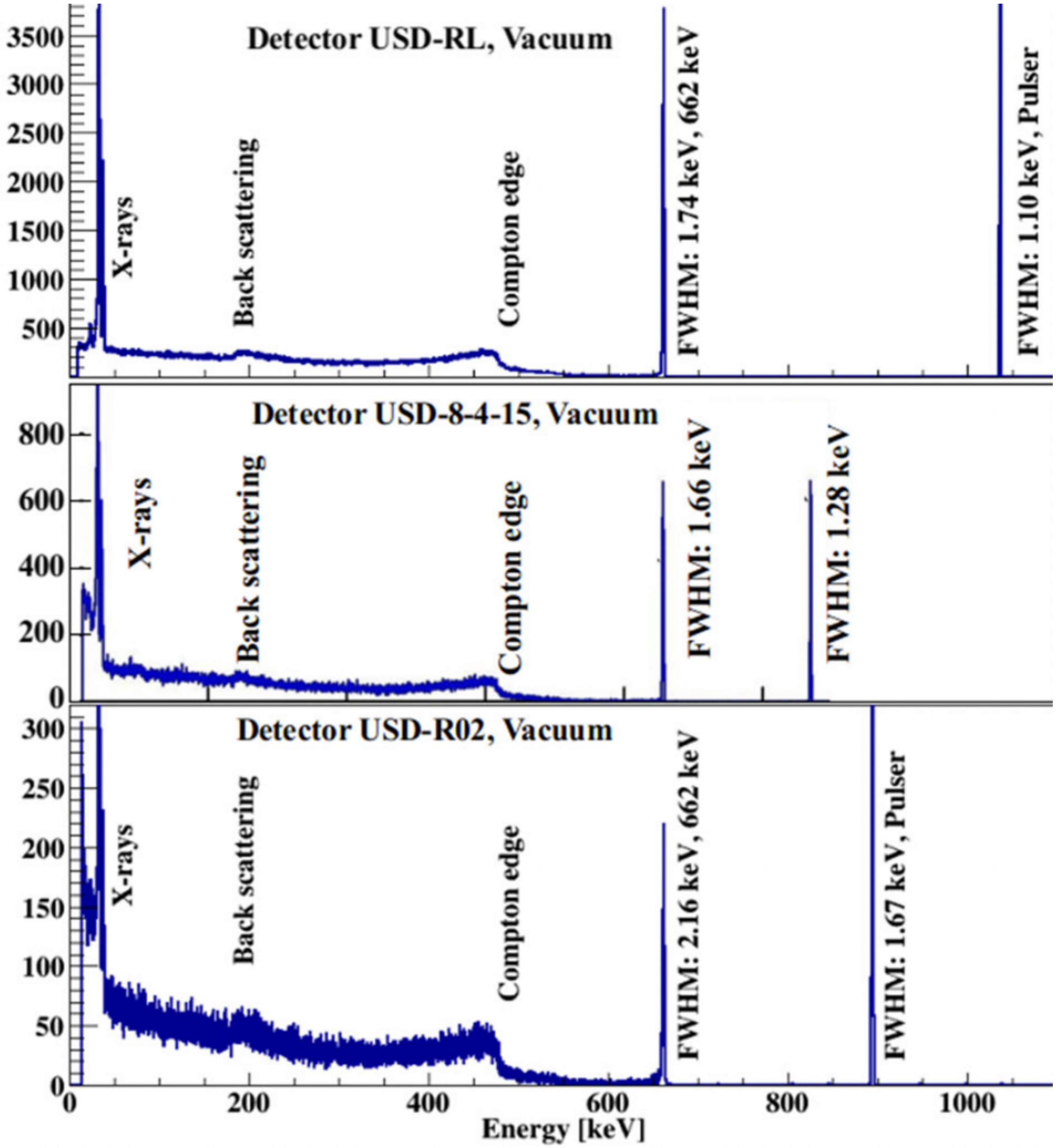

Figure 19: Energy spectra of three USD fabricated detectors, obtained using ^{137}Cs source at the vicinity of the detectors.

fluencing factors in zone refining and the crystal growth. We also successfully have fabricated numerous HPGe detectors from home grown crystals. Hence, research and development activities at USD is contributing a lot in the field of rare event physics.

3 Investigation of the Electrical Conduction Mechanisms in P-type Amorphous Germanium Electrical Contacts for Germanium Detectors in Searching for Rare-Event Physics

A HPGe crystal is fabricated into a planar detector, which is then reversely biased so that it is fully depleted allowing free charge carriers to move. The depletion region acts as an active volume for incident radiation. The energy deposition of incident radiation can be measured by analyzing the interactions in the detector volume [88, 89]. The exposed surface of a Ge crystal is sensitive to contamination. The contaminants deposited on the exposed crystal surface can change the electric field distribution in the detector volume that is in close proximity to the exposed surface and cause a reduction of the resistivity of the surface and hence increase in the surface leakage current. Therefore, a passivation layer is usually applied to protect the exposed surface. This layer should be thin to avoid a large dead layer and it should have large resistivity to prevent excessive leakage current [90, 91]. Amorphous Ge (a-Ge) [92] and amorphous silicon (a-Si) [93] are the most used and accepted passivation layers for semiconductor detectors.

A planar Ge detector fabricated at USD is sketched in Figure 20. It consists of a HPGe crystal passivated with a-Ge on the outer surface. The aluminum contact at the bottom is used to provide high voltage. The aluminum contacts on the top are designated for the measurements of the electrical signal including leakage current. The sources of leakage current are: (1) the bulk leakage current, I_{bulk}, which passes through the interior of the detector due to the injection of charge carriers from the

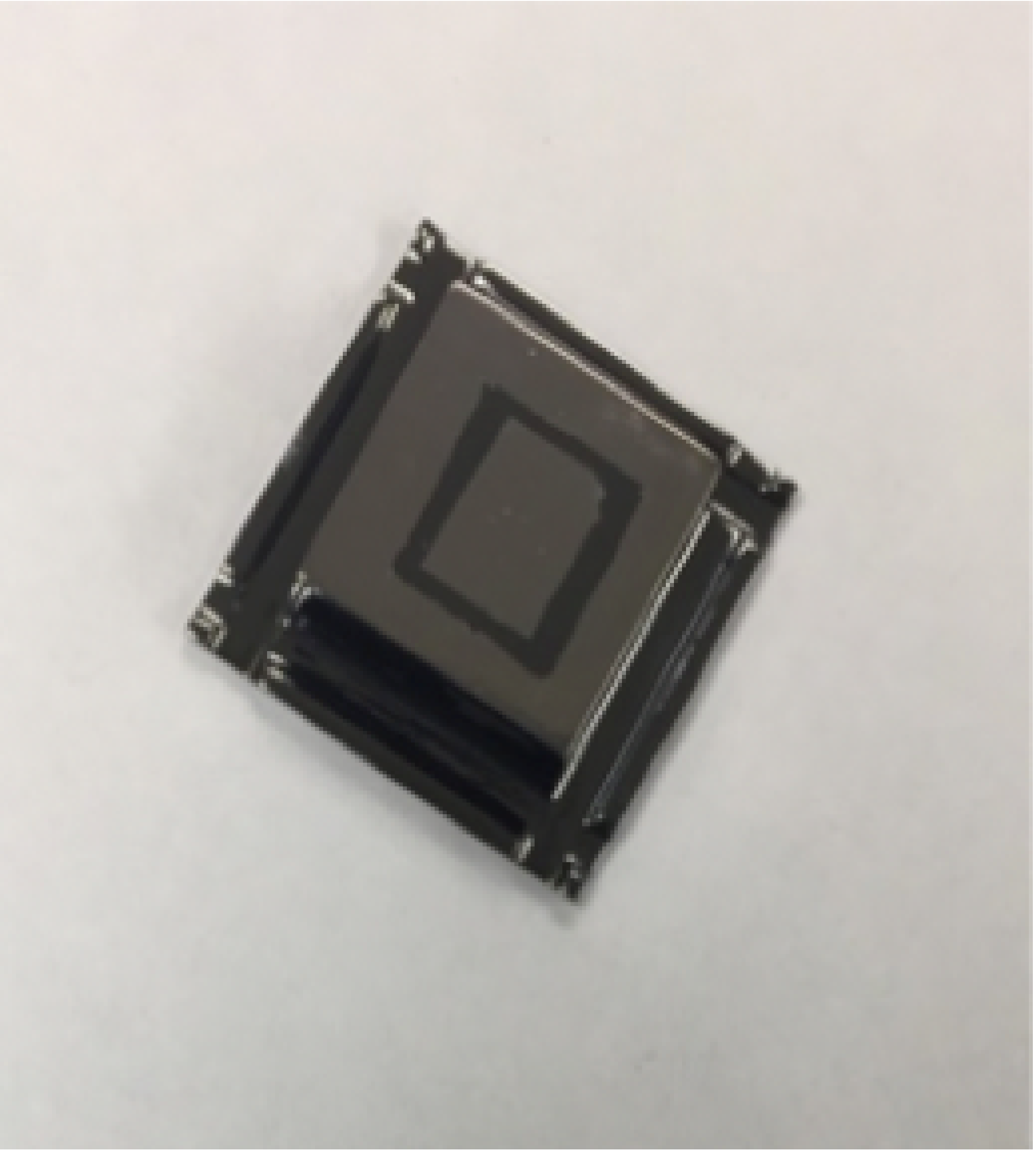

Figure 20: Shown is a Ge detector with a guard ring structure.

contacts and the thermal generation of electron-hole pairs inside the detector volume; and (2) the surface leakage current, I_S, which flows through the outer surface of the detector caused by inter-contact surface channels or carrier generation sites. While the bulk leakage current from the USD-fabricated detectors is discussed in detail by Wei et al. [94], the surface leakage current can be misread as the signal which can degrade the performance of the detector. A detector with a guard-ring structure can be used to separate the surface leakage current from the bulk leakage current, allowing us to study the electrical conduction mechanisms in the a-Ge contacts, as shown in Figure 20. The passivation material should have high sheet resistivity on the order of greater than 10^9 ohm/square [95] to minimize the current flowing through the surface. However, even a small amount of current flow through the side surface of the detector can decrease the performance of the detector significantly. Efforts to reduce the surface leakage current require an understanding of the sources of the surface leakage current, which depends upon the electrical properties of the passivating material - a-Ge. Hence, studying the electrical property of a-Ge is crucial for making better passivating materials and reducing the surface leakage current for Ge detectors.

Electrical conductivity of a-Ge is thought to be dictated by the hopping mechanism through localized defect states [96]. Since the Ge detectors fabricated with a-Ge contacts are used in liquid nitrogen temperature, we are interested in knowing the properties of a-Ge at low temperatures. Generally, the conduction at low temperature in a-Ge occurs via variable range hopping between localized defect states near the Fermi level. Sir Nevill Mott was one of the first to give a theoretical description of low temperature hopping conductivity in strongly disordered systems [96, 97]. In 1969 he introduced the concept of Variable Range Hopping to describe how the long jumps govern the conductivity at sufficiently low temperatures.

The electrical conductivity (σ) of amorphous semiconductors at low temperature (T) obeys the Mott's relation

$$\sigma = \sigma_0 e^{-(T_0/T)^{1/4}}, \tag{9}$$

where σ_0 is the conductivity prefactor and T_0 is the characteristic temperature given by

$$T_0 = 16\alpha^3/kN(\epsilon_f), \tag{10}$$

where α is the inverse of localization length and $N(\epsilon_f)$ is the density of defect states near the Fermi level and k is the Boltzmann constant. If we take log of both sides of Equation 9 and plot the log of conductivity on the y-axis and $T^{-1/4}$ on the x-axis, then we obtain a straight line, the slope of which gives the value of the characteristic temperature T_0 and the y-intercept gives the prefactor σ_0.

The energy between two localized states (hopping energy) at temperature T is given by

$$W_{HOP} = 1/4kT(T_0/T)^{1/4}, \tag{11}$$

and the spatial distance between two hopping sites at temperature T (hopping distance) is

$$R_{HOP} = 3/8(T_0/T)^{1/4} \times 1/\alpha. \tag{12}$$

In general, the Mott's parameter for a-Ge should be determined through the standard experimental procedure by coating the a-Ge layer onto the surface of an isolating material such a glass substrate. However, one would also like to know the electrical properties of a-Ge coated on the surface of Ge detectors using an well-established fabrication procedure. The goal of this work is to understand the impact of the fabrication procedure on the electrical properties of a-Ge. The variation of the electrical properties between three detectors will provide a range of the surface leakage current for the fabrication procedure and allow us to evaluate if this fabrication procedure can deliver a negligible surface leakage needed for detecting single electron-hole pair at cryogenic temperature.

We have obtained the values of the localization length ($1/\alpha$), the hopping energy, and the hopping distance of a-Ge for three detectors fabricated at USD. The purpose of this study is to characterize the a-Ge thin layer we created to passivate Ge detectors by comparing our results with the previous work done on similar materials. With such a characterization, we can revisit our fabrication process to improve the quality of the passivated material and reduce human error, thereby improving the detector performance.

3.1 Experimental procedure

Three HPGe detectors with guard structure, as shown in Figure 20, were fabricated with p-type a-Ge passivation in order to study the electrical properties of a-Ge. Since the planar detector is easier to be fabricated than other geometries and large-size detectors are not required for our study, all detectors used in this work were fabricated into a planar geometry. A RF sputtering machine was used to sputter a-Ge on all surfaces of the crystal. The thickness of a-Ge, the gas composition of the sputtering process, the pressure, and the applied power can be changed in the fabrication. In this work, a precisely cut crystal in a planar geometry was placed on the jig and loaded into the chamber of the sputtering machine. The plasma was created in the chamber with a mixture of hydrogen and argon gas (7:93) at a pressure of 14 mTorr. The thickness of the a-Ge deposited on the side surface of the crystal is 556 nm and on the top and bottom surfaces of the detector is 1.2 μm. Although the same deposition apparatus and the same deposition parameters are used to create the a-Ge layers, it is very difficult to maintain the homogeneity of the recipe for detector fabrication process, for example, the time-dependent surface re-oxidation. This may have led to difference in the conductivity of a-Ge for different detectors. This is a main goal of this work to find out the variation of the electrical properties of a-Ge using three detectors fabricated with the same procedure. Additionally, the quality of crystal used to fabricate these detectors and their net impurity concentration, the density of defects, the time since the fabrication, the storage and the handling of the detectors may also contribute to the differences in the electrical properties of a-Ge coated on the Ge detectors.

After a-Ge was deposited on all surfaces of the crystal, then the detector USD-R02 was loaded into the chamber of an Edwards Electron Beam Evaporator to make the aluminium contacts. An electron beam produced from a tungsten filament bombards the aluminum target. Under high vacuum, the electron beam can reach the crucible without interference. A voltage of 4.89 kV and a current around 35 mA were provided to have a stable data rate of 0.2 to 0.3 nm/s. Note that for the detectors USD-W03 and USD-R03, the aluminium deposition was carried out by sputtering process. The plasma was created in the chamber with argon gas at a pressure of 3 mTorr. A typical thickness for the aluminum contacts was 100 nm. The details are described in an earlier publication from our group [98]. Only the top and bottom surfaces need aluminum contacts to test the electrical properties of a detector. To remove aluminium contacts from the sides, a mask of acid-resisted tape was placed on the top and bottom. Then, the detector was dipped into the acid solution with one percent of HF for a few minutes, until all of the aluminum was etched away from the sides. Note that HF does not remove the a-Ge layer beneath the aluminium.To characterize the electrical properties of a detector, the Ge crystal was loaded into the cryostat, as depicted in Figure 21. After the pressure reaches the order of 10^{-6} mBar, LN$_2$ was added into the Dewar. The temperature of the detector was controlled by the Lakeshore temperature controller. The detector was started at a bias around 50 V and was biased up to 2500 V. The bias voltage was provided to the bottom contact of the detector and the signal was read out from the top contacts. Current-voltage (I-V) characteristic of the surface current for all three detectors was performed by using a transimpedance amplifier, which converts current into voltage. The voltage is then measured by a precision voltmeter. This voltage was then converted back to current, as described in a recent paper from our group [94]. The I-V characteristic of two detectors (USD-R03 and USD-WO3) was done at three different temperatures 79 K, 90 K and 100 K, while the I-V characteristic of the detector USD-RO2 was done at 85 K, 90 K, 95 K and 100 K.

3.2 Result and discussion

Utilizing the first order approximation, the reciprocal of the slope of the I-V curve measured at different temperatures gives the resistance (R) of the a-Ge contact layer. As an example, Figure 22 shows the surface leakage current versus the applied bias voltage for USD-W03 detector. Using this method, we obtained the values of the resistance corresponding to the measured temperatures for three detectors and the results are shown in Table 3. The resistivity (ρ) for a layer of a-Ge with a thickness t on a detector, with a length of sidewall l and a width w, was calculated using Ohm's law:

$$\rho = 4Rtw/l + 4Rtw^{'}/l^{'}, \tag{13}$$

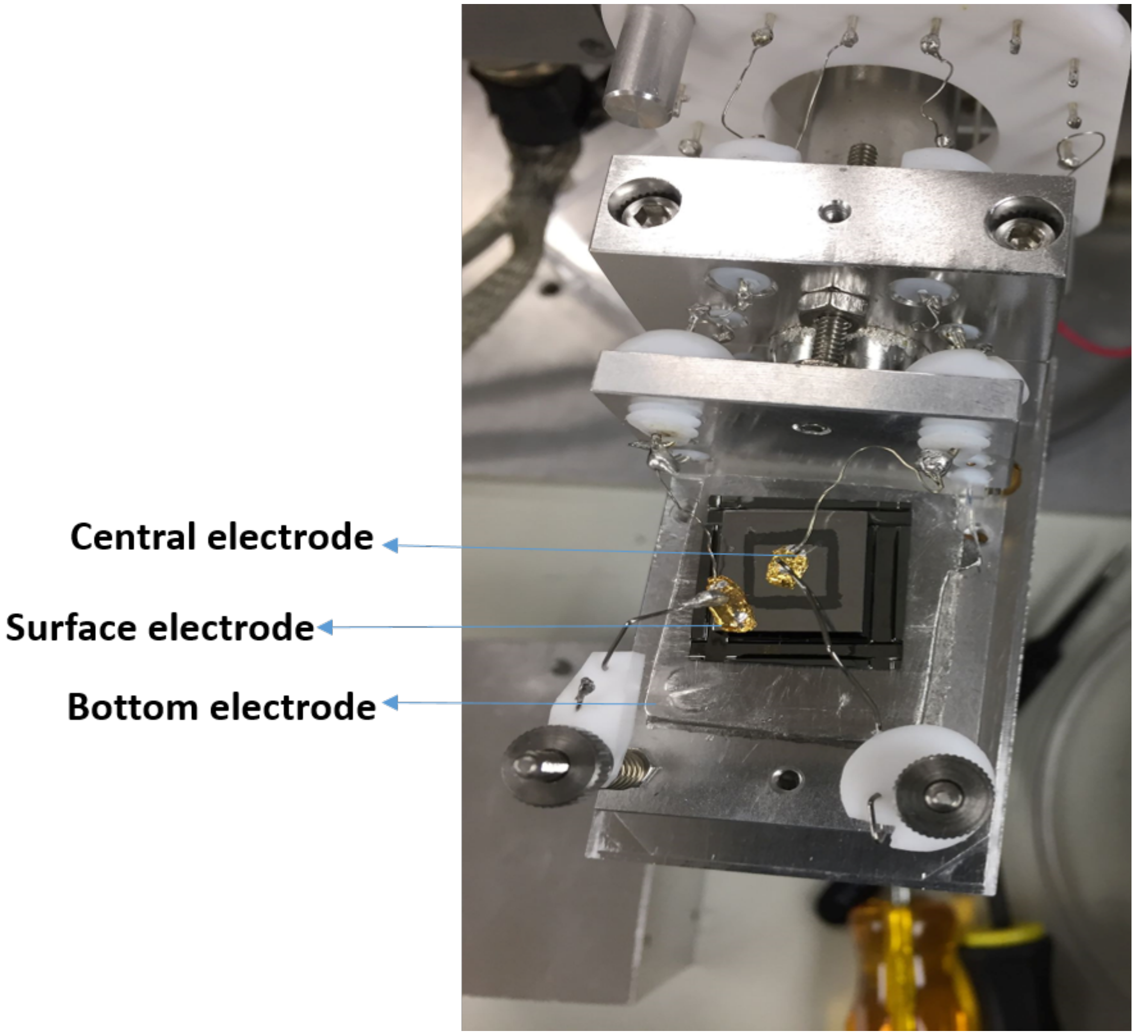

Figure 21: A detector is loaded into a cryostat for I-V measurement at desired temperatures.

where the constant 4 incorporates the four-side walls of the planar detector, $w^{'}$ represents the width of the wing on the bottom surface of detector and $l^{'}$ is the total length of the groove along which the current flows. A small distance on the top surface from the guard ring to the side surface which contains aluminium was neglected in this study because the resistivity of aluminium is much less than that of a-Ge. The thickness and the width for USD-R02 are 0.65 cm and 1.4 cm, respectively. For USD-R03, the thickness and the width are 1.6 cm and 0.81 cm. For USD-W03, the thickness and the width are 0.94 cm and 1.16 cm. For all detectors the value of t is 556 nm, $w^{'}$ is 2 mm and $l^{'}$ is 4.5 mm. Apart from the surface leakage current, the leakage current from the bulk of the detector is also contributed to the surface channel of the detector. This current should be subtracted from the surface leakage current in order to study the electrical properties of a-Ge. A theoretical model that describes the current voltage relationship for amorphous-crystalline heterojunction was developed by Döhler and Brodsky [99, 100]. For a-Ge coated on the surface of Ge, the energy barrier height for hole and electron injections are represented by ϕ_h and ϕ_e, respectively; the effective Richardson constant is A, the barrier lowering terms are $\Delta\phi_h$ and $\Delta\phi_e$, which account for the lowering of hole and electron energy barrier height, respectively due to the penetration of the electric field into the a-Ge contacts. Putting all of these parameters in an equation, the current density J is given by [99, 100]

$$\begin{gathered} J = A^{*}T^{2}exp[-(\phi_h - \Delta\phi_h/kT)], \\ \text{where } \Delta\phi_h = \sqrt{2qV_aN_d/N_f}, \end{gathered} \tag{14}$$

	Detector's Resistance(Ω)		
Temperature	USD-R03	USD-R02	USD-W03
79	2×10^{14}	-	5×10^{14}
85	-	1.1×10^{14}	-
90	2×10^{13}	2.5×10^{13}	1.4×10^{13}
95	2.5×10^{12}	1×10^{13}	5×10^{12}
100	-	5×10^{12}	-

Table 3: The calculated values of the resistance from the I-V curves for three USD fabricated detectors.

and

$$\begin{gathered} J = A^{*}T^{2}exp[-(\phi_e - \Delta\phi_e/kT)], \\ \text{where } \Delta\phi_h = \sqrt{\epsilon_0\epsilon_{Ge}/N_f}(V_a - V_d)/t. \end{gathered} \tag{15}$$

Note that the Equations 14 and 15 represent the current density before and after the full depletion of the detector, respectively. N_d is the net ionized impurity concentration of the detector, N_f is the density of localized energy states (defects) near the Fermi level in a-Ge, k is the Boltzmann constant, ϵ_0 is the free-space permittivity, ϵ_{Ge} is the relative permittivity for Ge, V_d is the full depletion voltage and t is the detector thickness, q is the magnitude of the electron charge, V_a is the applied biased voltage. The sum of Equations 14 and 15 give the total current density after the detector is fully depleted. The current injected into the bulk from the contacts was calculated by using the area of the aluminium contact outside the guard ring. These areas for USD-R02, USD-R03 and USD-W03 were 1.79 cm^2, 1.84 cm^2 and 0.98 cm^2 respectively. The values of $\Delta\phi_h$, ϕ_h and N_f have been calculated for these detectors in our group [94].

The results for the calculated conductivity are shown in Table 5.

The variation of conductivity with temperature is studied for three different detectors, as shown in Figure 23. The slopes of the fitted straight lines are used to

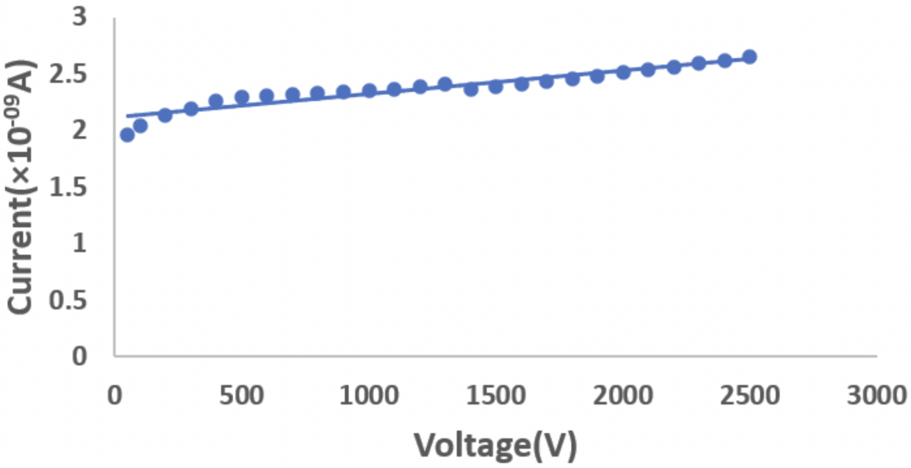

Figure 22: The surface leakage current (I) versus voltage (V) for USD-W03 at 95 K. The reciprocal of the slope of this line gives the resistance at 95 K.

Detector	USD-R03			USD-R02				USD-W03		
Temperature (K)	79	90	95	85	90	95	100	79	90	95
Conductivity($10^{-12}\Omega^{-1}cm^{-1}$)	3.5	35.0	280.1	6.1	27.1	68.1	130.6	1.5	55.1	157.3

Table 4: The calculated values of the conductivity (σ) for three USD-fabricated detectors.

calculate the characteristic temperature (T_0) and the intercepts are used to obtain the conductivity prefactor (σ_0) for three a-Ge layers used as the contacts for three Ge detectors. The electrical conductivity of the a-Ge sputtered on a HPGe detector in the low temperature range was studied by Amman et al. [101]. The a-Ge contacts fabricated in this work was performed using a similar recipes (7% Hydrogen, 11 mTorr pressure). There is a significant variation of conductivity of a-Ge measured in this work with the similar work done by Amman et al. In the referred work a-Ge was sputtered on a glass substrate and the pressure used to sputter was 11 mTorr. We used 14 mTorr pressure with same hydrogen argon composition ratio and the substrate we used was a HPGe crystal. The differences in the conductivity can affect the values of the Mott's Parameter. Therefore, the Mott's parameters should be determined for a-Ge fabricated with a specific machine. The three detectors used in this study show similar ranges of conductivity. Thus, the values of the localization length, the hopping energy and the hopping distance reported in this work are for the USD fabricated detectors. Table 5 shows the calculated characteristic temperature (T_0) and the conductivity prefactor (σ_0) for three USD-fabricated detectors. Although the a-Ge layers in three detectors have similar thickness, the measured values of the density of defects N_f and the barrier heights ϕ_h and ϕ_e are different [94]. Also the net impurity concentration for all the detectors is different so that the barrier lowering term $\Delta\phi_h$ and $\Delta\phi_e$ for the a-Ge layers are different. The fabrication handling process and the time of storage of these detectors are also different. These factors may have contributions to the time-dependent surface re-oxidation, which contributes to the difference in the measured properties of the a-Ge coated on the surface of Ge detectors.

The value of the characteristic temperature T_0 is calculated for each detector from the slope of these plots in Figure 23. The variation of T_0 reflects the difference in

Detector	T_0 (K)	$\sigma_0(\Omega^{-1}\text{cm}^{-1})$
USD-R02	3.04×10^9	2.30×10^{22}
USD-W03	9.19×10^9	2.03×10^{33}
USD-R03	5.77×10^9	4.16×10^{28}

Table 5: The calculated values of characteristic temperature (T_0) and conductivity prefactor (σ_0) for three USD-fabricated detectors.

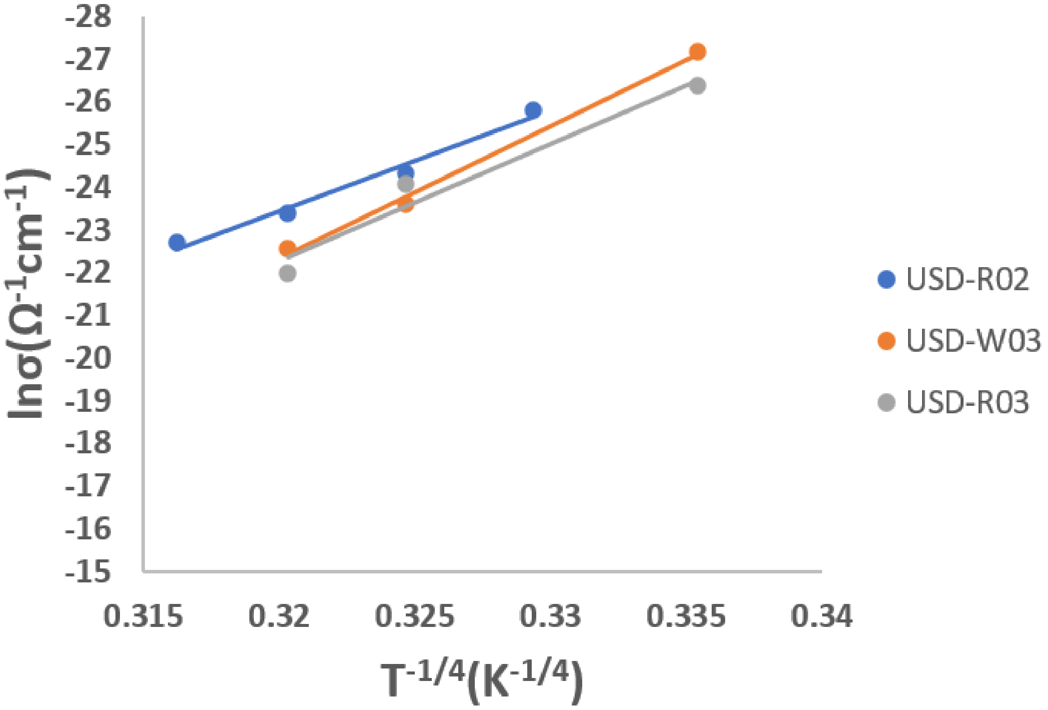

Figure 23: The variation of conductivity with temperature for detectors USD-R02, USD-R03 and USD-W03. The slope of the plot for USD-R02 is found to be -234.2 and the Y-intercept is 51.5. Similarly, the slope for USD-R03 is found to be -275.6 and the Y-intercept is 65.9. Likewise, the slope and the Y-intercept for USD-W03 are found to be -309.6 and 76.7, respectively.

Detector	USD-R03			USD-R02			USD-W03		
Temperature	$1/\alpha$(A°)	W_{HOP}(meV)	R_{HOP}(A°)	$1/\alpha$(A°)	W_{HOP}(meV)	R_{HOP}(A°)	$1/\alpha$(A°)	W$_{HOP}$(meV)	R$_{HOP}$(A°)
79	$2.2^{-0.26}_{+0.58}$	157.2	75.9	$5.07^{-0.83}_{+2.58}$	-	-	$2.13^{-0.05}_{+0.07}$	176.6	82.5
85	$2.2^{-0.26}_{+0.58}$	-	-	$5.07^{-0.83}_{+2.58}$	141.5	147.0	$2.13^{-0.05}_{+0.07}$	-	-
90	$2.2^{-0.26}_{+0.58}$	173.3	73.5	$5.07^{-0.83}_{+2.58}$	147.7	144.9	$2.13^{-0.05}_{+0.07}$	194.7	80.0
95	$2.2^{-0.26}_{+0.58}$	180.5	72.5	$5.07^{-0.83}_{+2.58}$	153.8	143.0	$2.13^{-0.05}_{+0.07}$	202.8	78.8
100	$2.2^{-0.26}_{+0.58}$	-	-	$5.07^{-0.83}_{+2.58}$	159.8	141.1	$2.13^{-0.05}_{+0.07}$	-	-

Table 6: The measured values of the localization length, the hopping energy and the hopping distance for three USD detectors.

the density of states near the Fermi level for three different a-Ge layers. The values of the density of states near the Fermi level $N(\epsilon_f)$ for these detectors are obtained in a recent paper from our group [94]. The value for USD-R02 is found to be $\mathrm{N}(\epsilon_f) = (4.68 \pm 3.32) \times 10^{17}$ eV/cm^3. Since there are two values of $\mathrm{N}(\epsilon_f)$ corresponding to two contacts for USD-R03, we simply take the average of these two values to obtain the density of states for USD-R03 and the average value used to calculate the Mott's parameter in this study is $N(\epsilon_f) = 3.08^{+1.36}_{-1.58} \times 10^{18}$ eV/cm^3. Similarly, the average value of density of states for USD-W03 is found to be $N(\epsilon_f) = 2.1^{+0.17}_{-0.20} \times 10^{18}$ eV/cm^3. With these values of $N(\epsilon_f)$ and T_0 determined and the Boltzmann constant k, the value of α can be calculated using the equation 10. The calculated values of the localization length for detector USD-R02, USD-R03 and USD-W03 are $5.07^{-0.83}_{+2.58}$ A°, $2.2^{-0.26}_{+0.58}$ A°, and $2.13^{-0.05}_{+0.07}$ A°, respectively. Table 6 displays the results obtained in this work. The errors are dictated by the errors from the density of states near the Fermi level.

The values of the localization length obtained for the a-Ge fabricated at USD are less than the values reported previously [102, 103, 104]. This difference in localization length can be attributed to the difference in the fabrication of a-Ge between the previous work and our work. The previous work referenced in this work used pure a-Ge, while we used hydrogenated a-Ge. A similar work on hydrogenated a-Si was reported and their results are comparable to our work [105]. The value of the localization length is directly related to the density of defects $N(\epsilon_f)$ and T_0. The amount of hydrogen reduces the density of defect states significantly and hence increases the resistivity of a-Ge. This suggests that a-Ge can be fabricated with or without hydrogen content, depending on the applications. If high resistivity is preferred, such as the passivation for Ge detectors, the a-Ge should be fabricated with hydrogen content. If low resistivity is needed, such as solar cells, the a-Ge should

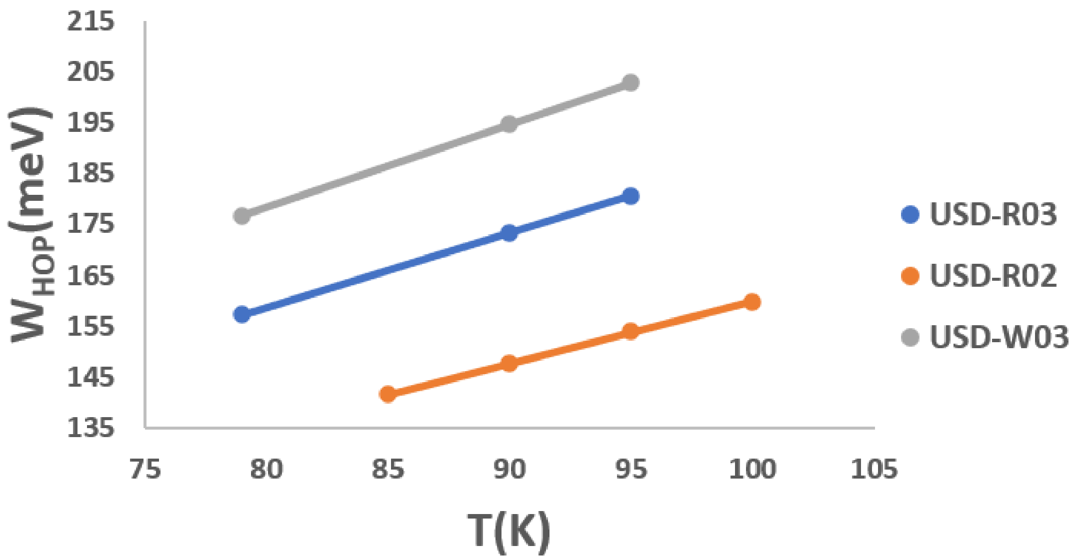

Figure 24: Shown is the variation of hopping energy with temperature for three different detectors.

be made without hydrogen content. This is to say that if the recipe of a-Ge deposition is modified, then the film's resistivity [101, 106] and hence the Mott's parameter are impacted by the fabrication process. Because we determine the electrical property of hydrogenated a-Ge passivated on HPGe detectors deposited by sputtering method and the referenced work considers pure a-Ge on a thin films on a substrate by the evaporation method, the difference in the localization length can be expected. However, all the calculated values of the localization length are in the acceptable range [104, 103, 105, 102].

In addition, the hopping energy and the hopping distance are calculated for each of the detectors using equations 11 and 12, respectively. The variation of hopping energy W_{HOP} with temperature (T) is also studied for all three detectors, as shown in Figure 24.

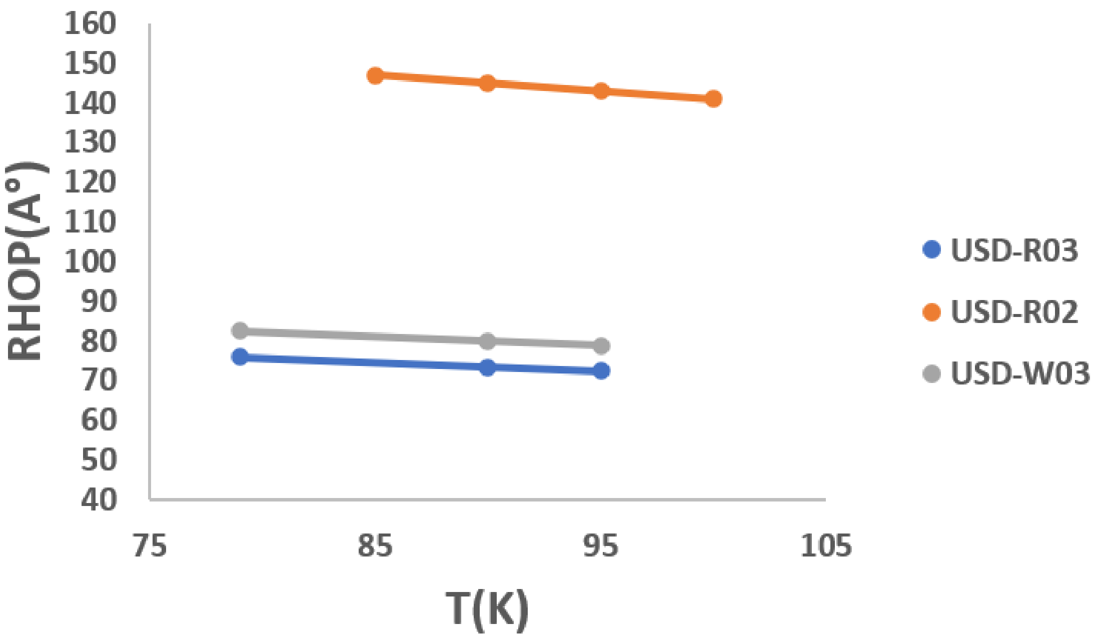

Figure 25: The variation of hopping length versus temperature for three different detectors.

The value of hopping energy increases with the increase in temperature. We obtain a larger value of T_0 as compared with a similar work for the a-Ge made without hydrogen. This indicates that the value of hopping energy is larger in our a-Ge. A larger hopping energy means that the charge carriers jumping from one defect state to another defect state for conduction require higher kinetic energy, which make the conduction process difficult and hence the material is highly resistive. Similarly, the variation of hopping length R_{HOP} with temperature (T) is also studied as shown in Figure 25.

From this study we find that the hopping length R_{HOP} decreases with increasing in temperature. R_{HOP}, as indicated in Equation 12, is small for small values of localization length. Thus, the wave function is more localized for trapping charges, making it difficult for them to hop to other trap states, resulting in the increase of resistance and hence the resistivity. The calculated values of R_{HOP} and the localization length ($1/\alpha$) are lower than the similar work reported previously without hydrogen content. This suggests that the a-Ge created with hydrogen has higher resistance and resistivity, suitable for passiviting Ge crystals when making Ge detectors.

3.3 Conclusion

We have determined the values of the Mott's parameters for three a-Ge layers used as planar Ge detector contacts fabricated at USD. As a result, we find that the localization length of a-Ge is on the order of $2.13^{-0.05}_{+0.07}$ A° to $5.07^{-0.83}_{+2.58}$ A°, depending on the density of states near the Fermi energy level within bandgap. The hopping energy ranges from 141.5 meV to 202.8 meV and the hopping distance varies from 72.5 A° to 147.0 A°, depending largely on temperature. We find that the hopping energy in a-Ge increases as temperature increases while the hopping distance in a-Ge decreases as temperature increases. Our results are different from that of pure a-Ge fabricated without hydrogen content, but comparable to a-Si fabricated with hydrogen content. This study confirms that the amount of hydrogen can reduce the density of defect states near the Fermi level significantly and hence can increase the resistivity of a-Ge. Subsequently, the values of the characteristic temperature T_0 and the localization length ($1/\alpha$) obtained in this study indicate a high resistivity of the a-Ge fabricated with hydrogen content at USD. The high resistivity of a-Ge is an essential characteristic of a good passivation material for HPGe detectors. The variation of the hopping energy, the hopping distance, and the localization length in three different a-Ge layers corresponds to the difference in the density of states near the Fermi level, which reflects the variation of the fabrication process for making a-Ge layers. The time-dependent re-oxidation and personal errors in the fabrication process may also have led to difference in these parameters. An in-depth study of the effects of surface re-oxidation is mandatory to reduce the scattering in the measured values in order to achieve the complete control of the production process of HPGe detectors. The values of the parameters calculated in this study shows that the a-Ge fabricated at USD to passivate Ge detectors meet the criteria for passivation.

4 Solar neutrinos

coherent elastic neutrino nucleon scattering (CEvNS) has not been used for detecting pp neutrinos because of the low amount of energy transferred to a nucleus during the interaction. However, utilizing internal charge amplification, the charge carriers created by phonon excitation can be used to detect pp neutrinos because of the extremely low energy threshold of the detector[107]. In addition, the size of the detector can be dramatically reduced. The event rate from CEvNS is much higher than that of elastic neutrino-electron scattering. The differential neutrino-nucleus cross section $d\sigma_{CNS}(E_\nu, E_{NR})/dE$ for a neutrino of energy E_ν (eV) is given by

$$\frac{d\sigma_{CNS}(E_\nu, E_{NR})}{dE_{NR}} = \frac{{G_F}^2}{4\pi}{Q_w}^2 m_N(1 - \frac{m_N E_{NR}}{2{E_\nu}^2})F^2(T_R) \tag{16}$$

where E_{NR} is nuclear recoil energy, m_N is the mass of the target nucleus, G_F is the Fermi Coupling constant, Q_w=$N - (1 - 4sin^2\theta_w)Z$ where N the number of neutrons and Z is the number of protons and θ_w the weak mixing angle. Here, the value of the form factor $F(T_R)$ is equal to 1 [108]. Likewise, the differential event rate for a detector of mass M and exposure time T is given by

$$\frac{dE}{dE_{NR}} = N_T \times M \times T \times \frac{d\sigma_{CNS}(E_\nu, E_{NR})}{dE_{RN}} \times \frac{dN_\nu}{dE_\nu} \tag{17}$$

where N_T is the number of target nuclei per unit mass and $\frac{dN_\nu}{dE_\nu}$ is the differential neutrino flux. Figure 27 shows the expected event rate as a function of nuclear recoil energy induced by solar neutrinos in a Ge detector. Through CEvNS, we can detect pp neutrinos in different flavors $(\nu_e, \nu_\tau, \nu_\mu)$ without considering the neutrino oscillation. This leads to the determination of total neutrino flux in the detector. Similar to the SNO experiment, which determined the total ^8B neutrino flux and

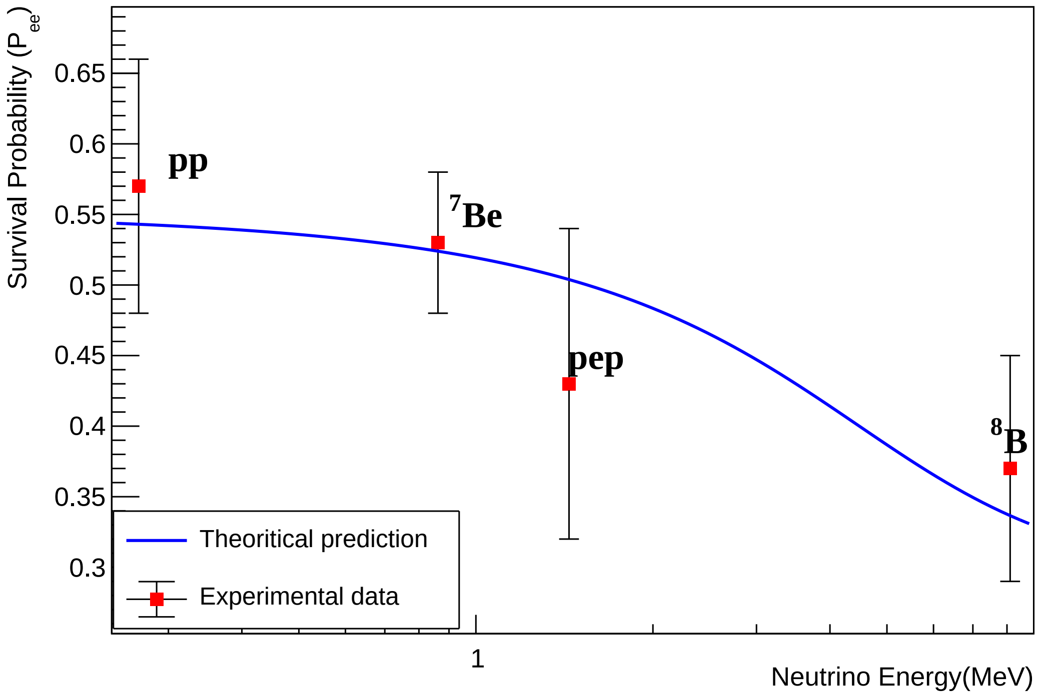

Figure 26: Survival Probability of solar neutrinos [51].

hence proved the neutrino flavor transition, measuring the total pp neutrino flux will verify the standard solar model and the neutrino flavor transition at lower neutrino energy when combined with the global measurements for the solar neutrino survival probability, as shown in Figure 26.

Below, we demonstrate how pp neutrinos can be measured more accurately with the proposed Ge detector that uses phonons generated by neutrinos via CEvNS

4.1 Internal charge amplification

In germanium detectors, the area of the device where the signal produced by an incident particle is amplified before it is read out is referred to as the internal amplification section. The signal-to-noise ratio must be increased and the sensitivity

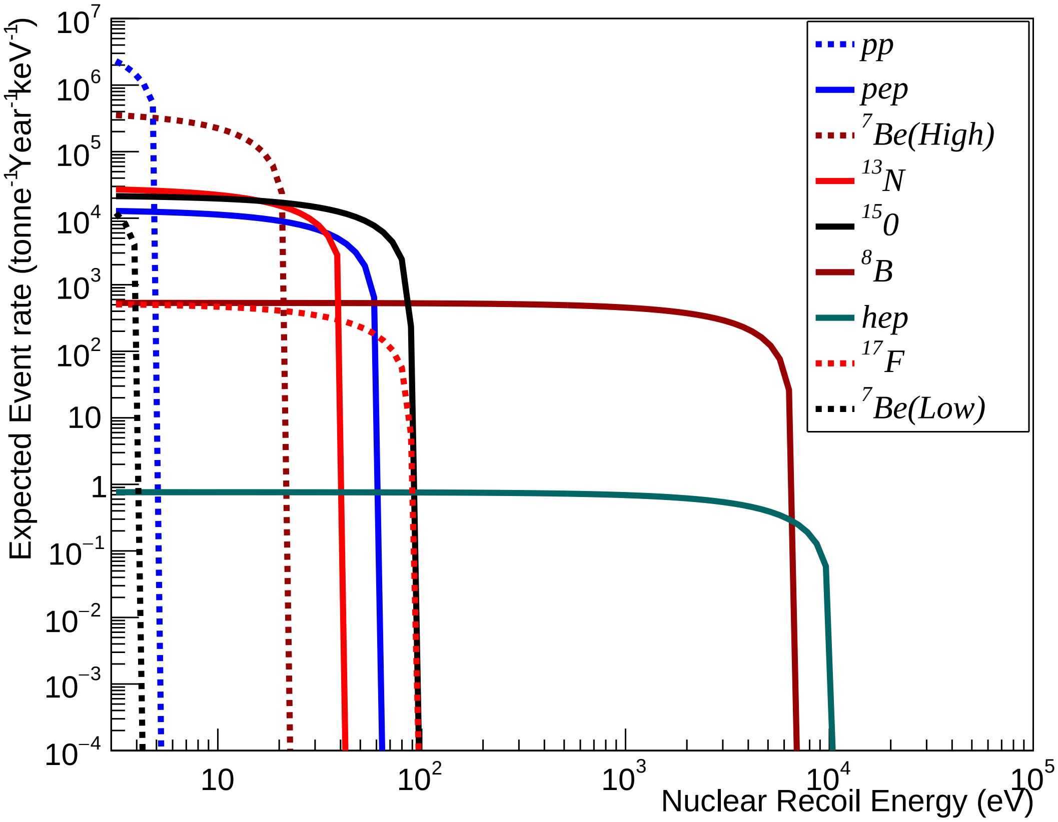

Figure 27: The expected event rate versus nuclear recoil energy produced by solar neutrinos in a Ge target. The label of y-axis is the event rate in a Ge detector for different solar neutrinos in the unit of tonne^{-1}year^{-1}keV^{-1}. This gives the event rate produced by solar neutrinos (the flux is in the unit of cm^{-3}sec^{-1}keV^{-1}) in a Ge detector corresponding to the nuclear recoil energy (in the level of keV) induced by solar neutrinos interacting with Ge nuclei. Here, keV stands for kilo electron volts.

Type	Maximum nuclear recoil (eV)	Total Event ($\mathrm{kg}^{-1}\mathrm{year}^{-1}$)
pp	5.29	16.58
pep	61.32	0.46
hep	10386.03	0.001
$^{7}Be_{low}$	4.27	0.11
$^{7}Be_{high}$	21.87	4.98
^{8}B	6654	1.86
^{13}N	42.58	0.67
^{15}O	88.71	1.09
^{17}F	89.53	0.03

Table 7: Maximum nuclear recoil and total event rate integrated for solar neutrinos.

of the detector must be increased through the amplification procedure.A significant advancement in gamma-ray spectroscopy was the creation of Lithium-drifted Germanium (Ge(Li)) detectors with an internal amplification section. These detectors were frequently employed for gamma-ray spectroscopy in the 1960s and 1970s after being initially reported by Goulding et al. in 1964[109]. Due to their reduced energy resolution and other drawbacks, Ge(Li) detectors are no longer employed as frequently as PPC detectors, but they nonetheless mark a significant advancement in the field of germanium detectors

Achievements: The energy resolution and sensitivity of germanium detectors have considerably increased over the past several decades with the usage of p-type point contact (PPC) germanium detectors with an internal amplification section. Luke et al. reported the 1991 [110] first demonstration of PPC detectors with internal amplification. Since then, numerous advancements have been made to the design and manufacture of PPC detectors, resulting in a typical energy resolution of 0.1% at 1 MeV. Limitations: The high degree of electrical noise, which can impair energy resolution and reduce the detector's sensitivity, is one of the main drawbacks of internal amplification in germanium detectors. Many techniques have been devised to reduce this noise, including lowering the detector's working temperature, utilizing specific preamplifiers, and applying cutting-edge digital signal processing algorithms[111, 112]. The size of the detectors, which is normally restricted to a few centimeters in diameter due to the challenge of maintaining uniform amplification across a greater region, is another restriction. This reduces the detector's effectiveness and sensitivity to low-energy gamma rays and other particles. To increase the uniformity of amplification, several methods have been devised, including the use of segmented detectors [113].

In conclusion, over the past few decades, internal amplification in germanium detectors has significantly advanced the sensitivity and energy resolution of gamma-ray spectroscopy. However, to fully exploit the promise of germanium detectors for scientific study, further developments in detector design and signal processing techniques would be required. Electronic noise and size restrictions remain key difficulties for the area.

4.2 The working principle of the proposed detector

Starostin et al. [107] have proposed a detector that can be used to amplify the signal generated by the pp solar neutrinos. It is assumed to be made from a 1.0 kg HPGe crystal. The net impurity concentration in the detector will be (1-3)$\times 10^{10}$ cm^{-3}. It will be a multi-strip planar Ge detector having a dimension of 9 cm × 7 cm × 3 cm with 15 anode strips fabricated using the photo-mask method each of width 20 μm. The fiducial volume of the detector will be about 190 cm^3 [58, 107]. The detector concept and its working principle were discussed in detail in our earlier publication [58]. The main conclusions are:

1. After purifying Ge ingots to a level of $\sim 10^{11}$ cm^{-3} by zone refining [114], a single crystal can be grown at the University of South Dakota (USD) through the Czochralski method [115]; during the crystal growth process, impurities can be further removed from the grown crystal down to a level of $\sim 10^{10}$ cm^{-3} or below [116].

2. It has been found that the remaining impurities are mainly aluminum (Al), phosphorous (P), boron (B), and gallium (Ga) in the USD-grown crystals [115]; the ionization energies of these impurities in Ge are in a level of $\sim$0.01 eV, which is less than the longitudinal acoustic (LA) phonon (0.04 eV) and the transverse (TA) phonon (0.026 eV) generated by neutrinos via coherent neutrino-nucleus elastic scattering [117, 58]; hence the phonons can certainly excite or ionize these impurities to produce charge carriers.

3. These charge carriers would then be drifted towards the electrical contacts. During the drifting process, these charge carriers would be accelerated by a high electric field to generate more charge carriers and hence, amplify the charge by a factor of $\sim$100 to $\sim$1000, depending on the applied electric field.

4. The absorption probability P of phonons in a given Ge detector can be estimated as

   $$P = 1 - exp(-d/\lambda) \tag{18}$$

   where d is the average distance diffused before an anharmonic decay and $\lambda = \frac{1}{\sigma \times N_A}$ is the mean free path of phonons with N_A being the net impurity level in a given p-type detector and σ is the cross section of phonons absorbed by neutral impurities [58].

5. Similarly, the ionization or excitation probability ($f(E_A)$) of a neutral accep-

tor state to be ionized is given by

$$f(E_A) = 1 - \frac{1}{1 + 4e^{(E_A - E_F)/k_B T}} \tag{19}$$

where E_A is the binding energy of a p-type impurity at its neutral state, E_F is the Fermi energy level, E_V is the energy level of valence band in Ge, and $(E_F - E_V) = k_B T ln(N_V/N_A)$ with $N_V = 2(2\pi m^* k_B T/h^2)^{3/2}$ being the effective states, m^* is the effective mass of a hole, k_B is the Boltzmann constant [58]. However, the recoil energy produced by pp neutrinos could only produce a few charge carriers by exciting these impurities. Such a small signal could be immersed in the noise of the generic Ge detectors. If the charge carriers can be internally amplified to surpass the level of electronic noise, then such a small signal created by pp neutrinos can be detected by a GeICA detector.

4.3 Absorption cross section

A critical question related to the above detector working principle is the phonon absorption cross section. The scattering mechanism of phonons off the neutral impurities at low-temperature regime is governed by the following reactions

$$D^X + \Delta E_D \rightarrow e^- + D^+; A^X + \Delta E_A \rightarrow h^+ + A^- \tag{20}$$

where D^X represents neutral donors, ΔE_D is the energy absorbed by neutral donors, e^- is the charge carrier produced after ionization of impurity. Here, ΔE_D is the energy of the incoming phonon. The absorption cross section is independent of the incoming particle but rather depends upon the incoming particle's energy (frequency). The net impurities present in our crystal for this work is 2×10^{10} cm^{-3} and the energy of phonons we have used ranges from 0.00325 eV to 0.026 eV. Using a direct analogy to photons having energy $\hbar\omega$ as quanta of excitation of the lattice vibration mode of angular frequency ω, the angular frequency of phonons with energy from 0.00325 eV to 0.026 eV is in the range of 4.92×10^{12} Hz to 3.94×10^{13} Hz. According to Majumdar [118], the cross section of scattering of lattice waves (phonons) off an impurity with radius R is given by

$$\sigma = \pi R^2 \chi^4/(\chi^4 + 1), \tag{21}$$

where $\chi = \omega R/v$ is called the size parameter, v is the group velocity of phonons assumed to be a constant, which is equal to the speed of sound in Ge, ω is the angular frequency of phonons. For calculating the effective radius of impurities in Ge, we have used the effective mass approximation [119] with effective Bohr's radius (R) of impurities:

$$R = 0.53\ \text{Å}\varepsilon/(m^*/m) \tag{22}$$

where ε is the dielectric constant of Ge which is equal to 16, m^* is the hydrogenic effective mass [120]. The value of m^*/m is taken to be 0.21 in the case of holes in p-type Ge. Using these values we have calculated the values of cross sections for various energies of phonons which are depicted in Table 8. From Table 8 we can infer that for the range of the phonon energies we have used in this work, the absorption cross sections are almost a constant, which is $\sim5\times10^{-13}$ cm^2. Note that the estimated cross section is mainly a geometrical cross section, which largely depends on the radius of the impurity. This is valid because the ionization cross section can be estimated using the electron impact ionization cross section of hydrogen

Phonon energy(eV)	Frequency(Hz)	Effective radius(cm)	Size parameter(χ)	$\chi^4/(\chi^4+1)$	Cross section(cm^2)
0.037	5.61×10^{13}	$4.03 \times 10{-7}$	42.01	1	5.12×10^{-13}
0.026	3.94×10^{13}	$4.03 \times 10{-7}$	29.52	0.999	5.12×10^{-13}
0.013	1.51×10^{13}	$4.03 \times 10{-7}$	11.35	0.999	5.11×10^{-13}
0.0065	9.87×10^{12}	$4.03 \times 10{-7}$	7.38	0.999	5.11×10^{-13}
0.00325	4.93×10^{12}	$4.03 \times 10{-7}$	3.69	0.994	5.09×10^{-13}

Table 8: Phonon-impurity cross sections for various energies of phonons and their corresponding angular frequencies.

atom [121] scaled by effective masses and the dielectric function.

4.4 Projected sensitivity

If we assume a Ge detector of 3 cm thickness with a total energy deposition of 2.0 eV, where each phonon has the energy of 0.026 eV, then the total number of parent phonons is ∼76. During the transport, each parent phonon undergoes anharmonic decay to generate two daughter phonons, each of which has energy equal to half of the parent phonon. We can estimate the total number of charge carriers $N_{carriers}$ using the formula below:

$$N_{carriers} = \sum_i n_i p_i f(E_A)_i \tag{23}$$

where n_i is the number of i^{th} phonons where $i = 1, 2, 3, ...$ is the order of phonons which are generated in the anharmonic decay sequence and , p_i is the absorption probability of i^{th} phonons given by Equation 18 and $f(E_A)_i$ is the ionization or excitation probability of i^{th} phonons given by Equation 19. Figure 28 shows the total number of charge carriers created by the ionization or excitation of impurities as a function of impurity level in a given Ge detector with an unprecedented energy threshold of 2.0 eV for two temperatures, 1.5 K and 4 K.

At 1.5 K temperature, the total number of charge carriers generated in a detector with net impurity 3×10^{10} cm^{-3} is about 90 as shown in Figure 28. Note that these charge carriers are created by the different generations of the daughter phonons,

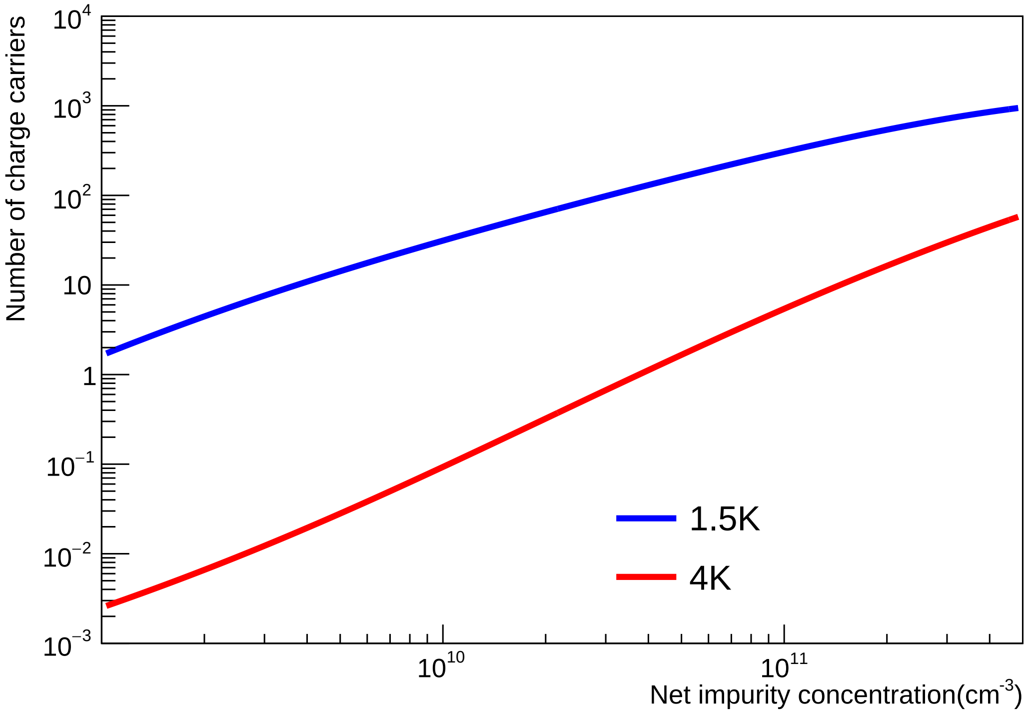

Figure 28: Number of charge carriers for different impurities in a Ge detector when the detector is operated at a very low temperatures of 1.5 K and 4 K.

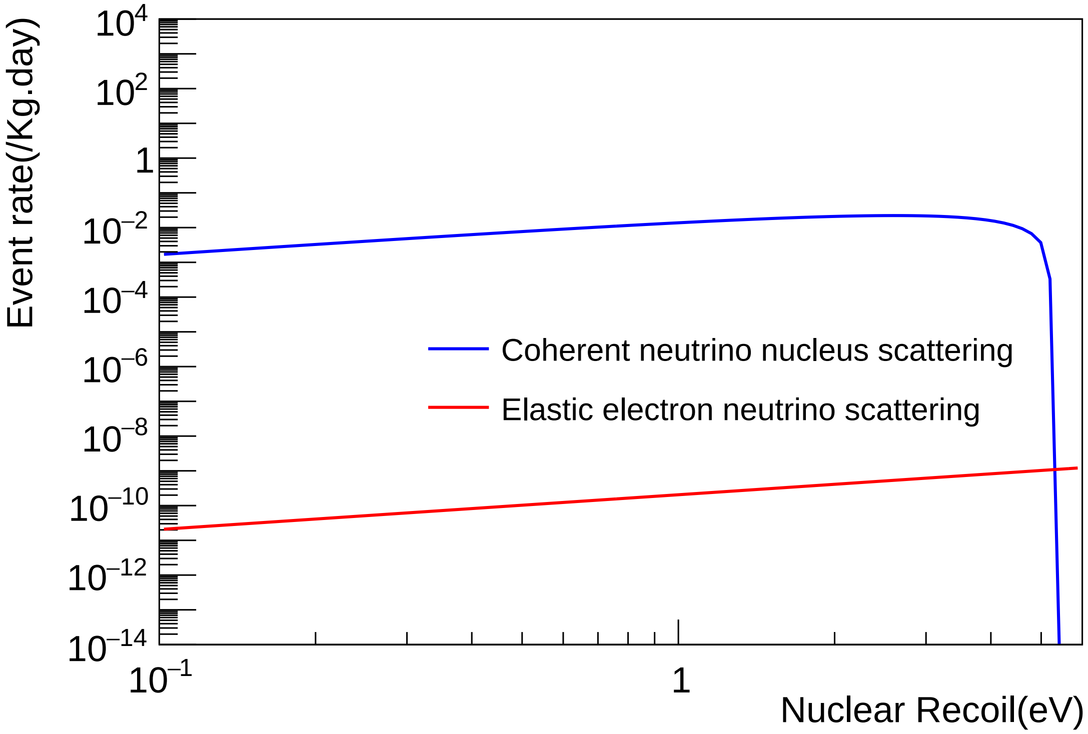

Figure 29: Event rate for pp solar neutrinos in a Ge detector of different nuclear recoil energies (eV) for elastic neutrino-electron scattering and coherent neutrino-nucleus scattering.

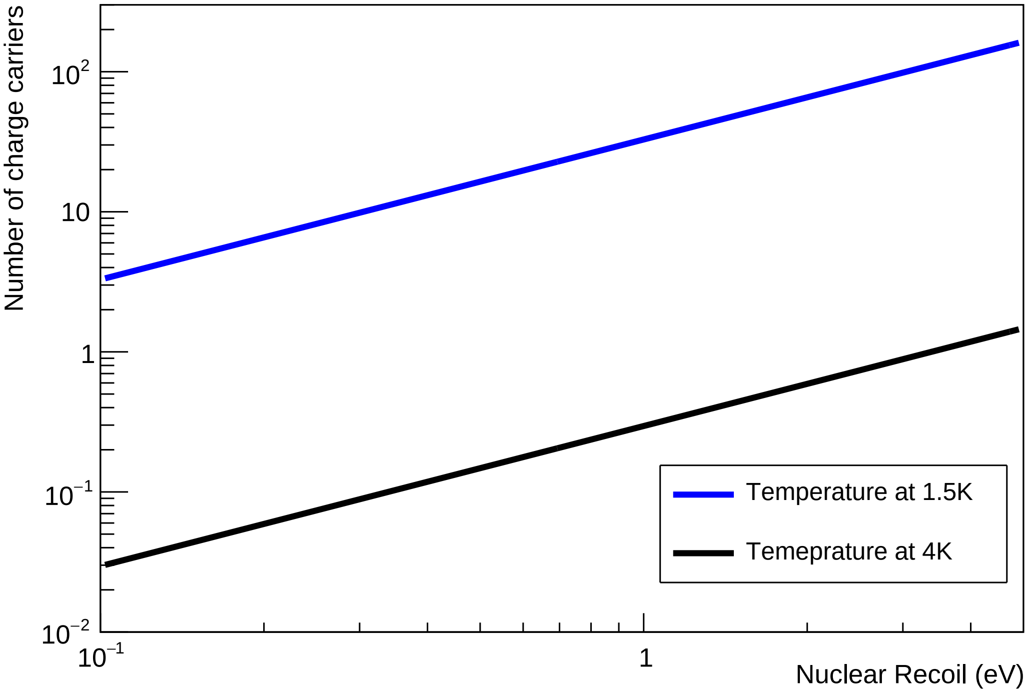

Figure 30: Number of charge carriers produced by phonons produced by pp neutrinos in a Ge detector for different nuclear recoil energies.

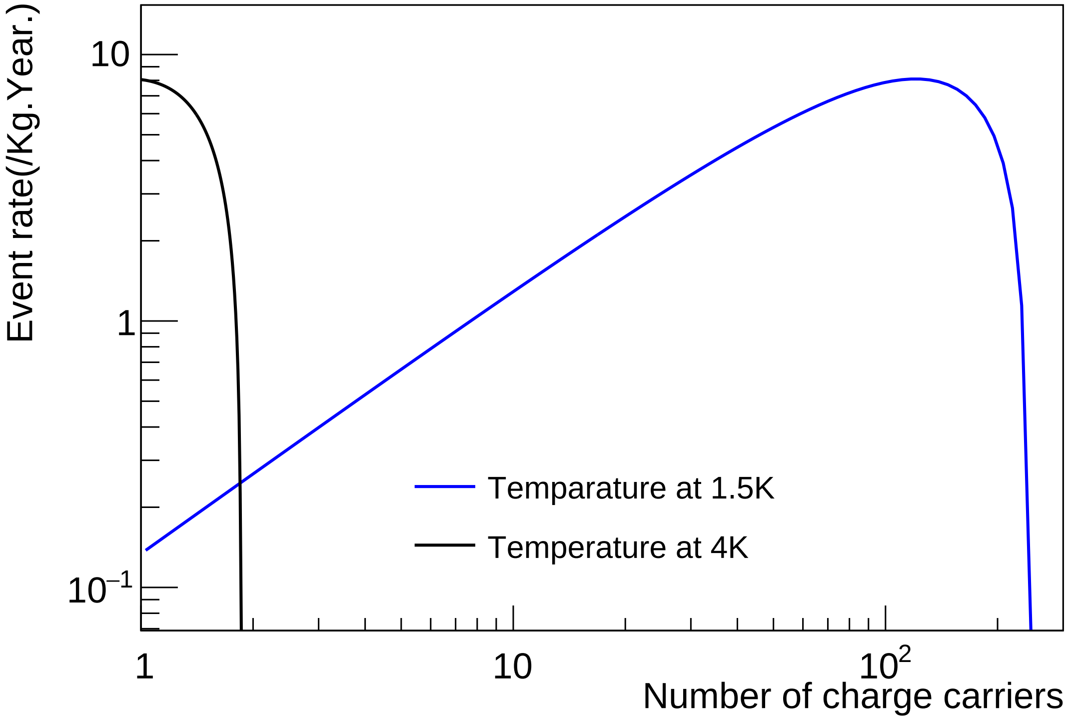

Figure 31: Event rate of pp neutrinos in a Ge detector when the detector is operated at 1.5 K and 4 K.

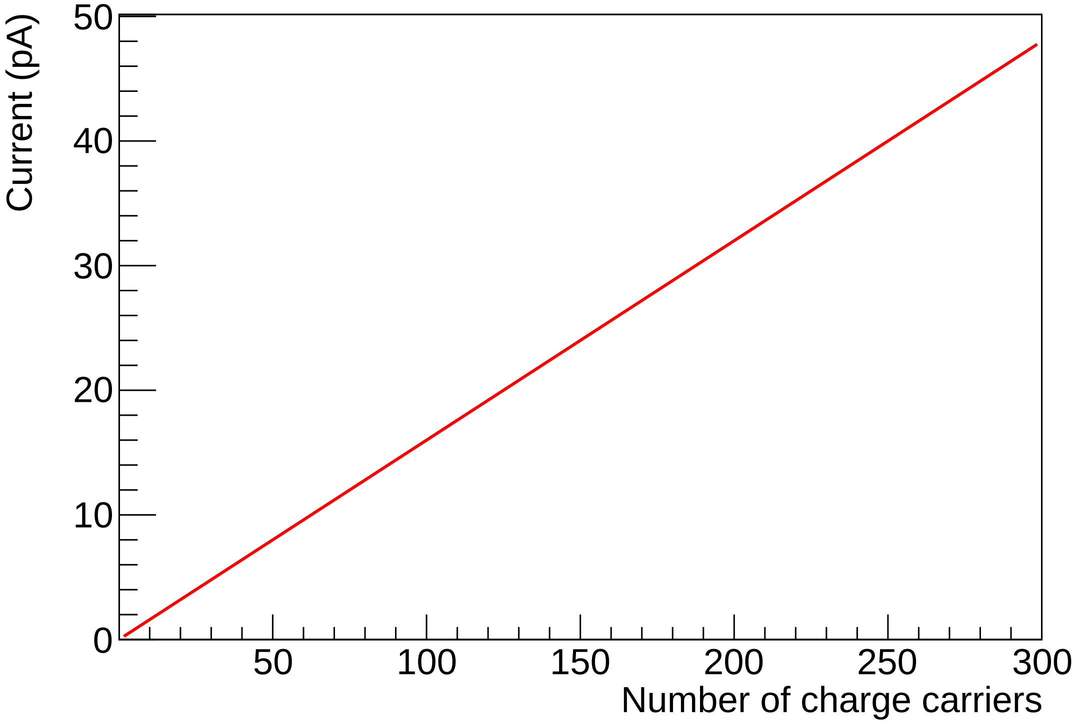

Figure 32: Current signal in the Ge detector when the pp neutrinos produce different number of charge carries through phonon channel.

from the parent phonons of 0.026 eV energy. With an impurity level of 7 × 10^{10} cm^{-3}, at least one charge carrier can be produced when the detector is operated at 4 K.

Utilizing the flux and energy of pp neutrinos [41] in equation 16 and 17, we plotted the energy threshold versus the event rate for CEvNS (the blue curve) as shown in Figure 29. Note that when neutrinos interact with electrons via exchange of neutral Z^0 bosons, the differential cross section is given by

$$\frac{d\sigma_{ES}}{dT_r} = \frac{G_f^2 m_e}{2\pi}[(g_\nu + g_a)^2 + (g_\nu - g_a)^2(1 - \frac{T_r}{E_\nu})^2 +$$

$(\mathrm{g}_a^2 - g_\nu^2)\frac{m_e T_r}{E_\nu^2}]$(24) where m_e is the electron mass, T_r is the electronic recoil, E_ν is the energy of incoming neutrinos, g_v and g_a are the vector and axial couplings respectively and are defined such that

$$g_\nu = 2sin\theta_w - \frac{1}{2}, g_a = -\frac{1}{2} \tag{25}$$

where $sin^2\theta_w$ is equal to 0.223 [108]. Using the flux and energy of pp neutrinos [41] in equation 17 and 4.4, the event rate for neutrino-electron scattering versus recoil energy is shown as the red curve in Figure 29. It is clear that the event rate induced by neutrino-electron scattering (the red curve) is much smaller than that of CEvNS (the blue curve). Therefore, CEvNS is studied in this work.

The event rate for pp neutrinos is maximized at 2.6 eV nuclear recoil produced by pp solar neutrinos for 1 kg exposure for a year. Figure 30 shows the variation in the number of charge carriers for different recoil energies produced by pp solar neutrinos. We can see that at two extremely low temperatures 1.5 K and 4 K, the number of charge carriers increases as the recoil energy increases for pp solar neutrinos in a Ge detector. For example, the event rate is maximum at 2.6 eV recoil energy where the number of charge carriers is ∼110 at 1.5 K and ∼0.5 at 4 K. The event rate variation versus the number of charge carriers is shown in Figure 31. The detector is most sensitive around 2.6 eV nuclear recoil, where the number of charge carriers is ∼110 at 1.5 K. One can expect that a 10 kg detector with an exposure of one year would obtain ∼1000 events, which is a ∼3% precision in terms of measuring the pp neutrino flux [72].

The number of charge carriers can be converted into electric current I as

$$I = n_{carriers} q/t \tag{26}$$

where $n_{carriers}$ is the number of the charge carriers , q is the unit of charge equal to 1.6×10^-19 coulombs and t is the charge collection time in the detector. If one assumes $t = 1$ microsecond, we can project the amount of current when pp solar neutrinos hit our detector as shown in Figure 32. If the detector is capable of amplifying charge carriers by a factor of 100 through internal charge amplification, the value of the current obtained from a single charge carrier is in the order of pico amperes. Hence, this current can be collected by a detector as described by D Mei et al. [58] which is the principle of this work. To create a single charge carrier, a phonon with an energy of 0.01 eV can excite or ionize the impurity atoms in a Ge detector. This means that the detector threshold can reach an unprecedented low of 0.01 eV.

It is worth mentioning that there are several sources of systematic uncertainties in the ROI for detecting pp neutrinos. The first is the systematic uncertainty due to the subtraction of background events in the ROI. For example, the prominent sources of the background are the other solar neutrinos such as ^{8}B and ^{7}Be, etc.

The values of neutrino fluxes for all solar neutrinos used in the evaluation of the systematic uncertainty are calculated by using high metallicity SSM [41, 122]. The pp and pep neutrino fluxes are determined with $\leq$ 1% accuracy. However, the uncertainty in the fluxes of other solar neutrinos varies from 6% to 30% [122]. These large uncertainties in the flux are one of the main sources of systematic uncertainty. Table 1 shows the calculated total event rates for pp neutrinos is 16.58 events/kg.year and the sum of the event rate of all other solar neutrinos is 9.201 events/kg.year, which are spread over a large energy range as stated in Table 1. In the ROI, a total of $\sim$1.2 events/kg.year from other neutrinos are expected. Although the uncertainty of the flux can be as large as 30%, the contribution to the background reduction in the ROI is much smaller than the expected signal events. Hence, the systematic uncertainty from the background deduction is small. The second source of systematic uncertainty is the detection efficiency of a single charge carrier. The proposed detector is able to detect a single charge carrier. Due to the complexity of charge trapping, the proposed detector may lose charges, which results in a limited charge collection efficiency. However, this uncertainty should be minimized under a high field in which the charge trapping is negligible. The final uncertainty is associated with the amplification factor that amplifies a single charge carrier through internal charge amplification. The amplification factor (K) is given by $K = 2^{h/l}$ where h is the length of the avalanche region and l is the free electron path of inelastic scattering. The approximate value of l and h in a planar Ge detector of 3 cm thickness at 4 K is about 0.5 μm and 5 μm respectively. This leads to an amplification factor of about 1000 [58]. However, the value of K is governed by the electric field, the concentration of impurities, and the gradient of temperature in the detector. Due to the uncertainties in these parameters, it is difficult to obtain a constant value of K. The spread of the K value is likely to impact the stability of the detection threshold and hence causes systematic uncertainty in detecting pp neutrinos. In summary, there will be some system uncertainties in detecting pp neutrinos using the proposed low-threshold detector. When designing a detector system, those systematic uncertainties should be minimized to be less than the statistical error.

4.5 Study on Backgrounds

Note that the background events can come from external and internal sources. Since the proposed detector is to have a threshold of 0.01 eV and the region of interest (ROI) for detecting pp neutrinos is between 0.1 eV to 5.2 eV, in such a low-energy window, we expected both external and internal background events to be very low. This is because: (1) the external radioactive backgrounds and the muon-induced backgrounds can be minimized when the detector is operated underground with a well-shielded experimental setup [58], and (2) the radioactivity inside the detector is often to generate background events through the Compton (inelastic) scattering process. These inelastic scattering of electrons by γ rays are usually in the energy region of keV, much larger than the ROI for eV-scale Ge experiments [123, 124]. The only notable and unavoidable background is due to the elastic scattering of external neutrons originating from (α, n) reactions. The radiological neutron rate underground is typically about 10^-6 neutrons cm$^-2$ sec$^-1$ depending on rock on shotcrete [125, 126]. The background from neutrons can be avoided effectively by using appropriate shielding [26, 57]. Acoustic and optical phonons can be produced by these radiological neutrons. Similarly, neutrons form (alpha, n) interactions of surface alpha-ray contamination on copper, teflon, and/or other materials in close proximity of your HPGe crystal. Neutrons can also be produced by ^{232}Th

and ^{238}U decay chains produced inside detector materials. During construction and operation underground, radon daughter plate-out from air onto detector materials must be managed. A more detailed discussion about the backgrounds of this type of detector is discussed by D Mei et.al. [58]. Mechanical vibrations can cause optical photons like seen in fibers for MINOS experiment [127]. Main source of the background events is the correlated background from other solar neutrinos. Other than the above sources of background events, for a low threshold detector, a common source of background is the various sources of noise associated with the cooling system, electronics, and cables. However, this can be usually resolved by using a good cooling system, better electronics, and cables. Therefore, we assume this can be put in control in this paper. Note that there are always possible unknown backgrounds in the region of interest in reality and they will have to be addressed in a real experiment. In the detector assembly, light leakage might be a significant issue. Thermal radiation, including infrared radiation, caused by imperfect cooling. The ultra-sensitive electronics you require in our instruments to run and read out our HPGe crystal need to be highly stable, nearly noise-free, and designed to remove rather than introduce those optical and thermal backgrounds. Microphonics coupling in is also a potential concern.

At 4 K, thermal energy is approximately 0.00033 eV, and this determines the bulk thermal noise. With such low thermal energy, the excitation probability is thought to be at a level of 10^4. This is utterly insignificant. The injection of a single electron from electrodes is yet another potential source of background noise. To reduce this background source, materials with greater work-function values will be used.

4.6 Conclusion

We present a viable detection method for studying pp neutrinos using coherent elastic neutrino-nucleus scattering (CEvNS) in a novel Ge detector with internal charge amplification. The very low energy deposition of pp neutrinos interacting with Ge nucleus is dissipated through the emission of phonons. The diffusion of those phonons will undergo anharmonic decay. It is the propagation of those phonons that will excite and ionize impurities in Ge, which will allow us to detect the energy deposition from pp neutrinos as low as 0.01 eV. If a Ge detector can internally amplify the charge signal by a factor of 100, then the charge carriers of $\sim$100 can be detected with current of $\sim$1 pA, which is a normal signal from a Ge detector.

5 Development of Low-Threshold Detectors for Low-Mass Dark Matter Searches Using an N-Type Germanium Detector at 5.2 K

At low temperatures near liquid helium, residual impurities in germanium freeze out from the conduction or valence band into localized states, forming electric dipoles (D^{0^*} for donors and A^{0^*} for acceptors) or neutral states (D^0 and A^0). These dipole states have the ability to trap charge carriers and form cluster dipole states (D^{+^*} and D^{-^*} for donors, and A^{+^*} and A^{-^*} for acceptors)[67]. This phenomenon has been studied in detail in a previous work by Mei et. al[67]. When an alpha particle (α) from an ^{241}Am decay is sent to a Ge detector, it deposits energy and creates electron-hole pairs within a 10 μm range from the surface of the detector [128, 129]. By applying a positive or negative bias voltage to the bottom of the detector and operating it at a cryogenic temperature of approximately 4 K, only one type of charge carrier is drifted through the detector. These drifted charge carriers undergo a dynamic process of elastic scattering, trapping, and de-trapping, allowing us to study the binding energy of the formed dipole states and cluster dipole states. In this study, an n-type Ge detector is operated in two different modes, applying different bias voltages and cooling the detector to cryogenic temperature.

5.1 Mode 1

In this mode, an n-type planar detector is first cooled to 77 K and a bias voltage is applied, gradually increasing until the detector is fully depleted. The bias is then increased by an additional 600 volts to become the operational voltage. The detector is then cooled down to 5.2 K while still under the applied operational voltage.

At 77 K, the depletion process causes all the free charge carriers to be swept away, leaving only the space charge states, D^+, behind. Upon cooling to 5.2 K, a charge trapping process occurs, resulting in the formation of dipole states as electrons drift across the detector [67]. Continued drift of electrons across the detector can result in de-trapping of charge carrier through impact ionization of the dipole states. The key charge-trapping and de-trapping processes are described below:

$$e^- + D^+ \rightarrow D^{0^*}, e^- + D^{0^*} \rightarrow 2e^- + D^+. \tag{27}$$

In this mode, the operation of the n-type planar detector begins with the formation of dipole states via charge trapping as a result of the Coulomb force between the space charge states and the drifting electrons. The second process is the release of trapped charge through impact ionization of the dipole states, known as charge de-trapping. By examining the time-dependent behavior of this de-trapping process, we are able to determine the binding energy of the dipole states.

5.2 Mode 2

In this mode of operation, the n-type planar Ge detector is cooled directly to 5.2 K without any applied bias voltage. Once cooled, the detector is then biased to the desired voltage level. At these low temperatures, impurities in the Ge crystal freeze out from the conduction or valence band to form localized states that result in the creation of dipole states. As it is an n-type detector, the majority of these dipole states are D^{0^*} [67]. When an α source is placed near the detector, the resulting α-particle-induced electron-hole pairs are created on the surface of the detector. Upon applying a positive bias voltage to the bottom of the detector, the electrons created by the α particles are drifted across the detector, leading to the following processes occurring within the detector:

$$e^- + D^{0^*} \rightarrow D^{-^*}, e^- + D^{-^*} \rightarrow 2e^- + D^{0^*}. \tag{28}$$

The first process in this mode is a trapping of charges by the Coulomb forces exerted by the dipole states on the drifted electrons, resulting in the formation of cluster dipole states. The second process is a de-trapping of charges through impact ionization of the cluster dipole states. The detector experiences a dynamic process of charge trapping, transport, and creation. The study of the time-dependent de-trapping of charges through the impact ionization of cluster dipole states helps us determine their binding energy.

When comparing the two operational modes, it can be noted that in Mode 2, the dipole states are formed at 5.2 K without any applied bias voltage. These dipole states rapidly trap charges as soon as the electrons are drifted across the detector, resulting in a shorter trapping time and lower binding energy. In contrast, in Mode 1, the dipole states are formed in the space charge region when electrons are drifted across the detector with an applied bias voltage. Therefore, it is expected that the trapping time will be longer and the binding energy of the dipole states will be higher than that of the cluster dipoles.

5.3 Physics model

As mentioned earlier, the formation of dipole states and cluster dipole states in the detector depends on the operational mode. In Mode 2, when the n-type Ge detector is cooled down to 5.2 K, the majority impurity atoms freeze out from the conduction band and form electric dipole states, D^{0^*}. If a positive bias voltage is applied to the bottom of the detector, electrons produced by the α particles from the ^{241}Am source, which is located above the detector within the cryostat, can be drifted across the detector. This drifting of electrons leads to the formation of cluster dipole states, D^{-^*}, through the charge trapping between the dipole states and the drifted electrons. As the bias voltage increases, the charge carriers gain more kinetic energy and begin to emit from the traps, resulting in a decrease in the number of cluster dipole states and an increase in electric dipole states.

In Mode 1, when a positive bias voltage is applied, electrons are drifted across the detector, leading to the formation of dipole states D^{0^*} through the space charge states of D^+. As the bias voltage increases, the drifted electrons gain more kinetic energy and are capable of freeing trapped electrons from the dipole states. In both modes, the emission rate of the charge carriers is time-dependent and reaches a balance when the charge emission and charge trapping are equal. At a sufficient bias voltage, such as around 800 volts, charge trapping becomes negligible and the charge emission also becomes negligible. The emission rate (e_n) of the charge carriers can be mathematically expressed as: [130].

$$e_n = \sigma_{trap} v_{th} N_c \exp\left(-\frac{E_B}{k_B T}\right), \tag{29}$$

where σ_{trap} represents the trapping cross-section, v_{th} is the thermal velocity, N_c $= 2.46 \times 10^{15}/\mathrm{cm}^3$ is the effective density of states of electrons in the conduction band at 5.2 K, E_B is the binding energy of the trapped charge carriers, k_B is the Boltzmann constant, and T is the temperature of the detector.

By using the experimental data to directly determine e_n and by knowing the values of v_{th}, N_c, and T, one can obtain the binding energy of dipole states or cluster dipole states from equation 29, provided the value of the trapping cross-section, σ_{trap}, is known. However, determining the value of σ_{trap} requires further calculation, as will be discussed.

The trapping cross-section (σ_{trap}) of the charge carriers is related to the trapping length (λ_{th}) through the following relation:[131, 132]

$$\lambda_{th} = \frac{1}{\left(\frac{N_A+N_D\pm|N_A-N_D|}{2}\right) \times \left(\sigma_{trap} \times \frac{v_{tot}}{v_d}\right)}, \tag{30}$$

where N_A and N_D represent the p-type and n-type impurities, respectively. v_{tot} is the total velocity of the drift electrons, and v_d is the drift velocity, which is dependent on the electric field (E) and is given by:

$$v_d \approx \frac{\mu_0 E}{1 + \mu_0 E / v_{sat}}, \tag{31}$$

where μ_0 represents the mobility of the charge carrier when the field is zero, and can be expressed as $\mu_0 = \mu_0(H)/r$. The Hall mobility, $\mu_0(H)$, has standard values of 36000 $\mathrm{cm}^2/\mathrm{Vs}$ for electrons and 42000 $\mathrm{cm}^2/\mathrm{Vs}$ for holes, while the corresponding values of r are 0.83 for electrons and 1.03 for holes. The saturation velocity, v_{sat}, can be calculated using the following empirical formula[132]:

$$v_{sat} = \frac{v_{sat}^{300}}{1 - A_v + A_v(T/300)}. \tag{32}$$

The saturation velocity at 300 K, v_{sat}^{300}, for electrons and holes are 7×10^6 cm/s and 6.3×10^6 cm/s, respectively. The values of A_v for electrons and holes are 0.55 and 0.61, respectively [133]. Additionally, the charge collection efficiency (ϵ) of a planar Ge detector can be related to the trapping length (λ_{th}) through the following formula [134, 132]:

$$\epsilon = \frac{\lambda_{th}}{L}\left(1 - \exp\left(-\frac{L}{\lambda_{th}}\right)\right), \tag{33}$$

where $L = 5.5$ mm represents the detector thickness.

The determination of the charge collection efficiency (ϵ) in a planar Ge detector enables us to calculate the charge trapping cross-section (σ_{trap}) using Equation 30. The necessary inputs, such as the net impurity concentration ($N_A + N_D \pm |N_A - N_D|$), are known from the Hall effect and capacitance-voltage measurements, while the electric field (E) in the detector can be obtained using the applied bias voltage.

With the calculated values of ϵ and the known thickness of the detector (L), we can find λ_{th} from Equation 33. The total velocity (v_{tot}) of the charge carriers is the combination of their thermal velocity (v_{th}) and the saturation velocity (v_{sat}). By combining the equations for λ_{th} and v_{tot}, we can determine the electric field-dependent trapping cross-section (σ_{trap}) [132].

In an n-type Ge detector, the emission rate (e_n) of charge carriers from the traps is measured during operation in both Mode 1 and Mode 2. The energy versus time plot is used to determine the emission rate by analyzing the slope of the plot after a given bias voltage has been applied to the detector. By combining this value with Equation 28, we can find the binding energy of dipole states and cluster dipole states in the n-type Ge detector at cryogenic temperature.

5.4 Experimental procedure

The USD crystal growth and detector development infrastructure is a state-of-the-art facility equipped with a zone refining process for purifying commercial ingots to a high level of purity suitable for crystal growth using the Czochralski method [114, 116, 81]. This results in high-quality homegrown crystals that are used for the fabrication of n-type (R09-02) detectors in the USD detector fabrication lab [135]. The R09-02 detector has a net impurity concentration of $7.02 \times 10^{10}/\text{cm}^3$ and dimensions

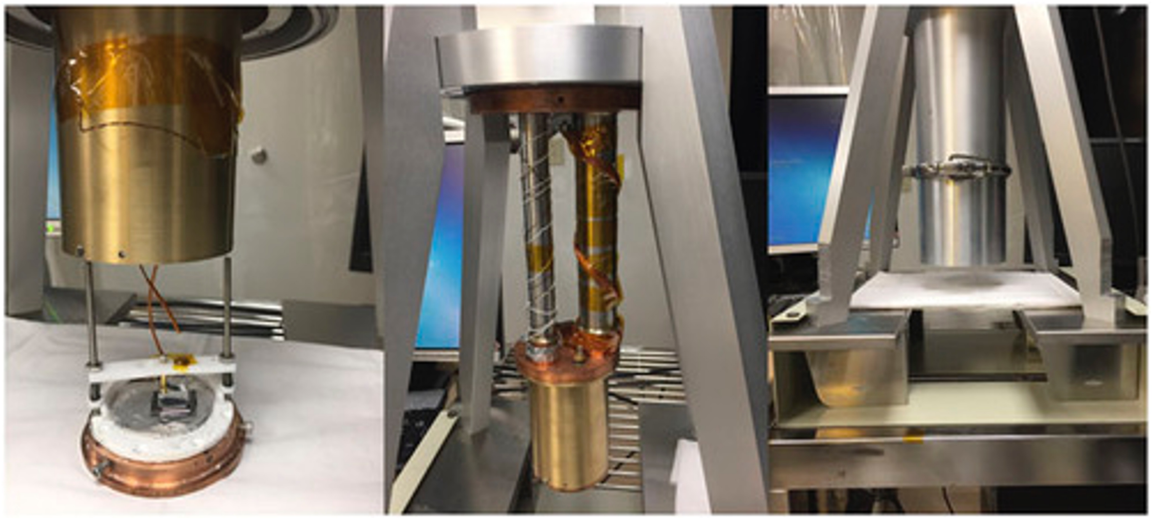

Figure 33: The detector is loaded into a pulse tube refrigerator (PTR), and two temperature sensors mounted above and below the detector are used to determine the temperature of the detector.

of 11.7 mm × 11.5 mm × 5.5 mm.

To ensure optimal electrical performance, an amorphous Ge passivation layer of 600 nm was coated on the surface of the Ge crystal as the electrical contact, effectively blocking surface charges[71, 136]. An alpha source (^{241}Am) was positioned near the detector inside a cryostat, and the energy deposition of α particles was measured. This creates localized electron-hole pairs near the top surface of the detector, and the electrons are drifted through the detector by applying a positive bias voltage to the bottom of the detector. The experimental setup for this measurement is illustrated in Figure 33.

This experiment was conducted using two modes of operation. In Mode 1, the R09-02 detector was depleted at 77 K with a depletion voltage of 1200 V and an operational voltage of 1800 V. An alpha source (^{241}Am) emitting alpha particles with an energy of 5.3 MeV was positioned above the detector within the cryostat. The energy spectrum was measured for the energy deposition of the 5.3 MeV alpha particles, which was visible as a 3.7 MeV energy peak due to energy loss on the way to the detector's active region. This 3.7 MeV energy deposition served as a reference for the energy deposition of 5.3 MeV alpha particles in the n-type detector without charge trapping, as the detector charge trapping at 77 K with a bias of 1800 volts was negligible. The charge collection efficiency was determined by dividing the measured alpha energy peak by 3.7 MeV for a given bias voltage.

In this mode, the detector was fully depleted at a constant bias voltage of 1800 V as the temperature was decreased to 5.2 K. This allowed for the formation of electric dipole states due to space charge at 5.2 K. The data was collected with a bias voltage applied in descending order from 1800 V to 30 V at 5.2 K, with histograms of energy deposition by alpha particles recorded every 2-3 minutes for 60 minutes at each bias voltage.

In Mode 2, the detector was cooled directly to 5.2 K without any bias voltage applied. Once the temperature reached 5.2 K, a positive bias voltage was gradually applied from the bottom of the detector, causing the electrons created on the surface to be drifted across the detector under the electric field. Energy spectrum measurements were taken at different bias voltages of 30 V, 100 V, 200 V, 300 V, 450 V, 600 V, 1200 V, and 1800 V. Similar to Mode 1, data was taken for 60 minutes at each bias voltage with histograms of energy deposition by alpha particles recorded every 2-3 minutes.

5.5 Result and discussion

Figures 34 and 35 demonstrate the energy deposition from 5.3 MeV alpha particles in the n-type detector when it operates under Mode 1 and Mode 2, respectively. The charge collection efficiency of the detector is determined by comparing the

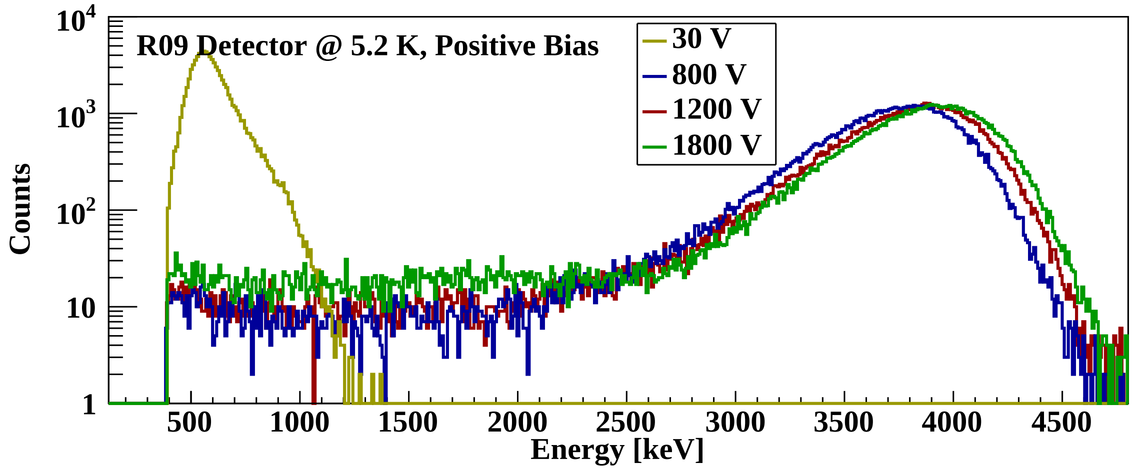

Figure 34: The energy deposition of 5.3 MeV α particles in an n-type detector operating in Mode 1.

mean total energy deposited at 5.2 K with a specific bias voltage to the mean energy deposited at 77 K when the detector was depleted and operated with a bias voltage of 1800 volts. For instance, the mean energy observed at 77 K with a bias voltage of 1800 V was 3.7 MeV, while the mean energy observed at 30 V at 5.2 K was 0.725 MeV. This results in a charge collection efficiency of 19.6% ($\epsilon = 0.725$ MeV/3.7 MeV) in Mode 2. Figure 36 shows the charge collection efficiency as a function of the applied bias voltage when the detector is operated in Mode 1 & 2. The trapping length (λ_{trap}) of the charge carriers was then calculated using Equation33 based on the charge collection efficiencies obtained at various bias voltages and the thickness (L) of the detector (5.5 mm). The calculated values are presented in Figure 37.

The net impurity concentration of the detector was measured to be $7.02\times10^{10}/\text{cm}^3$ and it was operated at a temperature of 5.2 K using the two modes described earlier. These values, along with other parameters presented in Equations 31, 32, and 33, were utilized to calculate the trapping cross-section of the trap centers. The relationship between the trapping cross-section and the applied bias voltage is illus-

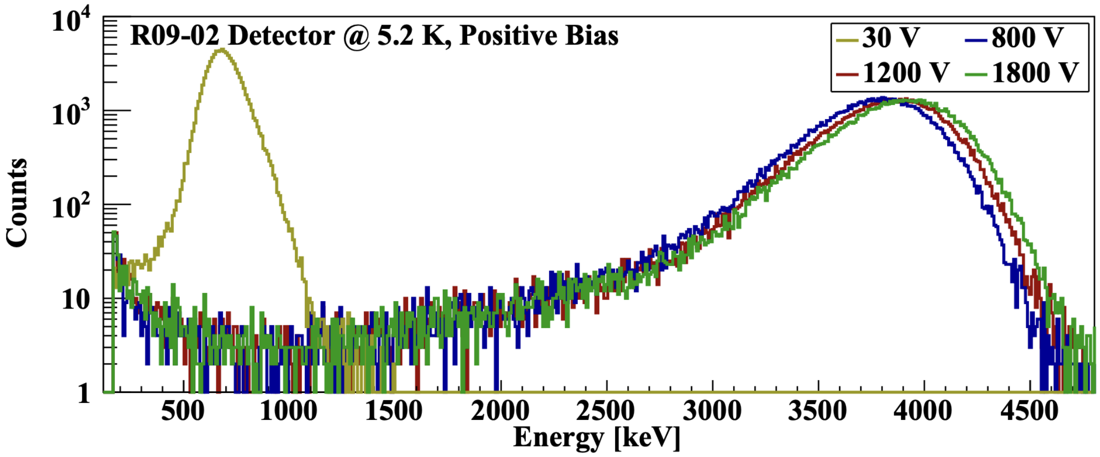

Figure 35: The energy deposition of 5.3 MeV α particles in an n-type detector operating in Mode 2.

trated in Figure38.

To determine the charge emission rate described in Equation 29, we conducted a measurement of the energy deposition from α particles as a function of time for a given bias voltage at 5.2 K over a 60-minute interval. We recorded the histogram of the energy deposition every 2-3 minutes within this time frame. The mean value of the energy deposition was determined from the observed α peak. An example of this measurement is shown in Figure 30, where the energy deposition versus time is plotted for a bias voltage of 200 volts.

As demonstrated in Figure 40, when the bias voltage is applied to the detector, the charge emission rate increases linearly for the first few minutes. This is due to the fact that the de-trapping through impact ionization of the dipole states or cluster dipole states outpaces the trapping of the charge carriers in the initial minutes at a given voltage. However, once the trapping and de-trapping reach a dynamic equilibrium, the energy deposition becomes constant. The slope of the portion of the plot where the emission of charge carriers is dominant provides the charge-energy emission rate per unit of time, represented as e_n in Equation 29. By divid-

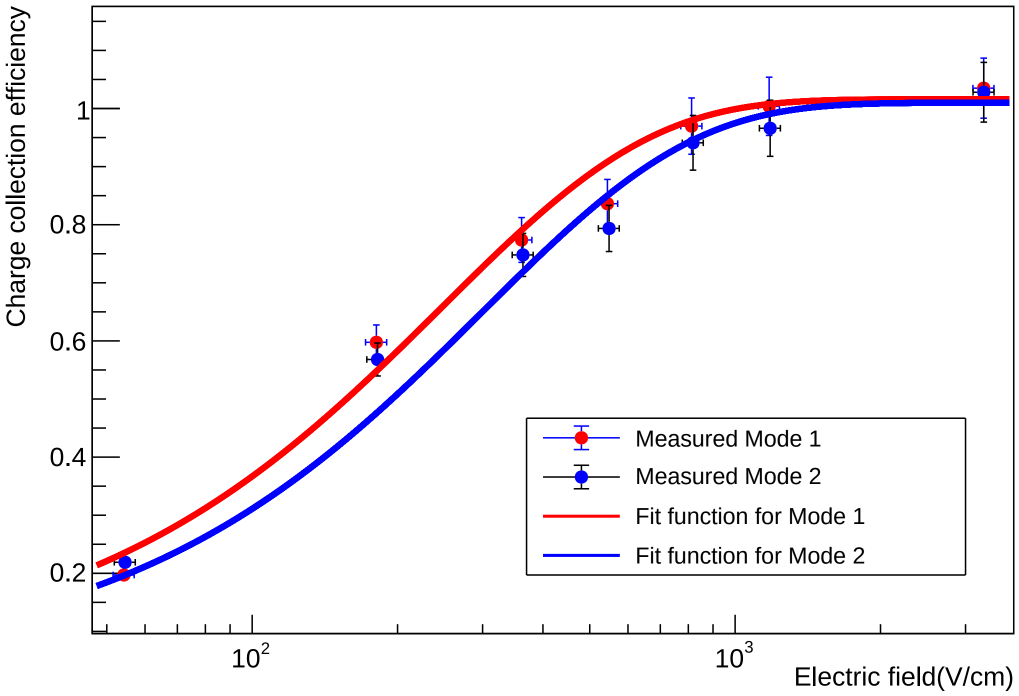

Figure 36: The graph of charge collection efficiency (ϵ) versus applied electric field (E) for Detector R-09 at Mode 1 and Mode 2 has been plotted, with errors taken into account. The error in ϵ is based on the measurement of the mean energy deposition, while the error in E is largely influenced by the bias voltage applied. A fitting model, $\epsilon = p_0 + [(p_1 \times \exp(-(p_2) \times E)]$, was utilized to curve-fit the data, resulting in the following fitted parameters: $p_0 = 1.01 \pm 0.008$, $p_1 = -0.973 \pm 0.001$, and $p_2 = (0.0033 \pm 0.0003) \frac{cm}{V}$ for Mode 1 and $p_0 = 1.008 \pm 0.008$, $p_1 = -0.974 \pm 0.001$, and $p_2 = (0.0027 \pm 0.0003) \frac{cm}{V}$ for Mode 2 respectively. The systematic uncertainty in the measurement of the charge collection efficiency is about 1% with 1σ confidence level limit. The fitted results are $\chi^2/\text{ndf} = 5.97/4$ for Mode 1 and 6.30/4 for Mode 2.

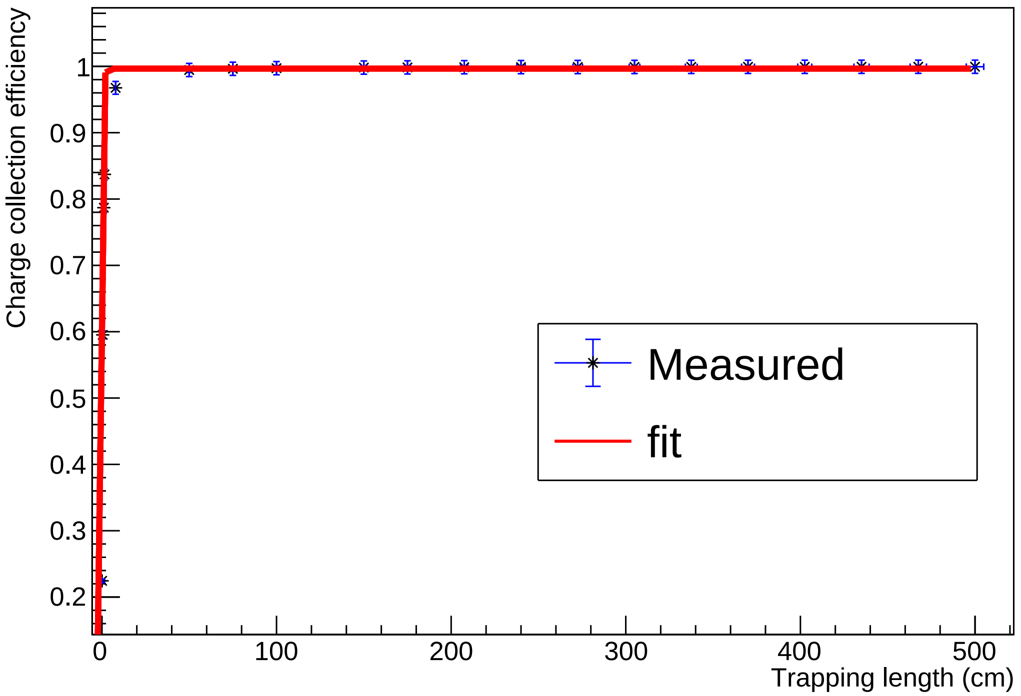

Figure 37: The graph of charge collection efficiency (ϵ) versus trapping length (λ_{trap}) for an n-type Detector R-09 has been plotted, taking into account the errors. The error in ϵ is derived from the measured mean energy deposition, while the error in λ is calculated using the propagation of error in Equation 33. A fitting model, $\epsilon = \frac{p_0}{1+(p_1 \times \exp(-p_2 \times \lambda_{trap}))}$, was applied to fit the data, resulting in the following fitted parameters: $p_0 = 0.996 \pm 0.015$, $p_1 = 4.83 \pm 0.46$, and $p_2 = (3.3 \pm 0.39)/\text{cm}$. The systematic uncertainty in the measurement of the charge collection efficiency is about 1% with 1σ confidence level. The fitted result quality is $\chi^2/\text{ndf} = 73.14/17$.

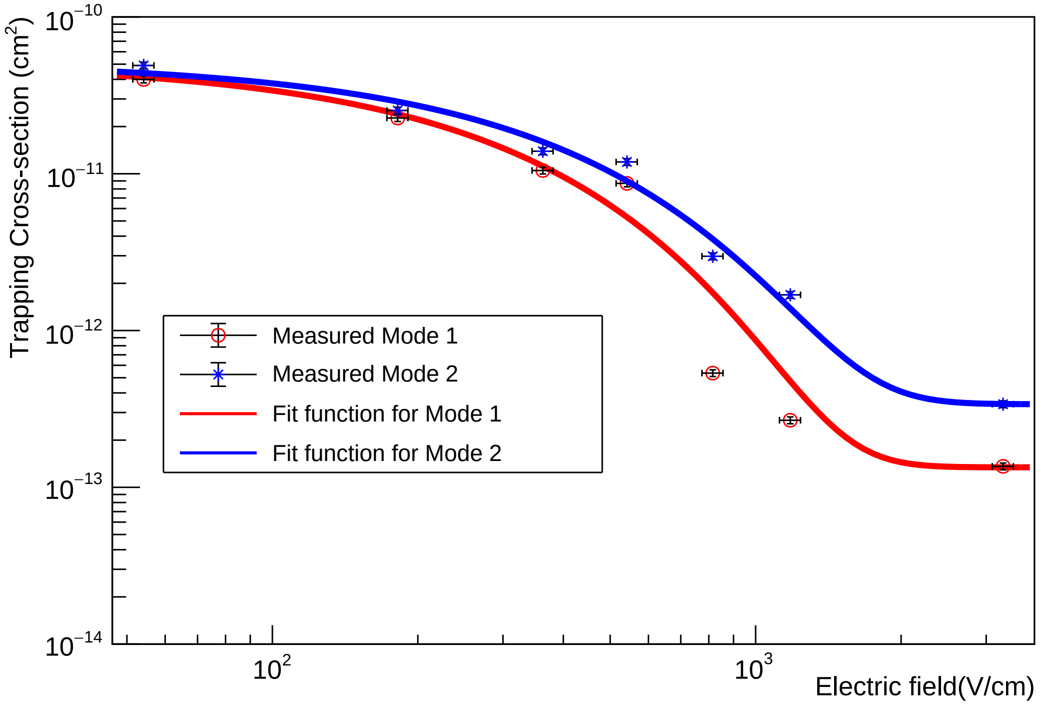

Figure 38: The graph of the variation of trapping cross-Section (σ_{trap}) with the applied bias field (E) in detector R-O9 has been plotted for both Mode 1 and Mode 2, considering the errors. The error in σ_{trap} is calculated using the propagation of error in Equation 30 while the error associated with E is primarily due to the applied bias voltage. A fitting model, $\sigma_{trap} = p_0 - [(p_1) \times \exp(-p_2 \times E)]$, was used to fit the data, with the following fitted parameters for Mode 1: $p_0 = (1.34 \times 10^{-13} \pm 1.83 \times 10^{-14})$ cm^2, $p_1 = -(5.17 \times 10^{-11} \pm 7.4 \times 10^{-12})$ cm^2, and $p_2 = (0.00425 \pm 0.00014) \frac{cm}{V}$. For Mode 2, these values are: $p_0 = (3.38 \times 10^{-13} \pm 1.69 \times 10^{-14})$ cm^2, $p_1 = -(5.20 \times 10^{-11} \pm 5.21 \times 10^{-12})$ cm^2, and $p_2 = (0.000335 \pm 0.00012) \frac{cm}{V}$. The fitted result quality are $\chi^2/\text{ndf} = 27.14/4$ for Mode 1 and 15.3/4 for Mode 2 . The trapping cross-section of the states for Mode 1 when 450 V and 650 V are applied are out of fit for the model. This is due to the uncertainty in data taking and the experimental set up. It is extremely difficult to maintain the homogeneity of the detector states in the measurement, in these low temperature conditions especially when you perform the experiment and take data for long period of time. The systematic uncertainty on the measurement of trapping cross-section is $\sim 5\%$ with 1σ uncertainty level.

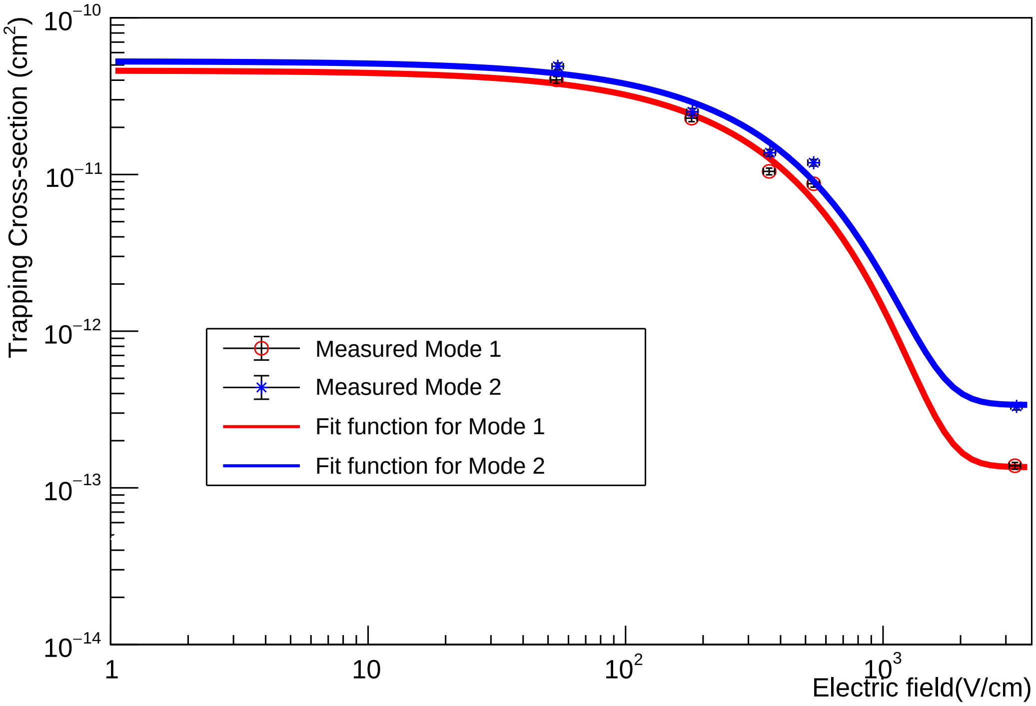

Figure 39: The graph of the variation of trapping cross-Section (σ_{trap}) with the applied bias field (E) in detector R-O9 excluding outliers points in Figure 38 (for 450 V and 650 V biases) has been plotted for both Mode 1 and Mode 2, considering the uncertainties. The systematic uncertainty on the measurement of trapping cross-section is ~5% with 1σ uncertainty limit. A fitting model, $\sigma_{trap} = p_0 - [(p_1) \times \exp(-p_2 \times E)]$, was used to fit the data, with the following fitted parameters for Mode 1: $p_0 = (1.356 \times 10^{-13} \pm 1.83 \times 10^{-14})$ cm^2, $p_1 = -(4.99 \times 10^{-11} \pm 7.54 \times 10^{-12})$ cm^2, and $p_2 = (0.00396 \pm 0.00014)\frac{cm}{V}$. For Mode 2, these values are: $p_0 = (3.37 \times 10^{-13} \pm 1.68 \times 10^{-14})$ cm^2, $p_1 = -(5.25 \times 10^{-11} \pm 5.23 \times 10^{-12})$ cm^2, and $p_2 = (0.000333 \pm 0.00013)\frac{cm}{V}$. The fitted result quality are $\chi^2/\mathrm{ndf} = 8.62/2$ for Mode 1 and for 5.22/2 Mode 2. Fit parameters for Figure 38 and Figure 39 differ by ~0.7% which do not significantly effect the result and conclusion we infer from the experiment.

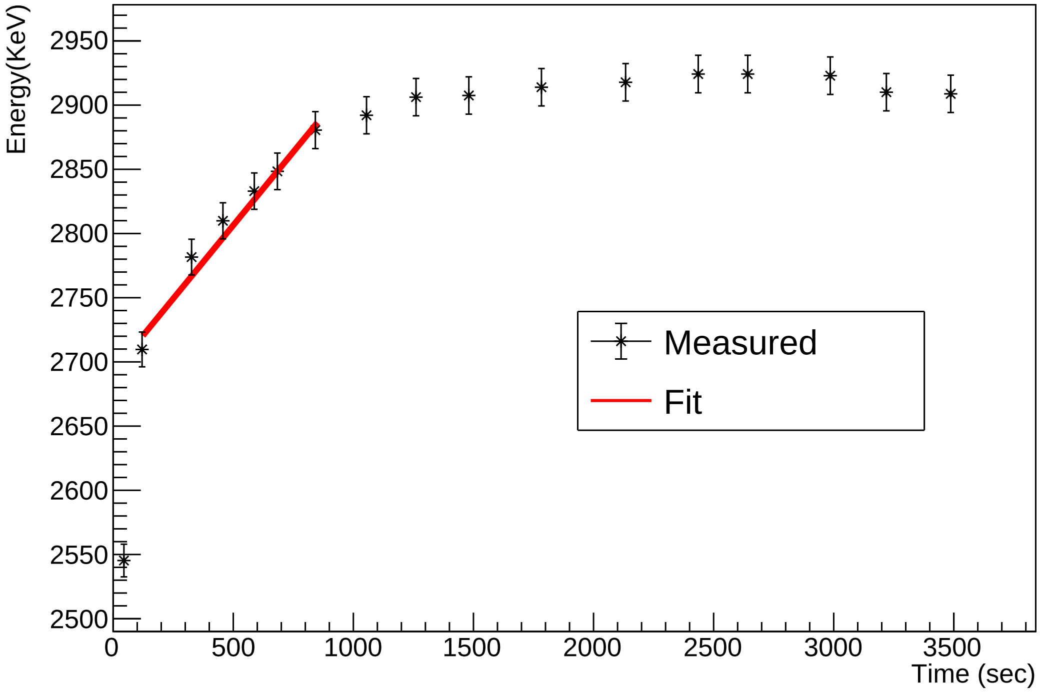

Figure 40: The mean energy deposition (E_{dep}) versus time (t) for detector R-O9 in Mode 1. As an example, the mean energy deposition (E_{dep}) and time (t) recorded for a bias voltage of 200 volts have been plotted for detector R-O9 when it is operated in Mode 1. The error in E_{dep} originates from the determination of energy deposition, while the error in t is primarily due to the determination of recorded time. A linear fit ($E_{dep} = p_0 \times t + p_1$) was applied to the portion of the plot where the emission of charge carriers is higher than the trapping of charge carriers. The slope (p_0) of the fit was calculated to be 0.2352 ± 0.011 and the intercept (p_1) was 2692.14 ± 13.46. The fitted result quality are $\chi^2/\text{ndf} = 2.80/4$. It is important to note that the slope represents the emission rate of charge (e_n) in Equation 29. The systematic uncertainty on the measurement of energy deposition is $\sim 0.5\%$ with 1σ uncertainty level.

		Mode 1			Mode 2		
Bias voltage (V)	Electric field(V/cm)	Slope (eV/s)	Binding Energy(meV)	Trapping cross-section(cm^2)	Slope(eV/s)	Binding Energy(meV)	Trapping cross section(cm^2)
30	54.54 ± 2.72	53.12 ± 2.65	8.05 ± 0.40	$(3.99 \pm 0.19) \times 10^{-11}$	62.2 ± 3.11	8.15 ± 0.40	$(4.90 \pm 0.24) \times 10^{-11}$
100	181.81 ± 4.90	654.17 ± 32.8	7.09 ± 0.35	$(2.26 \pm 0.11) \times 10^{-11}$	72.7 ± 3.61	6.58 ± 0.32	$(2.51 \pm 0.13) \times 10^{-11}$
200	363.63 ± 9.09	235.2 ± 11.76	6.71 ± 0.33	$(1.03 \pm 0.05) \times 10^{-11}$	92.3 ± 4.61	6.33 ± 0.31	$(1.37 \pm 0.06) \times 10^{-11}$
300	545.45 ± 27.27	275.9 ± 13.79	6.54 ± 0.33	$(8.59 \pm 0.42) \times 10^{-12}$	87.4 ± 4.37	6.20 ± 0.31	$(1.17 \pm 0.06) \times 10^{-11}$
450	818.18 ± 40.90	59.5 ± 2.97	5.93 ± 0.29	$(5.27 \pm 0.26) \times 10^{-13}$	68.2 ± 3.41	5.47 ± 0.27	$(2.93 \pm 0.14) \times 10^{-12}$
650	1181.81 ± 59.05	29.5 ± 1.47	5.94 ± 0.28	$(2.67 \pm 0.13) \times 10^{-13}$	35.3 ± 1.76	5.19 ± 0.30	$(1.67 \pm 0.08) \times 10^{-12}$
1800	3272.72 ± 163.60	13.6 ± 0.68	5.99 ± 0.30	$(1.35 \pm 0.06) \times 10^{-13}$	19.4±0.97	4.52 ± 0.22	$(3.39 \pm 0.17) \times 10^{-13}$

Table 9: The binding energy and trapping cross-section of R-09 at 5.2 K for Mode 1 and Mode 2. The errors associated with each value are either the result of measurement errors or the error calculated from the equations used in the paper.

ing e_n by the binding energy of the dipole states or cluster dipole states (E_b), the emission rate of electrons can be obtained. These emission rates are then utilized in Equation 29 to numerically determine the binding energy for the respective dipole states or cluster dipole states. The calculated binding energies are presented in Table 9.

The binding energy measured by the detector in Mode 1 pertains to the dipole states, whereas Mode 2 provides data on the binding energy of the cluster dipole states. Additionally, the binding energy values obtained at varying bias voltages demonstrate a relationship with the electric field. As shown in Figure 41, the binding energies are plotted as a function of the electric field at a temperature of 5.2 K.

In Mode 1, the binding energies of the dipole states (D^{0^*}) vary from 5.99 meV to 8.05 meV depending on the electric field. When the electric field is zero, the average binding energy is calculated to be 8.369 ± 0.748 meV, which is the sum of p_0 + p_1. Similarly, the binding energies of the cluster dipole states (D^{-^*}) in Mode 2 range from 4.52 meV to 8.15 meV based on the applied electric field. At zero field, the average binding energy is 7.884 ± 0.644 meV. The results indicate that the binding energy at zero field for D^{0^*} states is greater than that of D^{-^*} states. Moreover, Figure31 reveals that D^{-^*} states are more sensitive to the electric field than D^{0^*} states. It should be noted that the binding energies at zero field for both D^{0^*} states and D^{-^*} states are lower than the binding energies of ground state impurity

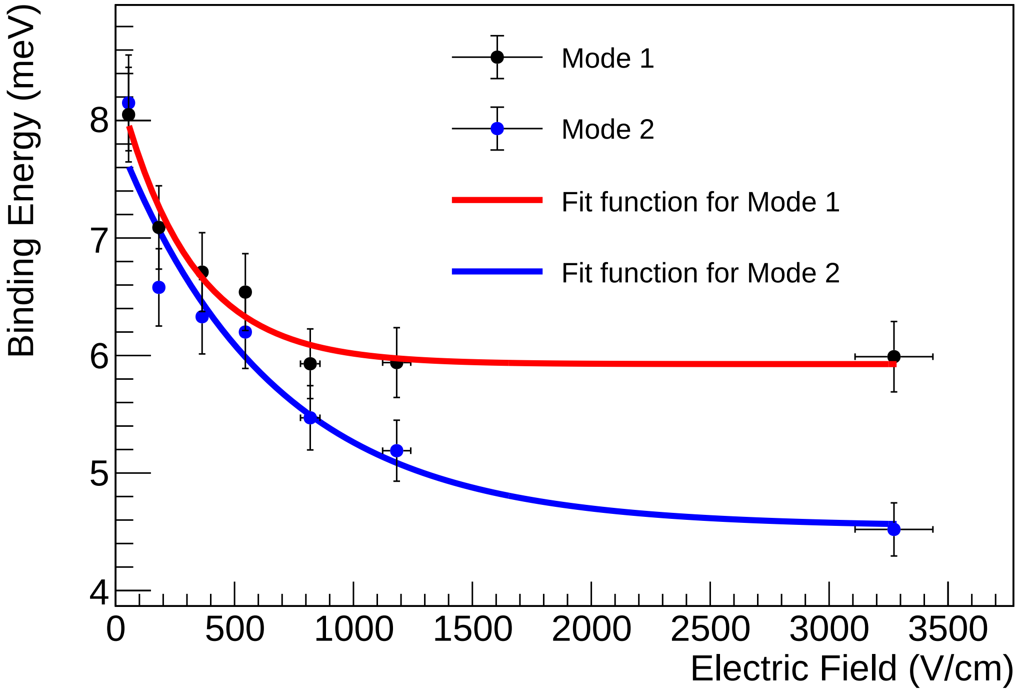

Figure 41: The binding energies of the dipole states and the cluster dipole states have been determined as a function of the applied electric field under two different operational modes, Mode 1 and Mode 2. The error in the binding energy measurement was calculated, while the error in the electric field measurement was dominated by the precision of the applied bias voltage. To analyze the data, a fit model was used, specifically $E_B = p_0 + [(p_1) \times exp(-(p_2) \times E)]$, which resulted in the following fitted parameters: For Mode 1, p_0 was found to be (5.927±0.219) meV, p_1 was (2.443±0.529) meV, and p_2 was (0.0033±0.001) $\frac{cm}{V}$. For Mode 2, p_0 was (4.545±0.248) meV, p_1 was (3.339±0.396) meV, and p_2 was (0.00154±0.0004) $\frac{cm}{V}$. The fitted result quality are $\chi^2/\text{ndf} = 4.70/4$ for Mode 1 and 3.11/4 for Mode 2.

atoms in a Ge detector, which typically fall within the range of 10 meV.

5.6 Use in dark matter searches

The event rate (R) for dark matter scattering off a target nucleus in a detector can be estimated as:

$$R = N_T \times \rho_{DM} \times \sigma \times v \times F_Q, \tag{34}$$

where, N_T is the number of target nuclei in the detector ,ρ_{DM} is the local density of dark matter σ is the dark matter-nucleus cross-section, v is the velocity of the dark matter particles, and F_Q is the nuclear form factor, which takes into account the momentum transfer of the scattering.

For a dark matter particle with mass of 100 MeV/c^2, the typical velocity in the Milky Way halo is around 10^{-3} times the speed of light, or v = 3 x 10^5 m/s [58].

The number of target nuclei in a germanium detector with a mass of 1 kg can be estimated as:

$$N_T = N_A \times m_{DETECTOR}/M \tag{35}$$

where, N_t, N_A, $m_{DETECTOR}$ and M are number of target nuclei, Avogadro's number , mass of the detector and molar mass of germanium respectively. Plugging in the values, we get the number of target nuclei to be 8.29×10^{24}. The nuclear form factor F(Q) depends on the momentum transfer Q and the specific nuclear properties of germanium. For simplicity, we can assume a constant form factor of 1.

Plugging in the values for the dark matter-nucleon cross-section of 10^{-40} cm^2 for such low threshold detector, the local dark matter density of 0.3 GeV/cm^3, and the velocity of 3 x10^5 m/s, we get the event rate for 1 kg germanium detector to be to be 7.48 events/kg.day which converts to 2730 events/kg.year. This opens up the new horizon on low dark matter search if this technology can be brought in fruition.

This estimate assumes that the background noise of the detector is zero, which is not realistic. In practice, the signal from dark matter scattering must be distinguished from the background noise and other sources of signal. However, this estimate provides a rough idea of the expected event rate for a 100 MeV dark matter particle in a germanium detector with the given specifications.

5.7 Conclusion

Our study of binding energies and trapping cross-sections in an n-type Ge detector operating at a low temperature has revealed valuable insights. Our measurements indicate that the binding energy of dipole states is 8.369 ± 0.748 meV and the binding energy of cluster dipoles is 7.884 ± 0.644 meV, both of which are lower than the typical binding energy (around 10 meV) of ground state impurities in Ge. We found that at a temperature of 5.2 K, the thermal energy of 0.448 meV is much lower than these binding energies, indicating that the corresponding cluster dipole states and dipole states are thermally stable at a temperature of 5.2 K. The application of an electric field causes the smaller binding energy of cluster dipoles to result in increased de-trapping via impact ionization when compared to dipole states. The trapping cross section, which ranges from 3.99×10^{-11} cm^2 to 1.35×10^{-13} cm^2, is primarily influenced by the electric field. Our findings further demonstrate that the binding energy and trapping cross-section decrease as the electric field within the detector increases. These low binding energies suggest the potential for developing a low-threshold detector using appropriately doped impurities in Ge for low-mass dark matter searches.

6 Summary and Outlook

For rare event physics, such as dark matter and solar neutrinos investigations, high-purity germanium detectors are required. With the help of the established germanium crystal growth facility, which consists of zone-refining, crystal growth, and characterization, we have shown that we are able to grow single germanium crystals with a large diameter (up to 12 cm), a high purity level of between 10^9 and $10^{10}/\mathrm{cm}^3$, and a low dislocation density of 7,000/cm^2. We looked at every component that could affect zone refining and HP-Ge crystal development. Zone-refining processes and experimental settings that work best have been found. Germanium ingots used for crystal formation can have impurities as low as $10^{10}/\mathrm{cm}^3$thanks to zone refining. Two techniques for controlling crystal growth's diameter have been researched and put to use. To obtain the optimum external contamination management, the causes of external contamination have been looked at. Based on meticulous calculations, the internal contamination can be managed during the growing process.

These highly pure germanium crystals were then converted into high purity germanium detectors. We have sucessfully fabricated and characterized the detectors fabricated from home grown crystals. This shows that our facility is a one of a kind for research and development high purity germanium material processing and detector fabrication.

This dissertation also presents the study of the amorphous germanium (a-Ge) as passivating contacts in a HPGe detector. Our study showed that the resistivity of the a-Ge used in our lab is very high ($\approx 10^{11}\Omega$ cm) which shows its suitability for a HPGe detector fabrication. We also studied the various electical and charge transport properties of disordered material (a-Ge in our case).For three a-Ge layers that were manufactured at USD and utilized as planar Ge detector contacts, we were able to calculate the values of the Mott's parameters.The determined values of the localization length vary in the $2A^\circ$ to $5A^\circ$ range for the three detectors USD-R02, USD-R03 and USD-W03 and are measured to be $5.07^{0.83}_{+2.58}$ A°, $2.2^{0.26}_{+0.58}$ A°, and $2.13^{-0.05}_{+0.07}$ A°, respectively depending on the density of states within the bandgap that are close to the Fermi energy level. The hopping distance varies from 72.5 A° to 147.0 A°, while the hopping energy varies from 141.5 meV to 202.8 meV, mostly dependent on temperature.

We discovered that when temperature rises, the hopping energy in a-Ge grows while the hopping distance in a-Ge reduces. Our results contrast with those of pure a-Ge made without hydrogen content, but they are comparable to those of a-Si made with hydrogen. For three a-Ge layers, we have calculated the Mott's parameter values. According to this study, the amount of hydrogen can dramatically lower the density of defect states close to the Fermi level and hence enhance the resistivity of a-Ge. As a result, the results of this study's measurements of the characteristic temperature T_0 and the localization length $(1/\alpha)$ point to the high resistivity of the a-Ge produced at USD with a hydrogen content. For HPGe detectors, a-high Ge's resistivity is a crucial quality in a passivation material. The change in the density of states close to the Fermi level, which represents the variance of the hopping energy, hopping distance, and localization length in three distinct a-Ge layers come from the fabrication process and recipe of the contacts.

We also investigated the potential of neutrino-nucleus elastic scattering to serve as a low-energy solar neutrino observatory using improved germanium (Ge) detectors. A unique technique with experimental sensitivity for detecting low-energy solar neutrinos is a Ge detector that uses internal charge amplification for the charge carriers produced by the ionization of impurities. The charge carriers produced by neutrinos interacting with Ge atoms through the emission of phonons will be amplified by Ge internal charge amplification (GeICA) detectors. With the ionization of contaminants, those phonons will produce charge carriers to reach an unprecedented low energy threshold of 0(0.1eV). We demonstrated the phonon absorption, excitation, and ionization probability of impurities in a Ge detector with impurity levels of 3×10^{10} cm^{-3}, 9×10^{10} cm^{-3}, and 2×10^{11} cm^{-3}. We outlined the sensitivity of such a Ge experiment for detecting solar neutrinos in the low-energy region. We show that, if GeICA technology becomes available, then a new opportunity arises to observe *pp* and ^{7}Be solar neutrinos. Such a novel detector with only 1 kg of high-purity Ge will give $\sim$10 events per year for *pp* neutrinos and $\sim$5 events per year for ^{7}Be neutrinos with a detection energy threshold of O(0.01 eV). We concluded that, if a Ge detector can internally amplify the charge signal by a factor of 100, then the charge carriers of $\sim$100 can be detected with current of $\sim$1 pA, which is a normal signal from a Ge detector.

In order to examine novel technology for improving low-mass dark matter detection sensitivity, we looked at charge transport in an n-type germanium detector at 5.2 K. To create low-threshold detectors, it is essential to calculate the binding energies of the dipole and cluster dipole states as well as the electric field-dependent trapping cross-sections. The detector functions in two alternative ways: either cooling immediately to 5.2 K while applying various bias voltages, or depleting at 77 K first. Findings suggested that various charge states evolved under different operating modes as seen by the reduced binding energies of charge states in the second mode, at zero field, and under an electric field. Cluster dipole and dipole state binding energies were measured to be 7.884 ± 0.644 meV and 8.369 ± 0.748 meV, respectively, at zero field, showing a low-threshold potential for low-mass dark matter searches in the future.

References

[1] M Agostini et al. "Probing Majorana neutrinos with double-β decay". In: *Science* 365.6460 (2019), pp. 1445–1448.

[2] N Abgrall et al. "The processing of enriched germanium for the Majorana Demonstrator and R&D for a next generation double-beta decay experiment". In: *Nuclear Instruments and Methods in Physics Research Section A: Accelerators, Spectrometers, Detectors and Associated Equipment* 877 (2018), pp. 314–322.

[3] R Agnese et al. "First dark matter constraints from a SuperCDMS single-charge sensitive detector". In: *Physical review letters* 121.5 (2018), p. 051301.

[4] CE Aalseth et al. "Search for Neutrinoless Double-β Decay in Ge 76 with the Majorana Demonstrator". In: *Physical review letters* 120.13 (2018), p. 132502.

[5] R Agnese et al. "Nuclear-recoil energy scale in CDMS II silicon dark-matter detectors". In: *Nuclear Instruments and Methods in Physics Research Section A: Accelerators, Spectrometers, Detectors and Associated Equipment* 905 (2018), pp. 71–81.

[6] E Armengaud et al. "Searches for electron interactions induced by new physics in the EDELWEISS-III germanium bolometers". In: *Physical Review D* 98.8 (2018), p. 082004.

[7] Yoann Kermaidic and David Radford. "76Ge detector R&D strategy for LEGEND". In: *XXVIII International Conference on Neutrino Physics and Astrophysics*. June 2018, 5, p. 5. DOI: `10.5281/zenodo.1286717`.

[8] G Angloher et al. "Commissioning run of the CRESST-II dark matter search". In: *Astroparticle Physics* 31.4 (2009), pp. 270–276.

[9] LT Yang et al. "Search for Light Weakly-Interacting-Massive-Particle Dark Matter by Annual Modulation Analysis with a Point-Contact Germanium Detector at the China Jinping Underground Laboratory". In: *Physical Review Letters* 123.22 (2019), p. 221301.

[10] D.-M. Mei et al. "Direct Detection of MeV-Scale Dark Matter Utilizing Germanium Internal Amplification for the Charge Created by the Ionization of Impurities". In: *European Physics Journal C* 78 (2018), p. 187.

[11] R Agnese et al. "Search for low-mass dark matter with CDMSlite using a profile likelihood fit". In: *Physical Review D* 99.6 (2019), p. 062001.

[12] K. Kang et al. "CDEX-1 1 kg point-contact germanium detector for low mass dark matter searches". In: *Chinese Physics C* 37.12 (2013), p. 126002.

[13] Craig E Aalseth et al. "CoGeNT: A search for low-mass dark matter using p-type point contact germanium detectors". In: *Physical Review D* 88.1 (2013), p. 012002.

[14] M Agostini et al. “Production, characterization and operation of Ge enriched BE Ge detectors in GERDA”. In: *The European Physical Journal C* 75.2 (2015), p. 39.

[15] JN Bahcall, S Basu, and MH Pinsonneault. “How uncertain are solar neutrino predictions?” In: *Physics Letters B* 433.1-2 (1998), pp. 1–8.

[16] AS Brun, S Turck-Chieze, and P Morel. “Standard solar models in the light of new helioseismic constraints. I. The solar core”. In: *The Astrophysical Journal* 506.2 (1998), p. 913.

[17] Peter AR Ade et al. “Planck 2013 results. I. Overview of products and scientific results”. In: *Astronomy & Astrophysics* 571 (2014), A1.

[18] Fritz Zwicky. “The redshift of extragalactic nebulae”. In: *Helvetica Physica Acta* 6 (1933), pp. 110–127.

[19] Fritz Zwicky. “On the Masses of Nebulae and of Clusters of Nebulae”. In: *The Astrophysical Journal* 86 (1937), p. 217.

[20] Vera C Rubin, W Kent Ford Jr, and Norbert Thonnard. “Rotational properties of 21 SC galaxies with a large range of luminosities and radii, from NGC 4605/R= 4kpc/to UGC 2885/R= 122 kpc”. In: *The Astrophysical Journal* 238 (1980), pp. 471–487.

[21] Vera C Rubin et al. “Rotation velocities of 16 SA galaxies and a comparison of Sa, Sb, and SC rotation properties”. In: *The Astrophysical Journal* 289 (1985), pp. 81–98.

[22] Gary Hinshaw et al. “Nine-year Wilkinson Microwave Anisotropy Probe (WMAP) observations: cosmological parameter results”. In: *The Astrophysical Journal Supplement Series* 208.2 (2013), p. 19.

[23] Mathbar Raut et al. “Development of InSb Low-Energy Threshold Detector for Dark Matter Searches”. In: *Bulletin of the American Physical Society* 66 (2021).

[24] E Aprile et al. “Search for new physics in electronic recoil data from XENONnT”. In: *Physical Review Letters* 129.16 (2022), p. 161805.

[25] R Agnese et al. “Search for low-mass weakly interacting massive particles with SuperCDMS”. In: *Physical review letters* 112.24 (2014), p. 241302.

[26] R Agnese et al. “Projected Sensitivity of the SuperCDMS SNOLAB experiment”. In: *Physical Review D* 95.8 (2017), p. 082002.

[27] MF Albakry et al. “Investigating the sources of low-energy events in a SuperCDMS-HVeV detector”. In: *Physical Review D* 105.11 (2022), p. 112006.

[28] E Armengaud et al. “Performance of the EDELWEISS-III experiment for direct dark matter searches”. In: *Journal of Instrumentation* 12.08 (2017), P08010.

[29] E Armengaud et al. "Constraints on low-mass WIMPs from the EDELWEISS-III dark matter search". In: *Journal of Cosmology and Astroparticle Physics* 2016.05 (2016), p. 019.

[30] Q Arnaud et al. "Optimizing EDELWEISS detectors for low-mass WIMP searches". In: *Physical Review D* 97.2 (2018), p. 022003.

[31] F Petricca et al. "First results on low-mass dark matter from the CRESST-III experiment". In: *Journal of Physics: Conference Series*. Vol. 1342. 1. IOP Publishing. 2020, p. 012076.

[32] Z She et al. "Direct Detection Constraints on Dark Photons with the CDEX-10 Experiment at the China Jinping Underground Laboratory". In: *Physical review letters* 124.11 (2020), p. 111301.

[33] Ettore Majorana. "Teoria simmetrica dell'elettrone e del positrone". In: *Il Nuovo Cimento (1924-1942)* 14.4 (1937), pp. 171–184.

[34] Frank T Avignone III, Steven R Elliott, and Jonathan Engel. "Double beta decay, Majorana neutrinos, and neutrino mass". In: *Reviews of Modern Physics* 80.2 (2008), p. 481.

[35] S Abe et al. "Production of radioactive isotopes through cosmic muon spallation in KamLAND". In: *Physical Review C* 81.2 (2010), p. 025807.

[36] JB Albert et al. "Improved measurement of the 2 ν β β half-life of 136 Xe with the EXO-200 detector". In: *Physical Review C* 89.1 (2014), p. 015502.

[37] N Abgrall et al. "LEGEND-1000 preconceptual design report". In: *arXiv preprint arXiv:2107.11462* (2021).

[38] IJ Arnquist et al. "Final Result of the Majorana Demonstrator's Search for Neutrinoless Double-β Decay in Ge 76". In: *Physical Review Letters* 130.6 (2023), p. 062501.

[39] Matteo Agostini et al. "Final results of GERDA on the search for neutrinoless double-β decay". In: *Physical review letters* 125.25 (2020), p. 252502.

[40] JB Albert et al. "Sensitivity and discovery potential of the proposed nEXO experiment to neutrinoless double-β decay". In: *Physical Review C* 97.6 (2018), p. 065503.

[41] DK Papoulias et al. "Novel neutrino-floor and dark matter searches with deformed shell model calculations". In: *Advances in High Energy Physics* 2018 (2018).

[42] R Davis. "A review of the Homestake solar neutrino experiment". In: *Progress in Particle and Nuclear Physics* 32 (1994), p. 13.

[43] S Fukuda et al. "Solar ^{8}B and hep Neutrino Measurements from 1258 Days of Super-Kamiokande Data". In: *Physical Review Letters* 86.25 (2001), p. 5651.

[44] Paul F Harrison, Don H Perkins, and WG Scott. "Tri-bimaximal mixing and the neutrino oscillation data". In: *Physics Letters B* 530.1-4 (2002), pp. 167–173.

[45] C Arpesella et al. "Direct Measurement of the Be 7 Solar Neutrino Flux with 192 Days of Borexino Data". In: *Physical Review Letters* 101.9 (2008), p. 091302.

[46] S Appel et al. "Improved measurement of solar neutrinos from the carbon-nitrogen-oxygen cycle by Borexino and its implications for the standard solar model". In: *Physical Review Letters* 129.25 (2022), p. 252701.

[47] Michael Altmann et al. "Complete results for five years of GNO solar neutrino observations". In: *Physics Letters B* 616.3-4 (2005), pp. 174–190.

[48] JN Abdurashitov et al. "Results from SAGE (The Russian-American gallium solar neutrino experiment)". In: *Physics Letters B* 328.1-2 (1994), pp. 234–248.

[49] M Cribier, LENS Collaboration, et al. "The LENS experiment". In: *Nuclear Physics B-Proceedings Supplements* 87.1-3 (2000), pp. 195–197.

[50] DB Guenther et al. "Standard solar model". In: *The Astrophysical Journal* 387 (1992), pp. 372–393.

[51] M Agostini et al. "Comprehensive measurement of pp-chain solar neutrinos". In: *Nature* 562.7728 (2018), pp. 505–510.

[52] Lincoln Wolfenstein. "Neutrino oscillations in matter". In: *Physical Review D* 17.9 (1978), p. 2369.

[53] Lincoln Wolfenstein. "Neutrino oscillations and stellar collapse". In: *Physical Review D* 20.10 (1979), p. 2634.

[54] John N Bahcall, Aldo M Serenelli, and Sarbani Basu. "10,000 standard solar models: a Monte Carlo simulation". In: *The Astrophysical Journal Supplement Series* 165.1 (2006), p. 400.

[55] Ivan Esteban et al. "Updated fit to three neutrino mixing: exploring the accelerator-reactor complementarity". In: *Journal of High Energy Physics* 2017.1 (2017), p. 87.

[56] CDMS collaboration et al. "A Search for WIMPs with the first five-tower data from CDMS". In: *arXiv preprint arXiv:0802.3530* (2008).

[57] E Armengaud et al. "Background studies for the EDELWEISS dark matter experiment". In: *Astroparticle Physics* 47 (2013), pp. 1–9.

[58] D-M Mei et al. "Direct detection of MeV-scale dark matter utilizing germanium internal amplification for the charge created by the ionization of impurities". In: *The European Physical Journal C* 78.3 (2018), p. 187.

[59] Mathbar Raut, Dongming Mei, and Sanjay Bhattarai. "Novelty of HPGe detector for direct detection of geo-neutrinos". In: *Bulletin of the American Physical Society* 65 (2020).

[60] Z Ahmed et al. "Results from a low-energy analysis of the CDMS II germanium data". In: *Physical Review Letters* 106.13 (2011), p. 131302.

[61] E Armengaud et al. "Search for low-mass WIMPs with EDELWEISS-II heat-and-ionization detectors". In: *Physical Review D* 86.5 (2012), p. 051701.

[62] Wei Zhao et al. "First results on low-mass WIMPs from the CDEX-1 experiment at the China Jinping underground laboratory". In: *Physical Review D* 88.5 (2013), p. 052004.

[63] J Aalbers et al. "First Dark Matter Search Results from the LUX-ZEPLIN (LZ) Experiment". In: *arXiv preprint arXiv:2207.03764* (2022).

[64] Rouven Essig, Jeremy Mardon, and Tomer Volansky. "Direct detection of sub-GeV dark matter". In: *Physical Review D* 85.7 (2012), p. 076007.

[65] W-Z Wei and D-M Mei. "Average energy expended per eh pair for germanium-based dark matter experiments". In: *Journal of Instrumentation* 12.04 (2017), P04022.

[66] Sanjay Bhattarai, D-M Mei, and M-S Raut. "Low-Energy Solar Neutrino Detection Utilizing Advanced Germanium Detectors". In: *arXiv preprint arXiv:2104.14352* (2021).

[67] D-M Mei et al. "Evidence of cluster dipole states in germanium detectors operating at temperatures below 10 K". In: *arXiv preprint arXiv:2203.15904* (2022).

[68] D Vénos et al. "The behaviour of HPGe detectors operating at temperatures below 77 K". In: *Nuclear Instruments and Methods in Physics Research Section A: Accelerators, Spectrometers, Detectors and Associated Equipment* 454.2-3 (2000), pp. 403–408.

[69] KM Sundqvist et al. "A Measurement of Electron and Hole Drift Velocities in a Germanium¡ 100¿ CDMS Detector, at a Temperature of 31 milliKelvin". In: *AIP Conference Proceedings*. Vol. 1185. 1. American Institute of Physics. 2009, pp. 128–131.

[70] Sanjay Bhattarai et al. "Development of Low-Threshold Detectors for Low-Mass Dark Matter Searches Using an N-Type Germanium Detector at 5.2 K". In: *arXiv preprint arXiv:2302.08414* (2023).

[71] Sanjay Bhattarai, Rajendra Panth, Dongming Mei, et al. "Experimental study of electrical conduction mechanisms in P-type amorphous germanium (Ge) used as contacts for Ge detectors in search for rare-event physics". In: *Bulletin of the American Physical Society* 65 (2020).

[72] Sanjay Bhattarai, Dongming Mei, and Mathbar Raut. “Low-Energy Solar Neutrino Detection Utilizing Advanced Germanium Detectors”. In: *APS Division of Nuclear Physics Meeting Abstracts*. Vol. 2020. 2020, SF–002.

[73] MD Fagen et al. *A History of Engineering and Science in the Bell System: Physical Sciences (1925-1980)*. Vol. 4. The Laboratories, 1983.

[74] J Bohm. “The history of crystal growth”. In: *Acta Physica Hungarica* 57.3-4 (1985), pp. 161–178.

[75] CENOS. *CENOS simulation software*. `https://www.cenos-platform.com/`. [Online; accessed 12/14/2019]. 2019.

[76] WC Dash. “Improvements on the pedestal method of growing silicon and germanium crystals”. In: *Journal of Applied Physics* 31.4 (1960), pp. 736–737.

[77] J Blears. “Measurement of the ultimate pressures of oildiffusion pumps”. In: *Proceedings of the Royal Society of London. Series A. Mathematical and Physical Sciences* 188.1012 (1946), pp. 62–76.

[78] JA Burton, RC Prim, and WP Slichter. “The distribution of solute in crystals grown from the melt. Part I. Theoretical”. In: *The journal of chemical physics* 21.11 (1953), pp. 1987–1991.

[79] RN Hall. “Hp Ge: Purification, crystal growth, and annealing properties”. In: *IEEE Transactions on Nuclear Science* 31.1 (1984), pp. 320–325.

[80] Edwin Herbert Hall. “XVIII. On the “Rotational Coefficient” in nickel and cobalt”. In: *The London, Edinburgh, and Dublin Philosophical Magazine and Journal of Science* 12.74 (1881), pp. 157–172.

[81] M-S Raut et al. “Characterization of high-purity germanium (Ge) crystals for developing novel Ge detectors”. In: *Journal of Instrumentation* 15.10 (2020), T10010.

[82] Rajendra Panth. “Development and Characterization of Germanium Detectors for Searching Rare-Event Physics”. PhD thesis. University of South Dakota, 2022.

[83] WZ Wei, DM Mei, and C Zhang. “Study well-shaped germanium detectors for low-background counting”. In: *Journal of Physics: Conference Series*. Vol. 606. 1. IOP Publishing. 2015, p. 012019.

[84] X-H Meng et al. “Fabrication and characterization of high-purity germanium detectors with amorphous germanium contacts”. In: *Journal of Instrumentation* 14.02 (2019), P02019.

[85] Rajendra Panth et al. “Characterization of high-purity germanium detectors with amorphous germanium contacts in cryogenic liquids”. In: *The European Physical Journal C* 80 (2020), pp. 1–11.

[86] ORTEC AMETEK. “High purity germanium (hpge) radiation detectors: Products: Ametek Ortec”. In: *Products, AMETEK ORTEC* (). URL: `https://www.ortec-online.com/products/radiation-detectors/germanium-hpge-radiation-detectors`.

[87] Mirion. “Germanium detectors”. In: *Detectors* (). URL: `https://www.mirion.com/products/germanium-detectors`.

[88] RD Baertsch and RN Hall. “Gamma ray detectors made from high purity germanium”. In: *IEEE Transactions on Nuclear Science* 17.3 (1970), pp. 235–240.

[89] J Llacer. “Planar and coaxial high purity germanium radiation detectors”. In: *Nuclear Instruments and Methods* 98.2 (1972), pp. 259–268.

[90] RD Baertsch. “Surface Effects on P Type High Purity Germanium Detectors at 77 K”. In: *IEEE Transactions on Nuclear Science* 21.1 (1974), pp. 347–359.

[91] AJ Tavendale. “Semiconductor nuclear radiation detectors”. In: *Annual review of nuclear science* 17.1 (1967), pp. 73–96.

[92] Ethan L Hull and Richard H Pehl. “Amorphous germanium contacts on germanium detectors”. In: *Nuclear Instruments and Methods in Physics Research Section A: Accelerators, Spectrometers, Detectors and Associated Equipment* 538.1-3 (2005), pp. 651–656.

[93] JT Walton et al. “Si (Li) X-ray detectors with amorphous silicon passivation”. In: *IEEE Transactions on Nuclear Science* 31.1 (1984), pp. 331–335.

[94] W.-Z. Wei et al. “The Impact of the Charge Barrier Height on Germanium (Ge) Detectors with Amorphous-Ge Contacts for Light Dark Matter Searches”. In: *archive* arXiv:2002.04462 (2020), p. xxxx.

[95] Paul N Luke, Craig S Tindall, and Mark Amman. “Proximity charge sensing with semiconductor detectors”. In: *IEEE Transactions on Nuclear Science* 56.3 (2009), pp. 808–812.

[96] Nevill Francis Mott. “Conduction in non-crystalline materials: III. Localized states in a pseudogap and near extremities of conduction and valence bands”. In: *Philosophical Magazine* 19.160 (1969), pp. 835–852.

[97] NF Mott and EA Davis. *Electron process in non-crystalline materials. Clarendon.* 1979.

[98] X.-H. Meng et al. “Fabrication and Characterization High-Purity Germanium Detectors with Amorphous Germanium Contacts”. In: *Journal of Instrumentation* 14 (2019), P02019.

[99] SM Sze and Kwok K Ng. “Physics of semiconductor devices John Wiley and Sons Inc”. In: *New York* (1981).

[100] Heinz K Henisch and HF Mataré. "Rectifying Semi-Conductor Contacts". In: *Journal of The Electrochemical Society* 105.3 (1958), p. 66C.

[101] Mark Amman. "Optimization of Amorphous Germanium Electrical Contacts and Surface Coatings on High Purity Germanium Radiation Detectors". In: *arXiv preprint arXiv:1809.03046* (2018).

[102] AM Szpilka and P Viščor. "Dc electrical conductivity of evaporated amorphous germanium—the low-temperature behaviour". In: *Philosophical Magazine B* 45.5 (1982), pp. 485–496.

[103] Aynur Eray, Hüseyin Tolunay, and Özcan Öktü. "The evaluation of Mott parameters by using the field dependent conductivity in amorphous germanium". In: *Journal of Non-crystalline solids* 122.2 (1990), pp. 193–196.

[104] K Yasuda, A Yoshida, and T Arizumi. "The effects of annealing on mott's parameters for hopping conduction in amorphous Ge". In: *physica status solidi (a)* 41.2 (1977), K181–K184.

[105] K Shrestha. "Electrical Conduction Mechanism In The Disordered Material System p-Type Hydrogenated Amorphous Silicon". PhD thesis. University of North Texas, 2014.

[106] Q Looker. "Fabrication Process Development for HighPurity Germanium Radiation Detectors with Amorphous Semiconductor Contacts". PhD thesis. University of California, Berkeley, 2014.

[107] AS Starostin and AG Beda. "Germanium detector with an internal amplification for investigating rare processes". In: *Physics of Atomic Nuclei* 63.7 (2000), pp. 1297–1300.

[108] J Billard, LE Strigari, and E Figueroa-Feliciano. "Solar neutrino physics with low-threshold dark matter detectors". In: *Physical Review D* 91.9 (2015), p. 095023.

[109] Fred S Goulding. "Pulse-shaping in low-noise nuclear amplifiers: A physical approach to noise analysis". In: *Nuclear instruments and methods* 100.3 (1972), pp. 493–504.

[110] PN Luke et al. "Low capacitance large volume shaped-field germanium detector". In: *IEEE Trans. Nucl. Sci* 36.926 (1989), pp. 10–1109.

[111] JF Lamb et al. "Application of Lithium-Drifted Germanium Gamma-Ray Detectors to Neutron Activation Analysis. Nondestructive Analysis of a Sulfide Ore." In: *Analytical Chemistry* 38.7 (1966), pp. 813–818.

[112] Douglas S McGregor et al. "Design considerations for thin film coated semiconductor thermal neutron detectors—I: basics regarding alpha particle emitting neutron reactive films". In: *Nuclear Instruments and Methods in Physics Research Section A: Accelerators, Spectrometers, Detectors and Associated Equipment* 500.1-3 (2003), pp. 272–308.

[113] Charles Mark Lewis. “Particle Physics in the Sub-keV Energy Regime”. PhD thesis. The University of Chicago, 2023.

[114] Gang Yang et al. “Investigation of influential factors on the purification of zone-refined germanium ingot”. In: *Crystal Research and Technology* 49.4 (2014), pp. 269–275.

[115] Jan Czochralski. “Ein neues verfahren zur messung der kristallisationsgeschwindigkeit der metalle”. In: *Zeitschrift für physikalische Chemie* 92.1 (1918), pp. 219–221.

[116] Guojian Wang et al. “Development of large size high-purity germanium crystal growth”. In: *Journal of Crystal Growth* 352.1 (2012), pp. 27–30.

[117] Robert Wittmann. “Miniaturization problems in CMOS technology: Investigation of doping profiles and reliability”. In: *Ph. D. Thesis, Vienna University of Technology* (2007).

[118] ASME Majumdar. “Microscale heat conduction in dielectric thin films”. In: (1993).

[119] B Skinner. “Properties of the donor impurity band in mixed valence insulators”. In: *Physical Review Materials* 3.10 (2019), p. 104601.

[120] OD Dubon Jr. *Electronic processes in uniaxially stressed p-type germanium.* University of California, Berkeley, 1996.

[121] IC Percival. “Cross sections for collisions of electrons with hydrogen atoms and hydrogen-like ions”. In: *Nuclear Fusion* 6.3 (1966), p. 182.

[122] FL Villante and A Serenelli. “The relevance of nuclear reactions for Standard Solar Models construction”. In: *Frontiers in Astronomy and Space Sciences* 7 (2020), p. 112.

[123] J Alexander et al. “Dark sectors 2016 workshop: community report”. In: *arXiv preprint arXiv:1608.08632* (2016).

[124] PP Kane. “Inelastic scattering of X-rays and gamma rays by inner shell electrons”. In: *Physics reports* 218.2 (1992), pp. 67–139.

[125] J Reichenbacher. “Dune module of Opportunity Workshop”. In: *IFIC Indico Server (Indico)* (). URL: `https://indico.ific.uv.es/event/6722/contributions/`.

[126] D-M Mei and A Hime. “Muon-induced background study for underground laboratories”. In: *Physical Review D* 73.5 (2006), p. 053004.

[127] JJ Evans. “The MINOS experiment: results and prospects”. In: *Advances in High Energy Physics* 2013 (2013).

[128] James F Ziegler, Matthias D Ziegler, and Jochen P Biersack. "SRIM–The stopping and range of ions in matter (2010)". In: *Nuclear Instruments and Methods in Physics Research Section B: Beam Interactions with Materials and Atoms* 268.11-12 (2010), pp. 1818–1823.

[129] IJ Arnquist et al. "α-event characterization and rejection in point-contact HPGe detectors". In: *The European Physical Journal C* 82.3 (2022), pp. 1–23.

[130] EY Lee et al. "Compensation and trapping in CdZnTe radiation detectors studied by thermoelectric emission spectroscopy, thermally stimulated conductivity, and current-voltage measurements". In: *Journal of electronic materials* 28.6 (1999), pp. 766–773.

[131] Arran Thomas James Phipps. *Ionization collection in detectors of the cryogenic dark matter search.* University of California, Berkeley, 2016.

[132] DM Mei et al. "Impact of charge trapping on the energy resolution of Ge detectors for rare-event physics searches". In: *Journal of Physics G: Nuclear and Particle Physics* 47.10 (2020), p. 105106.

[133] R Quay et al. "A temperature dependent model for the saturation velocity in semiconductor materials". In: *Materials Science in Semiconductor Processing* 3.1-2 (2000), pp. 149–155.

[134] Zhong He. "Review of the Shockley–Ramo theorem and its application in semiconductor gamma-ray detectors". In: *Nuclear Instruments and Methods in Physics Research Section A: Accelerators, Spectrometers, Detectors and Associated Equipment* 463.1-2 (2001), pp. 250–267.

[135] Rajendra Panth et al. "Temperature-dependent charge barrier height of amorphous germanium contact detector". In: *Nuclear Instruments and Methods in Physics Research Section A: Accelerators, Spectrometers, Detectors and Associated Equipment* (2022), p. 166862.

[136] W-Z Wei et al. "Investigation of amorphous germanium contact properties with planar detectors made from USD-grown germanium crystals". In: *Journal of Instrumentation* 13.12 (2018), P12026.